Building foundations for molecular electronics: growth of organic molecules on alkali halides as prototypical insulating substrates

Sarah A. Burke
Department of Physics
McGill University

November 2008

A thesis submitted to McGill University in partial fulfilment of the requirements of the degree of Ph.D.

To Dr. Manfred Jericho,
for showing me that we could "see" atoms and molecules;
I've never looked back.

Abstract

The epitaxy and growth of a series of organic molecules deposited on insulating surfaces were investigated by noncontact atomic force microscopy (nc-AFM). The molecules studied, C_{60} , 3,4,9,10-perylene tetracarboxylic dianhydride (PTCDA), 3,4,9,10-perylene tetracarboxlylic diimide (PTCDI), and copper (II) phthalocyanine (CuPc), were selected to investigate the effect of different molecular geometries, charge distributions and intermolecular interactions and as interesting candidates in molecular electronic applications. As it is known that the properties of molecules are influenced by their structural arrangements, an understanding of the interactions of molecules with substrates of interest as well as the dominant processes involved in growth are of great interest. Model insulating substrates KBr and NaCl were used for growth studies, due to the necessity of insulators in electrically isolating device regions.

Dewetting processes were observed in several of these systems : C_{60} on KBr and NaCl, PTCDA on NaCl and PTCDI on NaCl. The specific influences of dewetting are discussed for each system, in particular the morphological impact of dewetting and the driving of dewetting by strained metastable monolayers. For C_{60} deposits, interesting branched structures are formed in the process of dewetting which are remarkably stable once formed, yet do not represent the equilibrium growth morphology. A determination of the large cell coincident epitaxy reveals a small, yet significant discrepancy between the observed overlayer and calculated stable adsorption sites indicating a dominance of the intermolecular interaction over the molecule–substrate interaction. For both PTCDA and PTCDI on NaCl, strained metastable monolayer epitaxies were observed giving rise to a transition in both interface structure and morphology : a dewetting transition. A comparison of the observed molecular scale structures and growth modalities is made in order to build a framework for understanding the prevalence of dewetting for molecules on ionic surfaces.

Finally, in order to better understand the connection between molecular scale structures and interesting opto-electronic properties, the application of a hybrid-

electrostatic characterization technique by nc-AFM is discussed. Using this technique, the opto-electrostatic response of three different PTCDA arrangements on a nanotemplated NaCl surface are shown to differ according to the degree of intermolecular interaction permitted by the structure.

Résumé

L'épitaxie et la croissance d'une série de molécules organiques déposées sur surfaces isolantes ont été étudiées par nc-AFM. Les molécules étudiées, C_{60} , 3,4,9,10-perylene tetracarboxylic dianhydride (PTCDA), 3,4,9,10-perylene tetracarboxylic diimide (PTCDI), et Copper (II) Phthalocyanine (CuPc), ont été choisies pour examiner l'influence des géométries moléculaires, des distribution de charge, et de différentes interactions intermoléculaires, sur l'assemblage de candidats intéressants dans des applications en électronique moléculaire. Etant donné que les agencements structurels influencent leurs propriétés moléculaires, la compréhension des interactions entre molécules et substrats donnant lieu à la formation de couches minces est intéressant de plusieurs points de vue. Des surfaces isolantes modèles, KBr et NaCl, ont été utilisées pour les études de croissance, en raison de l'importance de l'isolement électronique de certaines régions des dispositifs.

On a observé des processus de démouillage dans quelques systèmes : C_{60} sur KBr et NaCl, PTCDA sur NaCl, et PTCDI sur NaCl. Les influences de ces processus sont discutées pour chaque système, avec une emphase particulière sur l'impact morphologique du démouillage et la force d'entraînement par des monocouches déformées. Dans le cas de C_{60} , des îlots ramifiés se forment pendant le démouillage. Ces structures sont remarquablement stables une fois formées, mais ne représentent pas la structure en équilibre. La détermination d'une épitaxie coïncidente indique une petite, mais importante, différence entre la sur-couche observée et les sites d'adsorption stables calculés. Cela indique une interaction intermoléculaire plus forte que l'interaction molécule–substrat. Pour PTCDA et PTCDI sur NaCl, les mono-couches déformées ont été observées avec pour résultat une transition de l'agencement sur l'interface et de la morphologie : un transition démouillage. Une comparaison des structures moléculaires observées et des modes de croissance est faite afin d'établir une base de compréhension pour la prédominance du démouillage dans les systèmes moléculaires sur substrats ioniques.

Finalement, pour mieux comprendre la connexion entre les structures moléculaires et les propriétés opto-électroniques intéressantes, l'application d'une technique hybride opto-électrostatique nc-AFM est discutées. Utilisant cette technique, les différentes réponses pour trois agencements de PTCDA sur une surface NaCl nano-structurée sont montrées en accordance avec le degré d'interaction intermoléculaire permis par l'agencement.

Statement of Originality

The author claims the following aspects of the thesis constitute original scholarship and an advancement of knowledge. Those topics which have formed publications are annotated with the citation information of the articles.

The thesis is primarily concerned with the characterization of several previously unexplored molecular systems on insulators by nc-AFM and the observation thereof that dewetting is a key growth process leading to bimodal growth and unique morphologies. Comparison of observations of all the systems studied provides a broader context in which to understand the origins and prevalence of dewetting in molecular deposits on insulating surfaces.

Specific contributions of original scholarship include:

- ▷ While the technique of dissipation imaging in noncontact AFM has the potential to reveal useful information about materials properties, there remain significant challenges in interpreting such data due to the seemingly strong influence of the tip structure. In response to a recent article reporting temperature dependent dissipation results which were used to determine the dissipation mechanisms on PTCDA and KBr, we wrote a comment showing our own data at room temperature and 100° K indicating that a variety of results, including changes in contrast while imaging, could be obtained depending on the tip structure and urged caution in the interpretation of limited data sets and encouraged the verification of such trends with the demonstration of reproducible results. (S.A. Burke and P. Grütter. Comment on: Temperature dependence of the energy dissipation in dynamic force microscopy, *Nanotechnology*, **19** 398001, 2008.)

- ▷ The detailed characterization of epitaxy and growth of C_{60} on KBr and NaCl surfaces and the proposal that a dewetting process contributes to the unique

morphology observed. (S.A. Burke, J.M. Mativetsky, S. Fostner, P. Grütter. C_{60} on alkali halides: Epitaxy and morphology studied by noncontact AFM. *Phys. Rev. B* **76**:035419, 2007.)

- ▷ The characterization of epitaxy and growth of PTCDA on KBr and NaCl. In particular, the determination that the formation of a strained monolayer drives the dewetting transition observed at a critical coverage for PTCDA on NaCl. (S.A. Burke, W. Ji, J.M. Mativetsky, J.M. Topple, S. Fostner, H.-J. Gao, H. Guo and P. Grütter. Strain Induced Dewetting of a Molecular System: Bimodal Growth of PTCDA on NaCl. *Phys. Rev. Lett.* **100**:186104, 2008.)

- ▷ The demonstration of a novel hybrid optical-electrostatic AFM characterization technique for locally probing electronic properties of nanoscale molecular structures on insulating substrates, providing a connection between local molecular scale arrangements and resulting opto-electronic properties. The test system PTCDA on nanotemplated NaCl was used and characterized for this study. (S.A. Burke, J.M. LeDue, J.M. Topple, S. Fostner, P. Grütter. Relating the functional properties of an organic semiconductor to molecular structure by nc-AFM. Submitted to *Advanced Materials*.)

- ▷ The characterization of a related perylene derivative, PTCDI, on KBr and NaCl for comparison to the observations concerning PTCDA. The observation of dewetting for PTCDI deposits on NaCl further indicates the prevalence of dewetting in molecule-on-insulator surfaces. (A manuscript containing the data presented here in the context of the connection between epitaxy and dewetting as well as further data characterizing the temporal evolution of the deposits, not included in the thesis, is in preparation by J. Topple.)

Contributions of co-authors

I would like to gratefully acknowledge my co-authors, who freely provided their ideas and worked to help make each article as complete and valuable a contribution as possible. For each of the articles included in this thesis, I am the principle author and as such collected all or the majority of the data presented, performed the analyses and composed the manuscripts. My supervisor, Peter Grütter was an invaluable source of ideas, knowledge and direction and played an instrumental role in the research described.

S.A. Burke and P. Grütter. Comment on: Temperature dependence of the energy dissipation in dynamic force microscopy. *Nanotechnology*, **19** 398001, 2008. *Appears in Chapter 2*

The concepts and writing were discussed with P. Grütter. Ideas were also discussed with J. Topple, S. Fostner, M. Fendrich, and J.M. Mativetsky, who are gratefully acknowledged for their insights in the paper.

S.A. Burke, J.M. Mativetsky, S. Fostner, P. Grütter. C_{60} on alkali halides: Epitaxy and morphology studied by noncontact AFM. *Phys. Rev. B* **76**:035419, 2007. *Appears in Chapter 3*

J.M. Mativetsky and S. Fostner were also involved in data collection for this paper and were continually involved with operation of the apparatus required for these experiments. The concepts described and presentation of the data were discussed on an ongoing basis with all contributing authors.

S.A. Burke, W. Ji, J.M. Mativetsky, J.M. Topple, S. Fostner, H.-J. Gao, H. Guo and P. Grütter. Strain Induced Dewetting of a Molecular System: Bimodal Growth of PTCDA on NaCl. *Phys. Rev. Lett.* **100**:186104, 2008. *Appears in Chapter 4*

J.M. Mativetsky, S. Fostner and J.M. Topple were continually involved with operation of the apparatus required for these experiments. W. Ji performed the modelling of the experimental data in collaboration with H.-J. Gao and H. Guo.

The concepts described and presentation of the data were discussed on an ongoing basis with all contributing authors.

S.A. Burke, J.M. LeDue, J.M. Topple, S. Fostner, P. Grütter. Relating the functional properties of an organic semiconductor to molecular structure by nc-AFM. Submitted to *Advanced Materials*. *Appears in Chapter 4*

J.M. LeDue was also involved with the data collection and assisted with the implementation of the optical system required. J.M. Topple and S. Fostner were continually involved with the operation of the apparatus required for these experiments. The concepts described and presentation of the data were discussed on an ongoing basis with all contributing authors.

Acknowledgements

First and foremost, I would like to thank my supervisor Dr. Peter Grütter for his advice and guidance, his ability to inspire, and for giving me the freedom and support to pursue my research interests. Thank you for providing me with so many opportunities to learn and grow as a scientist.

I would especially like to thank Jeff Mativetsky, Shawn Fostner, and Jessica Topple with whom I worked on a daily basis. Thank-you for listening to my ideas, keeping the instrument running, the data flowing, and keeping me sane. Without your work, help, creativity and friendship this work would not have been possible. In particular, I would like to acknowledge Jessica for her contribution to the PTCDI work in the course of her training. I couldn't have asked for a better apprentice, your creativity and tenacity contributed immensely to this work and I know it will continue to serve you well.

I would also like to thank Yoichi Miyahara for assistance and for sharing his technical expertise and in-depth knowledge of SPM techniques on many occasions.

I would like to acknowledge the theoretical contributions of Wei Ji and Hong Guo which have significantly advanced our understanding of our observations. Thank-you for your interest and efforts in modelling the systems we study and for working so closely with us.

I would like to thank Simon LeFrancois for his work as a summer student involved with the molecular fluorescence project and purification of CuPc molecules.

I would like to acknowledge helpful discussions with Jorge Viñals and Martin Grant regarding the unusual growth morphologies of C_{60} on alkali halides. I would also like to acknowledge Roland Bennewitz for sharing his insights on force microscopy and epitaxy. Thanks also to Tobin Filleter and Philip Egberts for discussing force microscopy and sharing some fun and interesting experiments with me.

I would like to thank the members of the Grütter SPM group both past and present with whom I have worked for their ideas, help and friendship. It has been a wonderful experience, and I'm grateful to have met you all. I would like to especially thank Mehdi ElOuali for patiently helping me with french translations, both for the abstract in this thesis and at other times when needed. I would also like to thank Robert Gagnon and John Smernos for their technical assistance in keeping things running. Thanks guys!

I would like to thank Rolf Möller, Markus Fendrich and Tobias Kunstmann for hosting me in their lab at Uni Duisburg-Essen in Germany. It was a valuable experience both scientifically and culturally. I would also like to acknowledge Markus for his assistance in performing dissipation measurements during his visit to McGill and for his insights regarding dissipation measurements.

For financial support, I would like to acknowledge NSERC, FQRNT and the Walter C. Sumner foundation for funding my studies through various postgraduate scholarships.

I would like to thank my parents, who not being scientists have probably wondered what it is I do all day but have been wonderfully supportive anyway. Thank-you for your love and support, and for always encouraging me to explore the world around me and pursue what excited me.

Lastly, I would like to thank Jeffrey LeDue for being such a wonderfully supportive husband, as well as a brilliant scientist and colleague. It is not often one finds a partner in both life and science and I am so very, very lucky. Thank-you for your unwavering love and support, all the patient late nights in the lab, immensely productive scientific discussions, proof-reading, code-debugging, and for doing all the little things that kept me sane.

List of Abbreviations and Symbols

AFM	Atomic Force Microscopy/e
AM-AFM	Amplitude modulation Atomic Force Microscopy/e, also "Tapping" mode AFM
CPD, V_{CPD}	Contact potential difference
C_{60}	60 carbon cage molecule, "Buckminster Fullerene"
DFT	Density functional theory
EFM	Electrostatic Force Microscopy/e
FIM	Field Ion Microscopy/e
KPFM	Kelvin Probe Force Microscopy
LEED	Low energy electron diffraction
LD	Laser diode
LF-AFM/FFM	Lateral-force AFM / Friction Force Microscopy/Microscope
MFM	Magnetic Force Microscopy/Microscope
MM	Molecular Mechanics
NC-AFM/FM-AFM/DSFM	Non-contact AFM / Frequency modulation AFM / Dynamic Scanning Force Microscopy/e
OBD	Optical beam deflection
QPD	Quadrant Photodiode
RHEED	Reflection High Energy Electron Diffraction
SEM	Secondary Electron Microscopy/e
STM	Scanning Tunneling Microscopy/e
TEM	Transmission Electron Microscopy/e
UHV	Ultra high vacuum

A	Amplitude of cantilever oscillation
A	Area when referred to island morphology
a_i	Substrate lattice constant
α	angle between a_1 and a_2
b_i	Overlayer lattice constant
β	angle between b_1 and b_2
$[\mathbf{C}]$	Matrix describing overlayer relation to substrate lattice
c_N	Normal mode spring constant of cantilever
c_L	Lateral or torsional mode spring constant of cantilever
D'	2-dimensional fractal dimension
δf	Error in frequency measurement
Δf	Measured/set-point frequency shift
Γ	Normalized frequency shift
γ_0	Intrinsic damping of the oscillator
E	Young's modulus
F_{int}	Tip–sample interaction force
f_0	Natural/free resonant frequency of cantilever
f_{mod}	Frequency of the bias modulation for KPFM
F_N	Normal force/load
F_L	Lateral/friction force
P	Perimeter
Q	Q-factor of the cantilever
$S.F.$	Shape factor
τ	Time constant

Contents

List of Figures

List of Tables

1

Introduction and Background

"A biological system can be exceedingly small. Many of the cells are very tiny, but they are very active; they manufacture various substances; they walk around; they wiggle; and they do all kinds of marvelous things – all on a very small scale. Also, they store information. Consider the possibility that we too can make a thing very small that does what we want – that we can manufacture an object that manewers at that level."

– Richard P. Feynman "There's Plenty of Room at the Bottom" delivered at the annual meeting of the American Physical Society, California Institute of Technology, CA December 1959. [1]

1.1 Nanoscience and Nanotechnology

Smaller is better? It is perhaps obvious in today's technologically driven society that one would strive for ultimate miniaturization of electronics and construct devices on a nanometer length scale: as devices shrink, capacity increases. Current silicon transistor technologies have already crossed below the 100nm gate length mark with today's processors containing upwards of 1 billion transistors giving processor speeds 10,000 times faster than computer systems made 35 years earlier [2]. The consumer drive for increased computer power continues to push technologies to smaller scales.

However, there is a far more compelling reason to look to nanoscale objects, which is that a wealth of exciting new properties arise as a result of reducing objects to such small sizes. This fundamentally different paradigm introduced by nanoscale objects, reached as numbers of atoms become small, is both a burden and an enormous opportunity. At nanometer length scales, classical scaling may

break down and for technology to proceed we must learn to understand the behaviour of materials in the "nano" regime. On the other hand, this new behaviour, often tuneable by size and entwined with quantum behaviour, has potential to revolutionize many technologies; not only computing and electronics, but from nanomedicine to novel new materials [3, 4]. Already, examples of nanoscale approaches are making their way into news headlines and real products including: carbon nanotube composites for lighter, stronger materials, perhaps in your next tennis racquet [4, 5], nanofiber cloths for the detection of biohazards [4, 6], and plasmonic nanoparticles to be used for diagnoses and treatment of cancer tumours [7]. *Such is the promise of "nano".*

1.2 Using molecules as functional components

Millions of identical nanoscale objects: molecules. Chemists have been in the business of nanoscience since the first alchemists strove to transmute the elements and cure disease. Molecules are naturally nanoscale objects whose properties can depend as much upon the number and arrangement of atoms as on their atomic constituents alone. Synthetic chemistry is a powerful tool for nanoscience, providing avenues to build in specific function by chemical design. Indeed, as noted in Richard Feynman's now famous lecture "There's plenty of room at the bottom"[1], nature does precisely this, by modifying molecular building blocks to provide the necessary functionality for biological operation (see example of porphyrin derivatives in figure 1.1).

Based on the concept that *electronic* function, perhaps as complex as logic, could be built into molecules, in 1974 Aviram and Ratner [8] proposed the idea of molecular electronics with an example of a possible molecular rectifying diode. With the introduction of scanning probe microscopy in the early 1980's [9, 10, 11, 12] providing the ability to see and manipulate objects on nanometer scales there has been considerable scientific effort put towards the investigation of molecular materials, both single molecules [13, 14] and molecular thin films [15, 16, 17, 18, 19], as electronic and opto-electronic components for device applications. The issues and challenges associated with each are briefly outlined here to provide some context for the investigation of molecular growth.

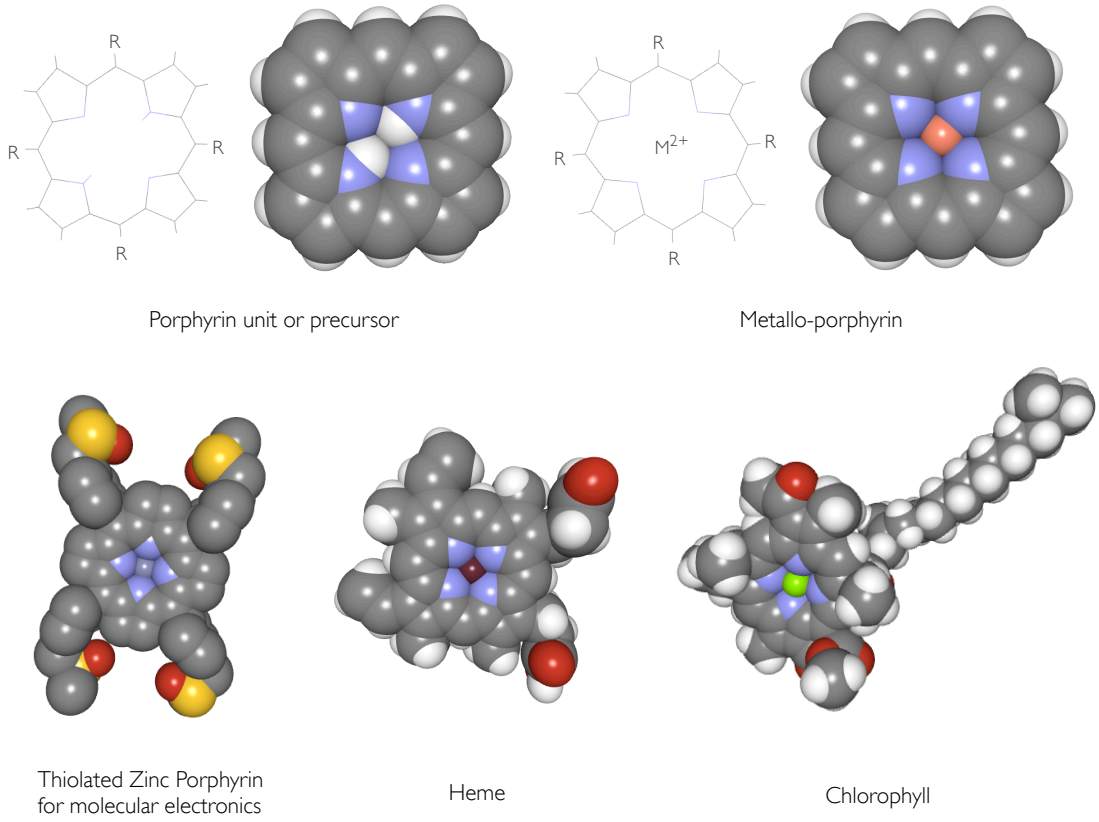

Figure 1.1: Variations on a theme: examples of porphyrin structures. Top: a porphyrin unit with no metal ion, sometimes referred to as a "porphyrin precursor", and a porphyrin with a metal ion in the center of the ligand. Both of these structures can be functionalized with a variety of different groups or with different metal ions to produce different properties and functionality. Below: examples of different porphyrins. The thiolated zinc-porphyrin 5,10,15,20 Zn^{2+}-tetrakis-3-5-acetyl-methyl-phenyl porphyrin designed for molecular electronics applications, and two examples from biology: Heme, a component of hemoglobin in the blood critical to oxygen transport through the human body, and Chlorophyl, which plays a vital role in plant photosynthesis.

Single molecule electronics

While chemistry provides a means for producing molecular species which may have desirable device properties, the challenge of interacting with a nanoscale object remains. The practice of electrically contacting a molecule which may be no more than a nanometer in size is certainly a daunting technical challenge, however, it also requires some conceptual consideration as well. For a molecule connected to nanometer scale metal electrodes, those metal atoms bonded to the molecule become rather indistinguishable from the molecule, with states extending across the metal–molecule interface [20, 21]. As a result, the properties of a single molecule junction are highly sensitive to the local electrode structure and composition (eg. contamination) producing highly variable results. Commonly today, single molecule junction measurements are performed using histograms of large numbers of repeated conductance measurements by breaking and reforming the junction [22, 23, 24, 25] allowing better comparison to theory [13], however the reproducibility and dependance on local structure of single molecules measurements still remains a pivotal issue in single molecule electronics. Additionally, molecular species are highly sensitive to their local environment, for example a substrate, which can influence the electronic structure of molecule through charge transfer and local electrostatic fields. Ideally, single molecule conductance measurements would be performed with a detailed knowledge of the atomic structure of the electrodes at the gap, bonding to the molecule, and the influence of the local environment such as a substrate.

While the details of the molecule–substrate interaction and precise adsorption sites and geometries are important in terms of the properties of such a molecular device, another key issue is positioning a molecule on a surface near contacts. This design issue relies on a knowledge of the surface science of molecules on the substrate of interest, as well as the interaction of the molecule with deposited structures and how these interactions compete. Thus, thorough understanding of the epitaxy, nucleation and growth of molecules on the insulating supports that will be required are an important basis for the design and understanding of future planar molecular devices.

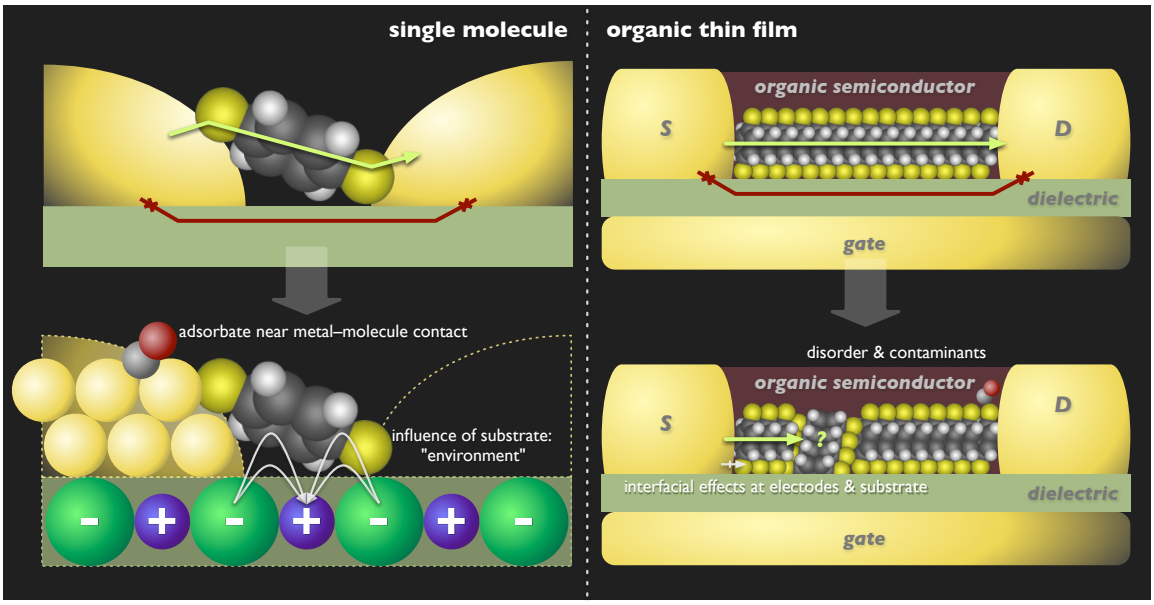

Figure 1.2: "Cartoon molecular devices" showing concept and need for insulating substrates (top pane) and illustration of some of the issues concerning real devices.

Thin film organic electronics

While the *local* environment of an individual molecule in a large area thin-film organic device is of less importance, the film structure and interface effects are known to influence the properties of the film and thus device performance [17, 16, 18, 19]. In particular, the presence of grain boundaries is known to influence transport properties [19] and different crystallographic structures may have different electrical characteristics. In particular, the interfaces between molecular materials and electrodes, gate dielectric, and between donor and acceptor materials (eg. for photovoltaics) are known to be of critical importance. For example, in organic field-effect transistors the majority of conduction occurs within the first few molecular layers [17] indicating that the structure and resulting properties at this organic–insulator interface are of critical importance in optimizing device performance.

Despite these outstanding issues, thin-film organic devices are progressing from the realm of science into technology, even so far as reaching market for a

few applications and attracting great interest in many areas [18, 26]. Still, a greater understanding of the influence of structure on electronic and opto-electronic properties, which will be discussed in section 4.3, may prove significant for optimizing such devices and pushing organics further into areas where conventional semiconductor technologies still dominate.

Molecules and Insulators

In both cases, a use of insulating substrates is necessary for the isolation of device regions. To avoid short circuits and to ensure that the current measured is travelling along the expected path, the band gap of these insulating regions should be significantly larger than any applied bias voltages, and thick enough to prevent tunnelling. Ideally, the electronic states of the molecule and substrate will not be influenced upon adsorption to aid in the prediction and understanding of device properties. Despite the crucial dependence of molecular devices on local environment and interfaces there has been little study concerning molecular growth on insulating substrates.

1.3 Molecular growth

1.3.1 Investigating molecular growth on insulating substrates

Both molecular materials and insulating substrates present special challenges to experimental surface investigation. The majority of surface science tools rely on the use of electron beams (electron diffraction: LEED and RHEED, electron microscopy: SEM, (S)TEM, LEEM, and SAM). However, molecules may undergo damage such as dissociation under electron irradiation changing the species investigated, and may also suffer from charging issues making data collection and interpretation difficult even when metal substrates are used. Similarly, bulk insulating crystals suffer from issues with charging and damage [27] when exposed to electron beams, severely complicating data collection and interpretation. X-rays and UV light (eg. in photoemission experiments to determine electronic structure) can also be used to probe surface structures, however, many molecules may also be sensitive to these [28] and may also damage insulating crystals such as alkali

halides (eg. producing colour centers) [27] and oxides [29] and cause charging in photoemission measurements [30].

While scanning tunnelling microscopy (STM) has contributed significantly to the understanding of molecular growth and epitaxy on conducting surfaces (metallic and semiconducting) [31, 32, 33], due to the requirement that a current be measured through the substrate, it cannot be applied to bulk insulating substrates. In order to perform studies on molecules on insulating surfaces with STM, insulating thin films have been used successfully [21, 34, 35, 36] with excellent results. However, by the very requirement that tunnelling be maintained across the insulating layer, interactions between the molecules on the film and the underlying conducting substrate may extend through the film, and examples have been reported where there is evidence of such influence [37, 38]. Also, since tunnelling through the insulating layer is possible, the use of this technique for application in molecular electronics is of some concern.

Alongside STM, noncontact (nc-) or frequency modulation (FM-) atomic force microscopy (AFM) has been been used for atomic scale imaging in UHV since 1995 [39, 40], particularly for the study of insulating surfaces [41, 42, 43, 44, 45, 46, 47, 48]. More recently, this technique has been applied to the high resolution imaging of molecular deposits on insulating crystals with considerable success [49, 50, 51, 52, 53, 54, 55, 56, 57]. The ability to image with high resolution both insulating crystals and organic deposits using nc-AFM provides a powerful tool for structural characterization of molecules on insulators circumventing the complications of insulating thin films or issues faced by electron techniques with damage and charging. Additionally, electrostatic forces can be detected, even to the sensitivity required to detect single electron events [58], providing methods for probing properties of organic films [59, 60] which will be discussed in section 2.2.3. The study of growth of molecules on insulators in this thesis applies high-resolution nc-AFM in UHV for both structural characterization as well as a novel application of a hybrid optical-electrostatic characterization for the connection between structure and optoelectronic response (see section 4.3).

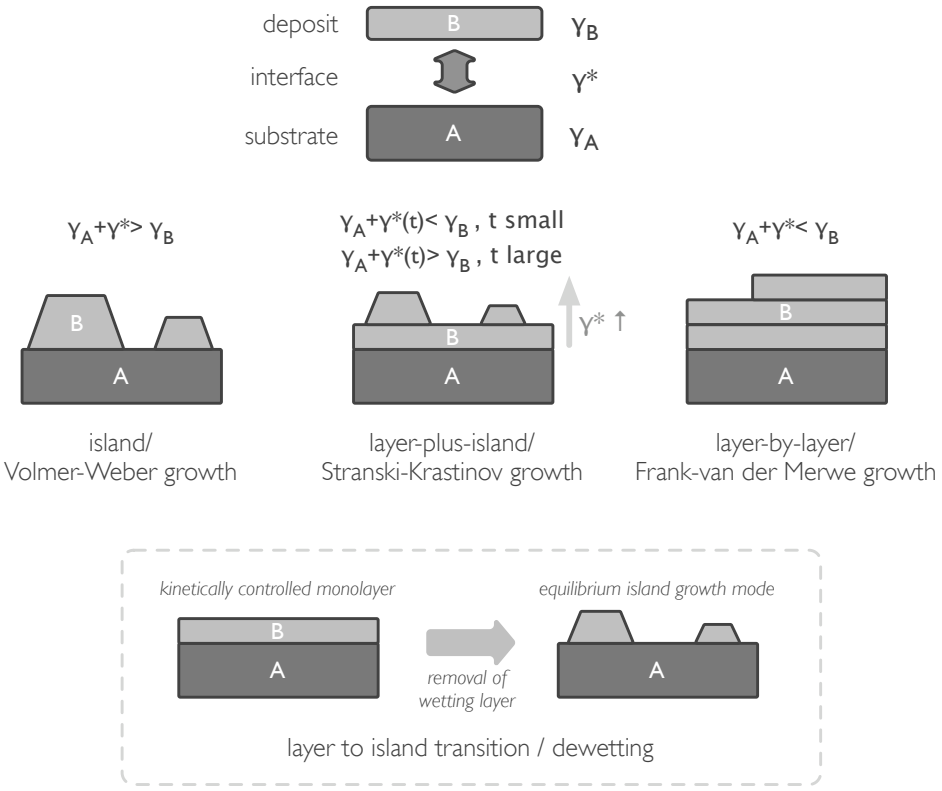

Figure 1.3: Growth modes and related surface free energies (labelled, top). The three common growth modes, island/Volmer-Webber, layer-plus-island/Stranski-Krastinov, and layer-by-layer/Frank-van der Merwe with respective balances of surface energies. Below, schematic of a dewetting transition from layer to island.

1.3.2 Growth modes and dewetting

Surface thermodynamics dictates the equilibrium growth modes of deposited materials based on the balance between the surface free energies of the substrate and the deposit, γ_A and γ_B respectively, and the interface energy, denoted as $\gamma*$. This gives rise to three different growth modes [61]:

Island/Volmer–Webber growth: Atoms nucleate small clusters on the substrate surface which grow into islands of the condensed phase of the deposit material. In terms of the surface free energies: $\gamma_A + \gamma^* > \gamma_B$, ie, the atoms of the deposit material are more strongly bound to each other than the substrate. Thus, a supersaturation of deposit atoms is needed to induce nucleation.

Stranski–Krastinov: Deposited atoms initially form sequential complete layers due to a strong interaction between the deposit atoms and the substrate, such that $\gamma_A + \gamma^*(t) < \gamma_B$ when the thickness of the film is small. As more material is deposited, the interface energy, γ^*, increases making subsequent layer growth *unfavorable*. At this point, the condition for island growth is satisfied, and the material continues to deposit only if there is a supersaturation of the deposit atoms. Typically the increase in the interface energy is due to strain in the first few layers.

Layer–by–Layer/Frank–van der Merwe: Atoms are more strongly bound to the substrate than each other and first condense to form a complete layer. Provided the binding energy of subsequent layers decreases monotonically with coverage approaching the bulk crystal value, the deposit material will continue to grow in a layer-by-layer fashion. In terms of the surface free energy: $\gamma_A + \gamma^* < \gamma_B$.

Under what seems as though it should be exceptional circumstances, a transition can occur between layer growth and island growth by reordering of the existing initial layer. This transition, known as "dewetting", can be triggered by annealing [62], increasing thickness of the deposit [63, 56], or apparently spontaneously as a result of the change in kinetic conditions between growth and ripening [55]. In all cases, it is supposed that the ordering of the deposit grown in a layer is altered, usually as a result of underlying strain, by which the balance of surface energies is shifted to favour the different growth mode. While similar to Stranski-Krastinov growth in the progression of surface energies, the dewetting scenario differs as a more extreme case whereby the wetting layer is removed. Dewetting is also thought to be a kinetically driven process as the initial layers formed are typically metastable, hence they are removed by annealing or other changes in conditions.

Due to the propensity of molecular systems to form multiple structures, polymorphs in the bulk and polymorphic or multiple epitaxies in film growth, and the ability of molecular lattices to accomodate large strain compared to inorgnaic lattices, the conditions for dewetting appear to be more often met for molecular deposits. In addition to the examples discussed in this thesis, there are increasing

numbers of examples in the literature, for example: perylene on Au and Cu [62], pentacene on Au [64], phenylthiophene fulgide on glass [65], diindenoperylene on SiO_2 [66] and 3,4,9,10-perylene tetracarboxylic dianhydride on Ag(111) [66]. The unique considerations for molecular growth leading to these conditions are discussed next.

1.3.3 Interactions of molecules at surfaces

While chemical bonding interactions require specific case-by-case treatment, the physical adsorption, physisorption, of molecules can be discussed in somewhat more general terms. Although these interactions also have some specificity and can be treated in great detail through methods such as molecular mechanics (MM), the general classes are worth considering to provide some sense of how molecules interact at surfaces.

In considering the cases of different types of molecules to be adsorbed on ionic surfaces there are three types of physisorption interactions which should be considered as were described by deBoer in 1950 [67]:

Non-polar van der Waals forces (also dispersion forces, or fluctuating dipole forces) which add to the interaction energy the familiar r^{-6} term, and higher order terms for additional multipoles which are usually negligible and omitted.

Polar van der Waals forces (or electrostatic interaction forces, as they will be referred to in this thesis) arising from the static charge distribution in the molecule and on the surface. For a dipolar molecule this gives rise to an interaction term: $V_\mu = -\vec{E}_{surf} \cdot \vec{\mu}$, where $\vec{\mu}$ is the dipole moment of the molecule and $\vec{E}_{surf}$ is the electrostatic field over the surface.

Induced van der Waals forces (also considered under electrostatic interaction forces producing an induced ionic-like interaction) arise from a polarization of the adsorbed species as a result of the electrostatic field of the surface. To first order, this adds an interaction term: $V_\alpha = -\vec{E}^2_{surf}\alpha/2$, however this tends to underestimate the contribution and a more precise estimate can be obtained by integrating the contribution over the volume adsorbed species which takes into account the spatial dependance of the field and the polarizability. While

this term is typically weak for atomic adsorbates, the net contribution from a larger polarizable molecule may be significant, and this term is also expected to contribute significantly at "special" sites such as defects and step edges which produce a larger field.

It is important to note the latter two of these contributions to physical adsorption with regards to a molecule on an ionic surface. Molecular species are often not uniformly charged but have some electrostatic moment which will interact with the surface. Additionally, ionic crystals, such as alkali halides, produce an electrostatic field with which the molecules will interact, either through a permanent partial charge distribution or through an induced moment in a polarizable molecule. While these terms are often not considered for atomic systems, they are likely to play a more significant role in the overall adsorption energy of molecules on ionic surfaces, and in particular in governing adsorption geometries. While detailed calculations are better suited to determining adsorption energies and geometries for specific systems, consideration of these additional contributions may act as a guide to understanding how different types of molecular species may interact with ionic crystal surfaces.

1.3.4 Special features of molecular growth

While many aspects of inorganic growth can be applied to molecular growth, there are a number of special issues which should be taken into consideration when characterizing the nucleation, epitaxy, and growth of organic materials. A key difference between atomic growth processes and molecular growth is the fact that molecules are extended objects which gives rise to internal degrees of freedom, orientational effects, and large area potentials. Also, the interactions between molecules, and between molecule and some substrates, is typically dominated by van der Waals and electrostatic interactions, rather than covalent bonding leading to weaker, softer interactions. There are many excellent reviews [15, 31, 68, 66] on molecular growth by vacuum deposition, also referred to as organic molecular beam epitaxy (OMBE) or organic molecular beam deposition (OMBD), however, the principle considerations are outlined here:

- ▷ As extended objects, *molecules can have well defined orientation*, which should

be considered when discussing molecular lattices. Geometrical parameters such as tilt angle from the surface as well as in-plane orientations give additional complexity to epitaxy and crystal structures of organic thin films, which may also give rise to changes in growth mode such as dewetting and roughening [66]. See fig. 1.4 first two panels.

- ▷ The presence of *internal degrees of freedom*, again a result of the molecule being an extended object, including conformational degrees of freedom, allow distortions of the molecule upon adsorption and vibrational degrees of freedom which may change kinetic conditions during growth can both influence film morphology and structuring. In particular, when modelling molecular epitaxy the inclusion of conformational degrees of freedom can lead to additional compliance of the lattice to accommodate surface induced strain. See fig. 1.4 third panel.

- ▷ As a result of the primarily *van der Waals interactions* between molecules, molecular lattices are typically much more *compliant* than inorganic lattices. However, due to integration over all atoms, binding energies may still be large ($\sim$1 eV range). [66]

- ▷ Similarly, for molecules adsorbed on inorganic substrates, the size of the molecule is often larger than the size of the substrate unit cell. This results in *large area adsorption potentials* which are similarly softer despite reasonably large adsorption energies. Also, these large area potentials give rise to translational domains as the atomic corrugation of the lattice is often much smaller than the molecule. See fig. 1.4 fourth panel.

- ▷ This *mismatch in size and geometry* between molecules and inorganic substrates combined with relatively soft molecule–molecule and molecule–substrate interactions also results in more frequent *coincident epitaxies*, rather than commensurate lattices [31]. For a description of different types of commensurate epitaxy and nomenclature for describing these epitaxies see Appendix E.

These issues, which primarily effect the structure of the film, provide the basis for film growth, and can lead to a variety of different domains influencing

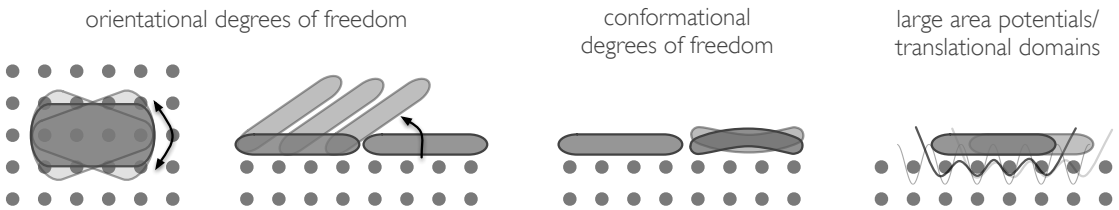

Figure 1.4: Schematic representation of some of the issues concerning molecular epitaxy and growth. From left to right: in-plane orientation, out-of-plane orientation or tilt angle, conformational freedom or deformation of molecules, and large area potentials resulting in soft but deep wells and leading to translational domains.

further film growth. An understanding of these underlying structures provides a foundation for understanding further growth processes, and is the principle reason for undertaking submonolayer growth studies in the context of film growth. Other processes such as diffusion and transitions between structures can lead to interesting morphologies. For example, the prevalence of mesa-like islands, islands with relatively flat tops and steep edges, in molecular growth have recently been attributed to differences in ascending and descending diffusion processes for molecular islands. In particular, the ascending process is dominated by differing effective binding energies at each layer as a result of strain [69]. In more extreme cases, the strain [56] or the presence of a transient structure [66] may result in roughening (also, Stranski–Krastinov growth) or dewetting of the initial film growth as described in the previous section, which will be a principle topic of this thesis.

1.3.5 Questions in molecular growth on insulators

Given the lack of appropriate investigative tools for probing molecular materials on insulating substrates, there is a great deal yet to be learned regarding molecular growth on insulators. Growth modes, morphologies, and kinetically controlled structures will dictate features important for thin film organic electronics such as grain boundaries and molecular orientations at interfaces. We must ask *what processes dominate adsorption and growth of organic materials on insulating surfaces?*

Additionally, the detailed adsorption geometries which underlie these larger scale structures are equally unknown and will also be of importance to the assem-

bly and properties of a single molecule device. Related to these adsorption geometries is the nature of the molecule–insulator interaction. What are the dominant interaction mechanisms? Are they the same as on metals and semiconductors, or do a different set of interactions have to be considered? More importantly, is an ionic substrate (of which all insulators have some ionic character) benign towards molecular states and vice versa allowing the system to preserve the properties of each separately? Or must we consider the system as a whole (molecule + electrodes + substrate) when predicting and designing device characteristics?

This thesis attempts to begin to address these issues through the characterization of epitaxy and growth of a series of organic molecules considered relevant to molecular electronics. Ionic crystal substrates are chosen as prototypical insulating substrates for practical experimental reasons, and while not typically used for technological purposes should share many commonalities with surfaces which are used for device applications. The technique of nc-AFM permits atomic-scale imaging of surfaces including insulators allowing detailed real-space structural characterization, similar to that of STM on conducting surfaces which has provided invaluable data regarding molecules on those surfaces.

1.4 Prototype systems

In order to investigate the effects of different molecular shapes and charge distributions on epitaxy and growth, a series of molecules considered relevant for molecular electronics were selected: C_{60} , 3,4,9,10-perylene tetracarboxylic dianhydride (PTCDA), 3,4,9,10-perylene tetracarboxylic diimide (PTCDI) or perylene tetracarboxylic bisimide (PTCBI), and copper (II) phthalocyanine (CuPc). This range of molecules, all of which are well studied on a variety of other surfaces, allows modification of the intermolecular interactions as well as interactions with the substrate. Each system is introduced in detail at the beginning of the relevant sections.

Alkali halide substrates, specifically KBr and NaCl, were selected as prototypical insulating surfaces due to their highly crystalline surface structure, and the ability to cleanly prepare these surfaces by cleavage in UHV. Freshly cleaved surfaces typically have defect free atomically flat terraces ranging from 100nm–1.5μm

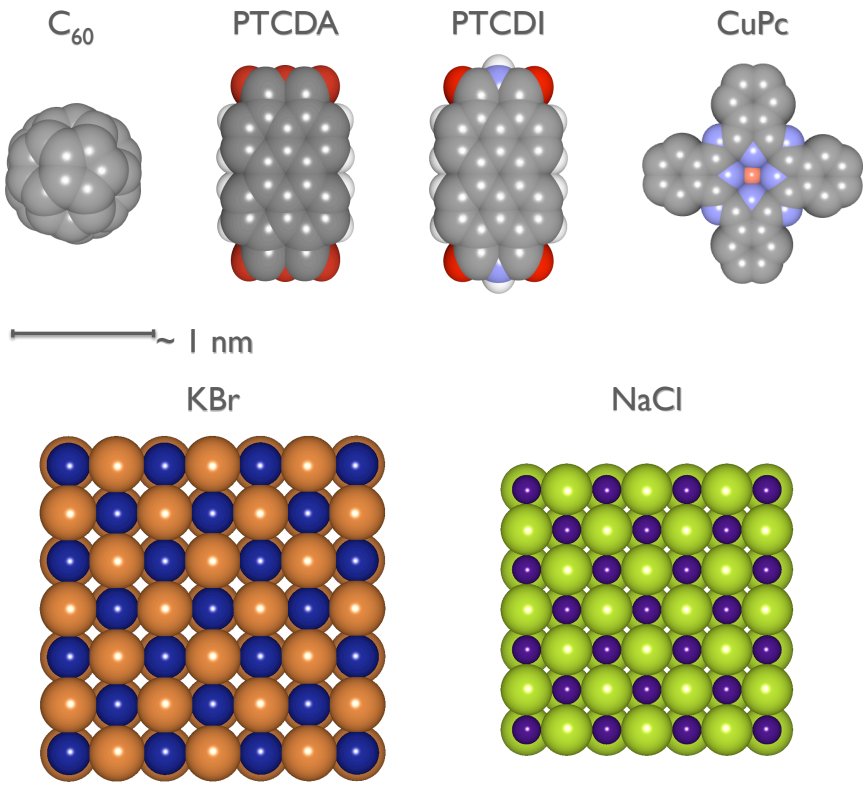

Figure 1.5: Scale representations of the molecules and substrates used in growth studies. Van der Waals radii shown for molecules [70] and ionic radii shown for ionic substrates [71].

providing an excellent basis for growth studies. The ionic lattice of these surfaces is readily resolved by nc-AFM which permits the determination of epitaxy of the molecular overlayer in most cases which is expected to lead to an improved understanding of the molecule–substrate interaction.

While alkali halides might seem of limited technological relevance, their ionic character is common, at least to some degree, in many insulators, including oxides. The basic insights gained regarding the molecule–substrate interaction and growth behaviour of molecules on alkali halides are expected to share common aspects as a result of this similarity.

2

Experimental methods

2.1 Operating principle of Atomic Force Microscopy

The basic operating principle of the atomic force microscope is the detection of forces on the nanoscale, with a local probe which is scanned over the surface of interest. As with other scanning probe microscopy techniques, a local probe, or "tip", is scanned in close proximity to the surface and either the signal of interest is recorded as a function of position (constant height mode), or the distance dependant signal is used to regulate distance with a positioner via a feedback circuit (topographic mode).

Typical implementation schemes of AFMs use a sharp tip attached to a small cantilever, now generally made of microfabricated silicon (see fig. 2.1), which reduces the problem of force sensing to one of detecting the deflection of this small spring. Various deflection detection schemes are applied including interferometry, electrical readout of a piezoelectric cantilever, and, most commonly, optical beam

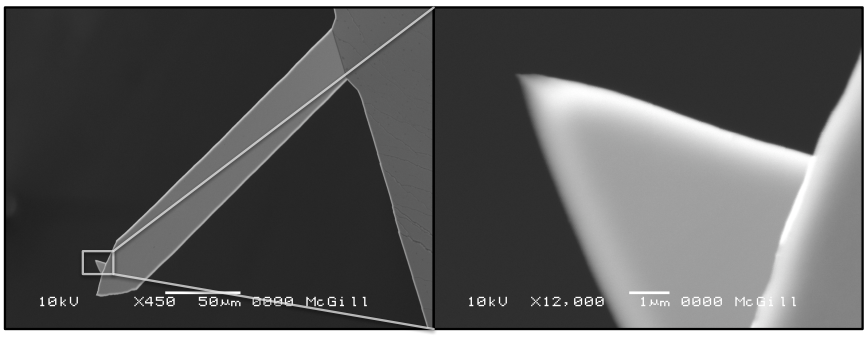

Figure 2.1: *In situ* SEM images of a commercially available microfabricated silicon cantilever used for nc-AFM or tapping mode imaging. (Nanosensors Point probe plus-NCLR)

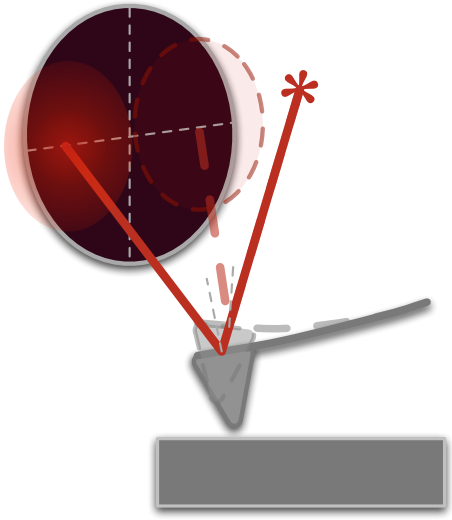

Figure 2.2: Optical beam deflection technique for detecting the deflection of an AFM cantilever. A focused laser beam is reflected off the back of the cantilever and onto a split or quadrant photodiode (PD). As the cantilever deflects, the angle of the reflected beam changes resulting in a different position of the beam on the PD which reads as a change in the difference voltage of the two halves.

deflection [72]. A piezoelectric drive is usually used for scanning the tip in x and y and tracking the z-direction.

Various modes of AFM have been developed since its inception in 1986 [11]. The most common is the static deflection, or "contact" mode. In this method, the tip is approached to the surface until a repulsive tip–sample interaction causes the cantilever to deflect. The deflection is then linearly related to the force through the spring constant, making this mode relatively straightforward to understand and interpret. As the tip is then scanned across the surface either the deflection is recorded, or maintained constant by controlling the z-position. This is the most intuitive method as it is akin to "feeling" a surface (see fig. 2.3). If a very soft cantilever is used, sensitive measurements can be made and destructive forces can be reduced. However, the DC measurement of deflection suffers from noise issues, the tip and sample are subject to wear in the repulsive regime, which is usually used, and lateral forces on the sample can be significant.

As an off-shoot of contact mode AFM, lateral force microscopy (LFM) or friction force microscopy (FFM) can provide information regarding lateral forces and friction between the tip and the sample surface by recording the lateral deflection as well as keeping the normal deflection constant for a constant normal force. This technique has been applied extensively for the study of atomic scale friction and wear [74, 75].

To circumvent the problems arising from low frequency noise in the de-

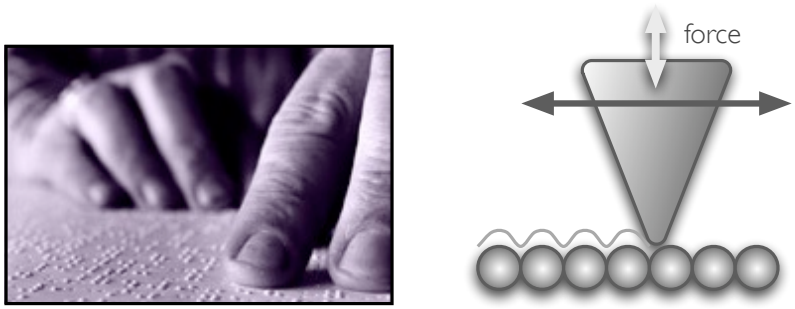

Figure 2.3: Touch vs. AFM: a sharp tip attached to a force sensor is scanned across the surface, much like a person feeling across a surface with their fingers to determine shapes and textures by touch. (Image in (a) from CNIB [73]).

flection measurement and to reduce undesirable lateral forces, dynamic modes of AFM have also been developed, which is the topic of the following sections.

2.2 Dynamic Modes of Atomic Force Microscopy

2.2.1 Cantilever motion

In dynamic modes of AFM, a cantilever with a sharp tip is positioned in close proximity to the surface to be investigated and is mechanically excited at or near resonance. The equation of motion of such a driven cantilever in the presence of a tip–surface interaction force can be expressed as:

$$\underbrace{c_N x_N(t)}_{restoring\ force} + \underbrace{\gamma_0 \dot{x_N}(t)}_{intrinsic\ damping} + m_{eff}\ddot{x_N}(t) = \underbrace{F_{int}(x)}_{interaction\ force} + \underbrace{F_{exc} cos(\omega_{exc} t + \phi)}_{driving\ force} \quad (2.1)$$

where the restoring force of the cantilever spring, intrinsic damping of the cantilever, the tip–sample interaction force and the driving force used to excite the cantilever are included. Note that if there are non-conservative terms in the interaction force or if an external signal proportional to the velocity of the cantilever is added (see Appendix C for example of this), that these will appear in the solution of the cantilever motion as dissipative terms or out of phase components of the

resulting oscillation. These non-conservative terms can often give rise to materials contrast due to differing visco-elastic properties, or differing adhesion between the tip and sample. Indeed, it has recently been shown that the dissipation signal in nc-AFM imaging can be used to distinguish between different atomic sites on a semiconductor surface [76] demonstrating the applicability of this concept down to the atomic scale.

The natural resonance frequency in the absence of the tip–sample interaction is given by:

$$f_0 = \frac{1}{2\pi}\sqrt{\frac{c_N}{m_{eff}}} \simeq \frac{1.8373^2 t}{4\sqrt{3}\pi l^2}\sqrt{\frac{E}{\rho}} \tag{2.2}$$

where c_N and m_{eff} are properties of the geometry and materials of the cantilever, and for a rectangular cantilever, f_0 can alternately be written in terms of the length, l, and thickness, t of the lever and the Young's modulus, E and density, ρ of the cantilever material. Similarly, the normal mode spring constant can be written in terms of the geometry and material properties of the cantilever:

$$c_N = \frac{Ewt^3}{4l^3} \tag{2.3}$$

where E, t and l are as above, and w is the width of the cantilever. While in principle the spring constant can be determined from these parameters, or measured [77, 78], in practice the values for cantilevers from a particular wafer are quite consistent and as such the stated values provided with a wafer are used here. This is generally acceptable unless highly sensitive quantitative force analysis is required.

The cantilever tip held close to the surface typically experiences a sum of forces arising from short range chemical interactions, van der Waals interactions, and electrostatic interactions (see fig. 2.4). The latter two give rise to significant long range attractive forces which often overwhelm the short range chemical interaction responsible for atomic resolution. Figure 2.4 also demonstrates another challenge of AFM which is that the force, and related quantities to be used for feedback, is non-monotonic, thus stable feedback can only be achieved on a particular branch of the imaging signal [79]. It should also be noted, that the functional dependence of the feedback signal is not fixed, as in STM where an exponential decay is always present, but depends upon the properties and geometry of the tip and

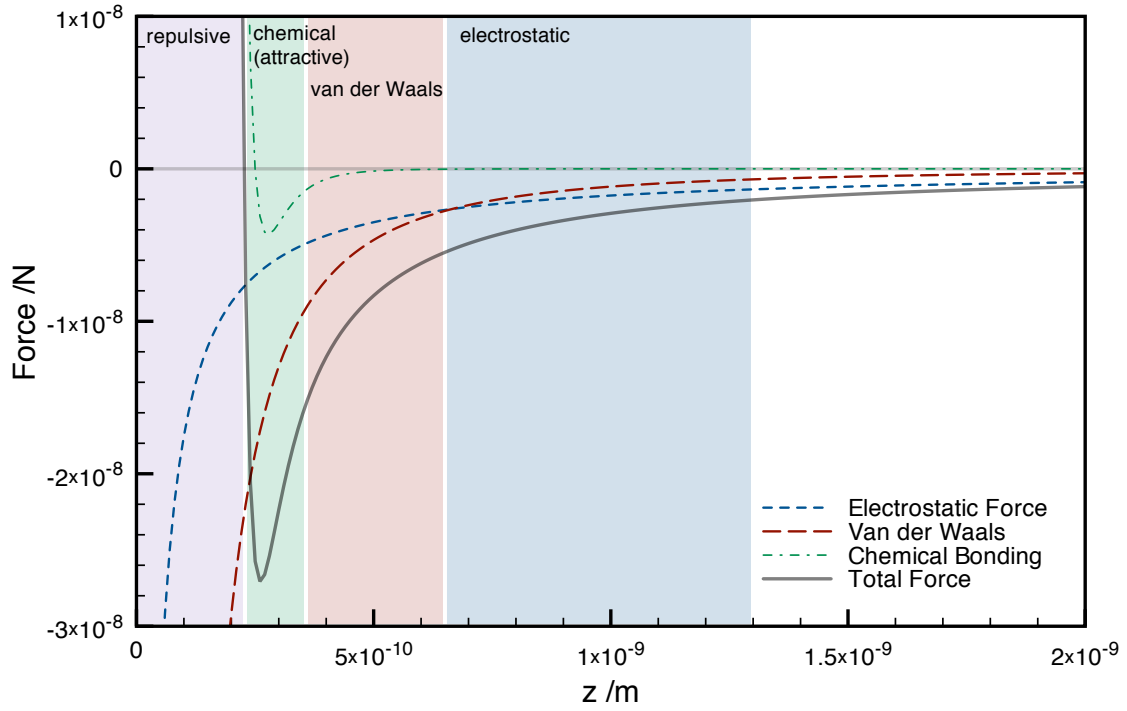

Figure 2.4: Plot of typical AFM imaging forces as a function of tip–sample separation (z). The long range electrostatic and van der Waals forces contribute the greatest extent to the sum of forces, overwhelming the short-range chemical interactions until nearly repulsive. This presents a significant challenge for AFM as these short range chemical interactions are what typically give rise to atomic resolution.

sample.

The electrostatic force on the cantilever can be expressed in general in terms of the capacitance gradient and the potential difference between tip and sample:

$$F_{el} = \frac{1}{2}\frac{\partial C}{\partial z}V^2 \tag{2.4}$$

where $V = V_{bias} - \frac{\Delta\phi}{e}$ where $\Delta\phi$ is the work function difference between the tip material and the sample material [80], and $\Delta\phi/e$ is often referred to as the **contact potential difference** (CPD, or V_{CPD}). This means that even with no external bias

applied and no trapped charges present there may be an electrostatic force present due to the difference in work function between tip and sample materials. However, by applying the appropriate bias the electrostatic force can be nulled, and this is often done for FM-AFM imaging. Assuming a spherical tip a distance z above an infinite plane this reduces to:

$$F_{el} = -\pi\epsilon_0 \left(\frac{R^2}{z(z+R)}\right) U^2 \approx -\frac{\pi\epsilon_0 R U^2}{z} \tag{2.5}$$

where R is the radius of the spherical tip, and the approximation that $z \gg R$ is often made [79]. It is worth noting that the value of the tip radius determined from fitting the electrostatic contribution to the force is often larger than the expected microscopic tip radius, and the capacitance may even vary with distance transitioning from a sphere-like dependence to a parallel-plate like dependence [81]. This implies that more than just the tip apex is involved in this long range force, and that the contribution of different parts of the tip/cantilever also depends upon distance which may complicate the interpretation of capacitance measurements if not carefully considered.

The other long range force arises from van der Waals interactions and unlike the electrostatic force cannot easily be reduced except in liquid environments. The form of the van der Waals potential for a sphere and an infinite plane is given by:

$$V_{VdW} = -\frac{A_H R}{6z} \tag{2.6}$$

where A_H is the Hammaker constant which encapsulates the effects of the atomic polarizability and density and is a property of the materials of the tip and sample, typically of the order of 1eV [79] (for a detailed description and tables of values for different materials see [82]). This gives rise to a force [83]:

$$F_{VdW} = -\frac{A_H R}{6z^2} \tag{2.7}$$

For a more general expression of the van der Waals interaction and force for different tip–sample geometries see [84].

The chemical/short range interactions are usually empirically modelled by

either a pair-wise Leonard-Jones or Morse potential, both of which can be expressed in terms of a bond energy, E_{bond}, and an equilibrium distance σ. The Leonard-Jones potential is given by [84]:

$$V_{L-J} = -E_{bond}\left[2\left(\frac{\sigma}{z}\right)^6 - \left(\frac{\sigma}{z}\right)^{12}\right] \tag{2.8}$$

which gives rise to a force:

$$F_{L-J} = -12\frac{E_{bond}}{\sigma}\left[2\left(\frac{\sigma}{z}\right)^7 - \left(\frac{\sigma}{z}\right)^{13}\right] \tag{2.9}$$

The Morse potential describes the bonding dependence as an exponential decay [79]:

$$V_{Morse} = E_{bond}[2e^{-\kappa(z-\sigma)} - e^{-2\kappa(z-\sigma)}] \tag{2.10}$$

where κ is the decay length of the bonding interaction and must be determined for the pair of atoms under consideration from spectroscopic data [85]. This gives rise to a force in the z-direction:

$$F_{Morse} = 2\kappa E_{bond}[2e^{-\kappa(z-\sigma)} - e^{-2\kappa(z-\sigma)}] \tag{2.11}$$

Most often the Leonard-Jones potential is used, however, in some cases the exponential dependence of the Morse potential may describe the interaction more closely.

If the details of the sample and tip are known, atomistic simulations can also be used to model the interactions between tip and sample. This is often done to gain understanding of contrast mechanisms, however, as this requires *a priori* knowledge of both sample and tip, the later of which is often not known at the atomic scale, usually many different tip structures and compositions must be modelled to compare with experiment [79, 86]. More recently efforts have turned towards the possibility of exploiting the unique nature of chemcial interaction as an atomic fingerprint to perform the identification of atoms through a combination of modelling [87] and force spectroscopy, which has now been realized experimentally [88].

These tip–sample interaction forces can be detected in two ways in a dy-

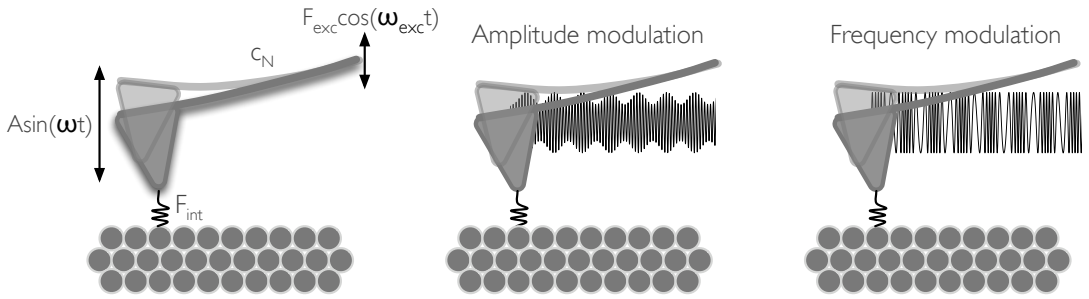

Figure 2.5: The cantilever and tip–sample system labelled with variable definitions from eqn. 2.1. Schematics of amplitude modulation and frequency modulation methods.

namic mode: amplitude modulation (AM) or frequency modulation (FM) (see fig. 2.5). In the amplitude modulation method, a constant drive signal is applied near the natural resonance of the cantilever and changes in the amplitude resulting from the tip–sample interaction are recorded or used for distance control. In frequency modulation, the change in resonance frequency of the cantilever + tip–sample interaction system is monitored and this signal is recorded or similarly used for distance control. Both methods have respective advantages and challenges under different circumstances. The following sections discuss some of these considerations and situations under which each might be advantageous.

2.2.2 Amplitude Modulation AFM

The AM-AFM mode can, in principle, be used in either the attractive part or the repulsive part of the tip–sample interaction. However, due to instabilities caused by the multi-valued amplitude vs. distance dependance, imaging at large sample separations, ie. in the attractive mode, can be difficult [83]. As such, it has been most successfully applied in the repulsive regime, even producing atomic resolution [89], and is often referred to as "tapping"[1] or "intermittent contact" mode due to the fact that the tip comes into repulsive contact with the sample at the lower turning point of the oscillation. In this mode, the drive signal, both amplitude and frequency, is held constant and changes in amplitude of the cantilever oscillation at

[1] "Tapping mode" is a term trademarked by Vecco Instruments

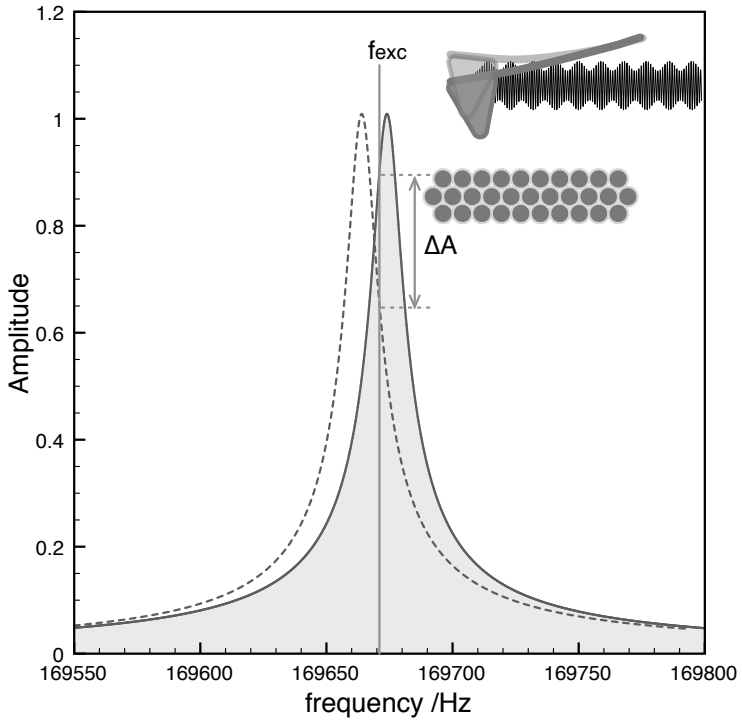

Figure 2.6: AM-AFM: due to a shift in the resonant frequency of the tip–sample system, the cantilever is excited further off resonance resulting in a reduced oscillation amplitude. Non-conservative tip–sample forces may also result in a reduction of amplitude. The changes in amplitude of the oscillating cantilever are used to detect the topography of the sample.

the drive frequency due to tip–sample interactions are measured. These changes in amplitude arise from two sources: the shift in the resonance of the cantilever due to tip–sample interactions which causes the excitation to be off resonance, and dissipative mechanisms in the sample, ie. non-conservative tip–sample interactions [89]. The former case is shown in fig. 2.6, though usually both mechanisms would be present.

The imaging forces, as well as the dissipative non-conservative forces, in AM-AFM can be determined quantitatively by considering both the amplitude change as well as the phase shift between the cantilever oscillation and the drive signal [90]. However, since both the amplitude and phase need to be considered the distinction between the conservative forces and non-conservative forces is not intuitive during the imaging process and must be determined by post-processing.

A significant issue with AM-AFM is that the amplitude signal does not instantaneously respond to changes. The "settling time" of the cantilever oscillation is dependant on the quality factor (Q-factor) of the cantilever as $\tau_{AM} \approx 2Q/f_0$ [79]. However, the signal-to-noise of the amplitude signal increases with increasing Q-

factor improving sensitivity. This trade-off is the principle reason for applying the frequency modulation technique [91] discussed in the following section.

Despite the challenges in using AM-AFM, it has been successfully applied to many systems, and is commonly used in air and even liquid environments producing excellent resolution on scales of 10's of nanometers and covering areas up to $100\mu m$ with small lateral forces. By recording phase information materials contrast can be obtained in many cases, for example to distinguish between regions of differing visco-elastic properties [92]. Additionally, as AM-AFM can be readily applied in the repulsive mode, the effects of long range forces can be mostly eliminated providing improved resolution in cases where long range forces overwhelm contact mode or FM-AFM techniques. As a result of the wide range of environments and samples which can be studied with this technique, AM-AFM has made a considerable impact on a wide range of fields from biology to materials engineering[2].

Q-control for reducing the settling time in high-Q environments

As the use of AM-AFM may be advantageous in some situations where a high-Q environment is required for other reasons (eg: ultra-high vacuum for clean surfaces, or low temperatures to investigate small energy scales) a method has been devised to artificially reduce the natural Q of the cantilever. The concept is relatively simple, and is easily seen from eqn. 2.1: the addition of a driving signal proportional to the *velocity* of the cantilever has the effect of an apparent damping of the cantilever response (see appendix C for derivation).

In practice this can be implemented by using the derivative of the cantilever deflection signal, or by using the drive signal phase shifted by $\pi/2$, multiplying either of these by a variable gain, and adding this "Q-control" signal to the drive signal used to excite the cantilever. The variable gain allows control over how much damping is added. The latter of these two methods was employed by making use of the voltage controlled oscillator (VCO) and phase-shifter present in the standard phase-locked loop used for nc-AFM imaging (see fig. 2.7)[3].

[2] AFM has even impacted popular culture! An AFM was featured on the television show CSI:Miami for materials characterization in forensics.

[3] Method using PLL and sensor controller devised by Yoichi Miyahara.

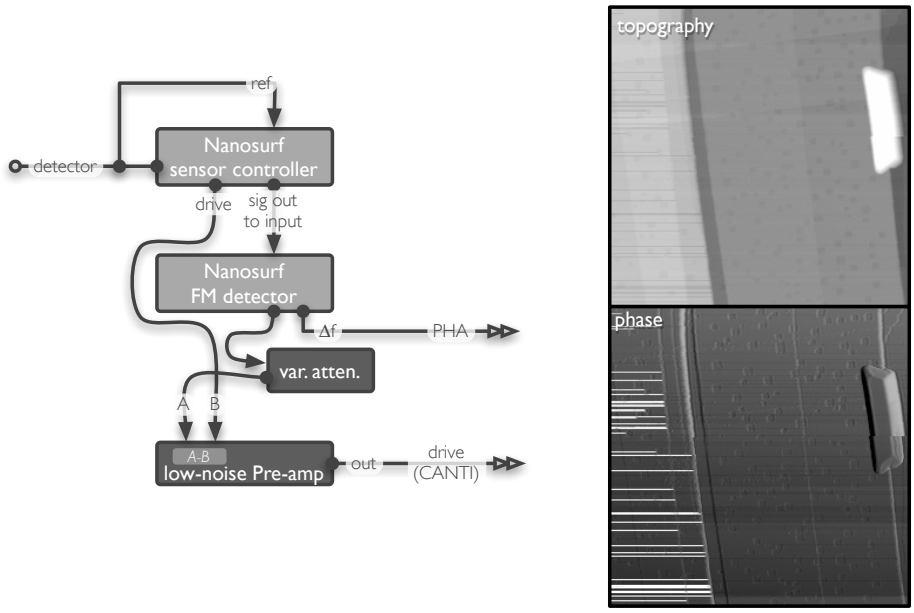

Figure 2.7: Configuration for tapping mode with Q-controll using Nanosurf EasyPLL+, with UHV tapping mode images acquired with Q∼1000, A≃7nm, and $A_{s.p.} = 0.85A_0$.

This method might be advantageous where long range forces dominate the attractive regime, or where high aspect ratio features or other issues cause instability in the self-excitation oscillation used for nc-AFM imaging, as the constant drive signal used for AM-AFM ensures that the oscillation is not lost during the imaging process.

2.2.3 Frequency Modulation or "non-contact" AFM

While the FM-AFM method was devised primarily to increase the response time of the imaging signal while maintaining high sensitivity as $\tau_{FM} \approx 1/f_0$ for the frequency is independent of Q [91], this method also provides other advantages over AM-AFM. Firstly, as the frequency shift is measured directly and the amplitude of the cantilever oscillation can be maintained constant by an additional feedback loop, the effects of conservative and non-conservative tip–sample interactions can be separated [93], which makes for a more intuitive measurement process. Also, as stable feedback is achievable in the attractive regime, so long as the spring constant of the cantilever exceeds the force gradient to avoid the so-called "snap-to-contact"

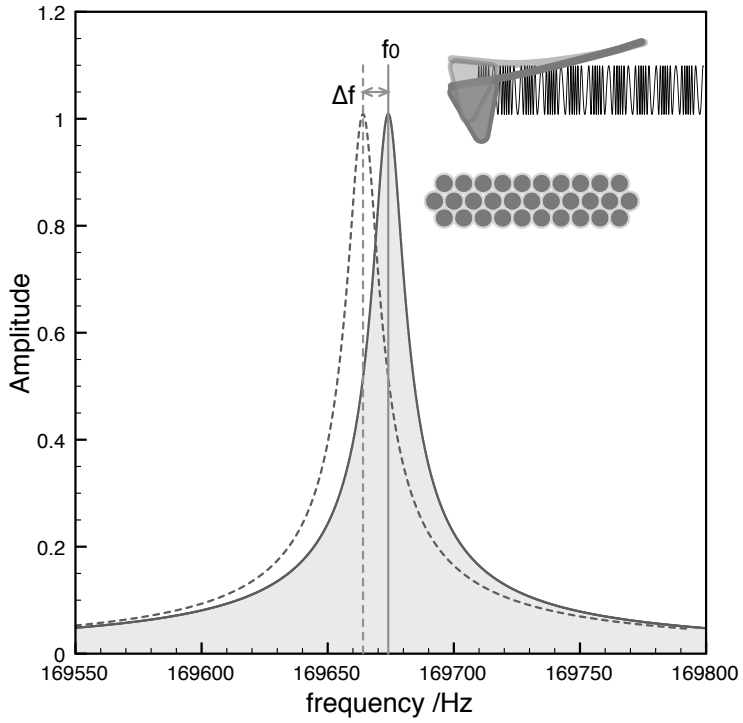

Figure 2.8: FM-AFM: by maintaining a constant $\pi/2$ phase shift between the cantilever oscillation and the excitation signal, the resonance frequency of the cantilever under the external force provided by the tip–sample interaction can be tracked.

instability, relatively reliable atomic scale imaging has now been possible for over a decade [40, 39].

The FM-AFM mode, typically referred to as nc-AFM due to its use in the attractive regime where wear and deformation of tip and sample is limited, operates by tracking the change in resonant frequency of the cantilever due to the tip–sample interaction. This is achieved by maintaining a constant phase shift of $\pi/2$ between the excitation and output oscillation such that the cantilever excitation remains on resonance, even in the presence of an external force, ie. $f_{drive} = f_0 + \Delta f_{interaction}$. This is achieved by the use of a "phase-locked loop" (PLL) which maintains a $\pi/2$ phase shift between the drive and measured oscillation thus tracking the resonance condition and providing a measure of the frequency shift. Typically a self-oscillation mode is used, whereby the measured oscillation signal is used to excite the cantilever, although the output oscillation from the PLL circuit can also be used to drive the cantilever in a so-called "tracking" mode. The details of the implementation of a PLL for nc-AFM imaging are described later in section 2.3.3.

If the tip experiences a linearly dependant force throughout the oscillation cycle, as is approximately the case for very small amplitudes or slowly varying forces, the frequency shift is simply related to the force gradient, or k_{ts} the effective spring constant of the interaction [79]:

$$\Delta f = -\frac{f_0}{2c_N}\frac{\partial F}{\partial z} = -\frac{f_0}{2c_N}k_{ts} \tag{2.12}$$

However, as larger amplitudes are commonly used to prevent snap-to-contact instabilities, the relation between force and frequency shift is somewhat more complicated [79]:

$$\Delta f = -\frac{f_0}{c_N A^2} < F_{ts}q(t) >= \frac{f_0}{2c_N}\int_{-A}^{A} k_{ts}(z-q)\frac{\sqrt{A^2-q^2}}{\pi A^2/2}dq \tag{2.13}$$

where $q(t)$ is the deflection of the cantilever. While this relationship is somewhat difficult to apply, it can be considered as a weighted average of the force over the oscillation cycle. This is a useful definition for understanding the mechanics of nc-AFM imaging, especially when determining optimal imaging parameters when the range of the interaction expected to give rise to contrast is known. In principle, for greatest sensitivity to a particular interaction, the oscillation amplitude should be selected to be on the order of the range of the interaction. Quantitative conversion from frequency shift to force in the large amplitude limit requires some mathematical machinery and is the topic of several papers presenting both numerical methods [94, 95] and an analytic framework for arbitrary amplitudes [96, 97] in which the rigourous demarcation between conservative and non-conservative forces is also addressed.

While the frequency shift Δf is the measured observable quantity in nc-AFM which is typically used for z-feedback, the other parameters of the oscillating cantilever also play a role. To compare results obtained under differing parameter sets, a normalized frequency shift is sometimes used [79]:

$$\Gamma = \frac{c_N A^{3/2}}{f_0}\Delta f \tag{2.14}$$

where c_N, A and f_0 are the spring constant of the cantilever, the amplitude of

oscillation and the free resonant frequency of the cantilever, respectively.

Dissipation imaging in nc-AFM

It is common in nc-AFM imaging to use an additional control loop to maintain a constant amplitude of oscillation by modifying the drive signal. In this case, the change in drive signal required to maintain the constant amplitude of the cantilever is often interpreted as being related to the energy dissipated per cycle of the cantilever oscillation [79]:

$$E_{ts} = E_0 \left(\frac{A_{exc}}{A_{exc,0}} - \frac{f}{f_0} \right) \tag{2.15}$$

where E_{ts} is the dissipated energy, A_{exc} and $A_{exc,0}$ is the amplitude of the drive signal required to maintain the amplitude setpoint during imaging and far from the sample, respectively. E_0 is the intrinsic damping of the cantilever and is given by [79]:

$$E_0 = \frac{\pi c_N A^2}{Q} \tag{2.16}$$

where c_N and Q are, as before, the normal spring constant of the cantilever and the intrinsic quality factor of the oscillator, and A is the amplitude which is maintained constant. It should be noted, that this measurement approach may not be entirely rigourous, and for a full discussion of issues regarding quantitative determination of conservative and non-conservative forces and their distance dependence see [97]. Regardless, the required increase in drive amplitude is often reported as the "dissipation" and is still interpreted as discussed here.

While dissipation imaging holds the potential to reveal a wealth of information regarding visco-elastic properties and adhesion down to the formation and breaking of a single bond, it has been wrought with issues related to sensitivity to tip structure and composition [79, 76, 98].

THE FOLLOWING SECTION IS BASED ON TEXT FROM:

S.A. Burke and P. Grütter. Comment on: Temperature dependence of the energy dissipation in dynamic force microscopy, *Nanotechnology*, **19** 398001, 2008.

Recently, T. Roll and co-authors reported measurements of the temperature dependance of dissipation in dynamic force microscopy, or noncontact atomic force microscopy (nc-AFM), on a sample system of molecular crystallites PTCDA on KBr [99]. They find the anticipated behaviour for the adhesion hysteresis mechanism on the molecular islands, ie. decreasing dissipation with increasing temperature. However, they find the opposite trend for dissipation on KBr indicating a possible stochastic friction force mechanism, though this gives a very different order of magnitude for the expected dissipation. While we do not dispute the importance of results such as these in understanding the mechanisms for dissipation in nc-AFM, we urge caution in interpreting dissipation results which we argue are highly dependant on tip structure.

We have performed similar measurements on the same system, PTCDA on KBr. These measurements were made in the nc-AFM imaging mode using a JEOL JSPM-4500a with a variable temperature stage in combination with a nanoSurf easyPLL+ for frequency detection and constant amplitude control. The dissipation signal is measured by the increase in drive amplitude required to maintain a constant amplitude of oscillation of the cantilever. To enhance the often weak dissipation output, a Stanford Research Systems low-noise pre-amplifier was used to amplify the dissipation signal before input to the JEOL controller. Measurements were made with Nanosensors PPP-NCLR cantilevers which have typical resonance frequencies of 170kHz, spring constants of 38 ± 6N/m (for the wafer used) and measured Q-factors of 10,000-15,000 in our system. Measurements were made at room temperature and $\sim$100K using the JEOL cryostat and cold finger with liquid nitrogen. Samples were prepared in UHV by depositing PTCDA molecules on a nanotemplated KBr substrate as described elsewhere [54].

In our measurements of dissipation we have found that contrast is very highly dependant upon the tip, and that results ranging from negative contrast to positive contrast or no contrast at all can be easily obtained by minor tip changes or with different cantilevers. For example, figure 2.9 shows a nc-AFM image with topography and dissipation simultaneously acquired. A tip change occurs several lines from the top of the scan which has only a minor effect on topography, but shows a sudden increase in dissipation and a negative contrast between the KBr substrate (on the left) and the PTCDA island (on the right). This change is tempo-

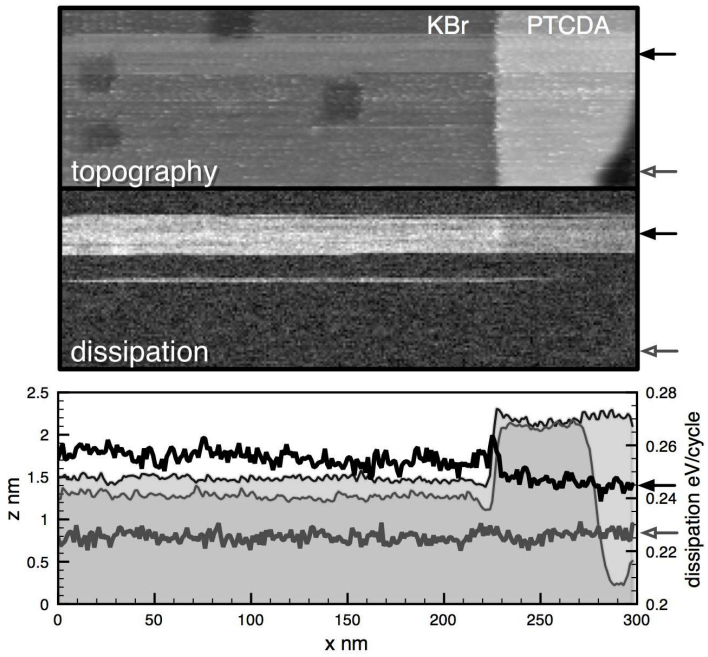

Figure 2.9: Measurement of topography (top) and dissipation (middle) exhibiting a tip change with minimal effect in topographic imaging, but with a dramatic effect in the dissipation channel. The two cross-sections (8 lines averaged) are shown by the open and closed arrows showing the overall shift in dissipation between the two different regions as well as the appearance of contrast (closed arrows). Imaging parameters: Γ=-0.86fNm$^{1/2}$,Δf=-7Hz, f_0=169,653Hz, A=6.7nm, T=100K.

rary and the image returns to showing no dissipation contrast for most of the rest of the scan.

Similarly, for high resolution imaging, where larger frequency shift is used, we find tip changes to be frequent and have a significant impact on the contrast appearance in both topography and dissipation. Figure 2.10, shows five different segments of the same image each following a different tip change on a molecular island. The appearance of the molecules changes dramatically depending on the tip, and molecular contrast in dissipation only appears in two of the segments. The effect of the state of the tip on atomic scale dissipation are well known [79] and interpretation of such measurements requires careful consideration of the tip structure [76].

We have likewise attempted to measure the temperature dependance of dissipation contrast. However, due to variability of the tip we were unable to obtain consistent results. For example, the authors report a somewhat small negative contrast over the PTCDA molecules at 300K and a considerably larger positive contrast over the molecules at 100K. However, we have observed the opposite trend in contrast using the same tip to measure at both room temperature and

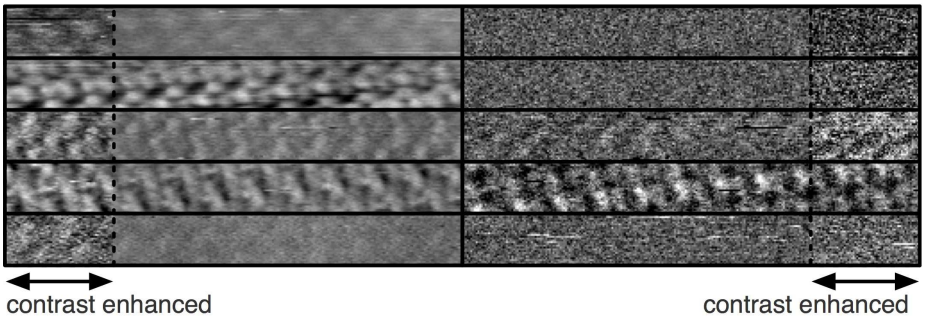

Figure 2.10: Segments of the same image showing variety of molecular contrast in topography (left) and dissipation (right) possible by minor tip changes during imaging. The z-scale (topography range: 115pm, dissipation range: 0.1eV/cycle) is the same for all images in the central region, and enhanced to better show molecular contrast for each section on the edges. Imaging parameters: Γ=-1.7– -2.9fNm$^{1/2}$,Δf=-9– -16Hz, f_0=170494Hz, A=8.8nm, T=300K.

$\sim$100K (see fig. 2.11). As the imaging conditions used in our experiments differ significantly from those used by Roll et al, we do not attempt to quantitatively compare values for the dissipation. At room temperature we observe a significant positive contrast, however, after cooling to $\sim$100K we do not see any dissipation contrast between the KBr substrate and a PTCDA island within a noise level of 0.006 eV/cycle. We were also able to obtain negative contrast for similar values of the normalized frequency shift at room temperature with a different cantilever, and often observed no contrast at all. Similarly, in some instances clear dissipation contrast (both positive and negative) was obtained at low temperature.

It should be noted that the different imaging conditions used by Roll et al., ie. larger amplitude and higher fundamental frequency, may result in stronger dissipation contrast due to a closer matching of timescales between the tip motion and dissipative processes in the sample. However, the influence of such imaging parameters on the stability of dissipation contrast, for example against tip changes, is not understood and should be investigated systematically.

The variability of the results obtained for dissipation on molecular islands due to both differing macroscopic and microscopic tip shapes and compositions, points to an extreme difficulty in interpreting dissipation results. Roll *et al.* take care to indicate that the measurements were performed with the same cantilever,

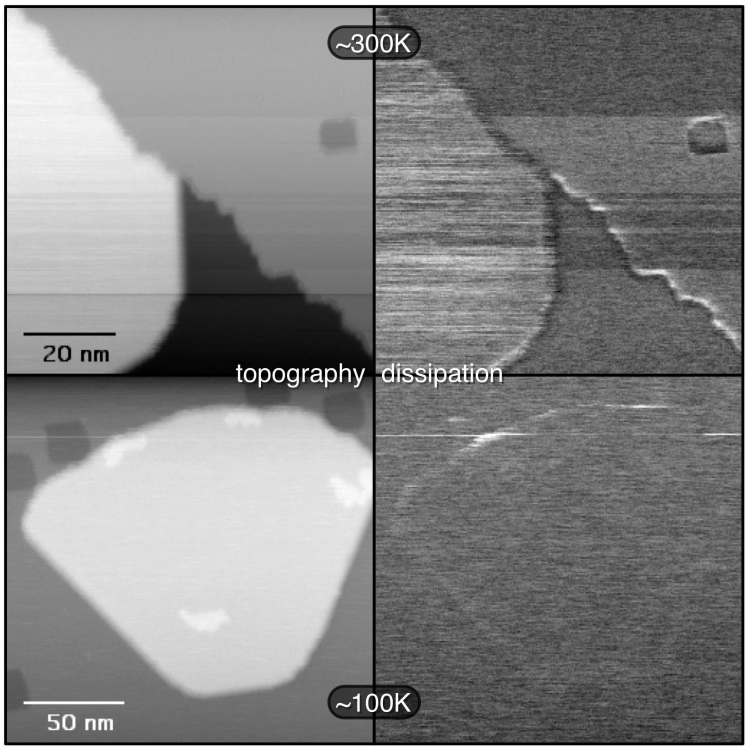

Figure 2.11: Room temperature and low temperature measurements of dissipation for PTCDA crystallites on KBr showing strong positive contrast at room temperature and no discernible contrast at 100K. Imaging parameters (top): Γ=-1.4fNm$^{1/2}$,Δf=-9Hz, f_0=171718Hz, A=8.1nm, T=300K. Imaging parameters (bottom): Γ=-1.9fNm$^{1/2}$,Δf=-12Hz, f_0=171754Hz, A=8.1nm, T=100K.

which we agree is necessary for comparison within a data set for this reason, however it cannot be assured that the microscopic nature of the tip remains unchanged. Tip changes which are subtle in topography can have a dramatic influence on dissipation contrast, and indeed, a recent paper shows a tip change which reversibly occurs across a single KBr step with little influence on topography, but showing dramatic changes in dissipation [98]. Moreover, acknowledging that the dissipation contrast is highly tip dependent indicates that to determine overall dissipation mechanisms and for comparison to theoretical calculations these experiments must be reproduced with multiple tips showing the same overall trends.

Kelvin Probe Force Microscopy

THE FOLLOWING SECTION IS BASED ON TEXT FROM:

Supporting information for: S.A. Burke, W. Ji, J.M. Mativetsky, J.M. Topple, S. Fostner, H.-J. Gao, H. Guo and P. Grütter. Strain Induced Dewetting of a Molecular System: Bimodal Growth of PTCDA on NaCl. *Phys. Rev. Lett.* **100**:186104, 2008.

Noncontact Atomic Force Microscopy (nc-AFM) is sensitive to tip-sample forces which includes those from: chemical interactions, van der Waals interactions and electrostatic interactions. As electrostatic interactions often play a significant role, it is common in nc-AFM to minimize electrostatic forces by applying a voltage corresponding to the contact potential difference (CPD). However, for heterogeneous samples, the CPD will most commonly have a spatial variation corresponding to the composition of the material under the tip at a given point. By applying a constant voltage only, there can be variation in the contrast arising from the electrostatic interaction.

Kelvin Probe Force Microscopy (KPFM) utilizes an oscillating bias voltage between tip and sample which is used through a lock-in measurement of the resulting frequency shift to minimize the electrostatic forces over all parts of the sample (see fig. 2.12 for a schematic) [100]. The result is a topographic image that is, ideally, corrected for electrostatic forces, and a KPFM image corresponding to the CPD variations of the sample. It was suggested by Sadewasser et al [101] that this method could be used to obtain "true height measurements" in nc-AFM corresponding to only the van der Waals and chemical interaction forces. In the absence of a large CPD difference, the height measurement is relatively unaffected. However, as demonstrated by imaging at different voltages for PTCDA monolayer islands on NaCl, the apparent height can be influenced significantly, even appearing as a depression rather than an island, depending on the applied bias (see fig. 2.13).

While it is difficult to interpret the CPD measurement on a thick insulating substrate, the technique can still be used to minimize the electrostatic force over the substrate. Figure 2.14 shows the topography (a) and CPD map (b) resulting from a KPFM measurement of monolayer islands of PTCDA on NaCl. Heights

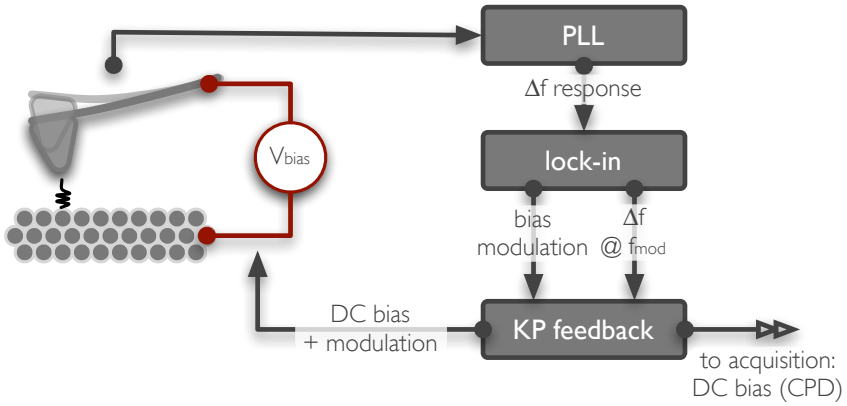

Figure 2.12: KPFM feedback on electrostatic force: A modulated bias is applied between tip and sample producing a frequency shift response at the modulation frequency. This is detected by lock-in detection and used as a feedback signal to be minimized by adjusting the offset bias. This offset bias is then recorded as the CPD.

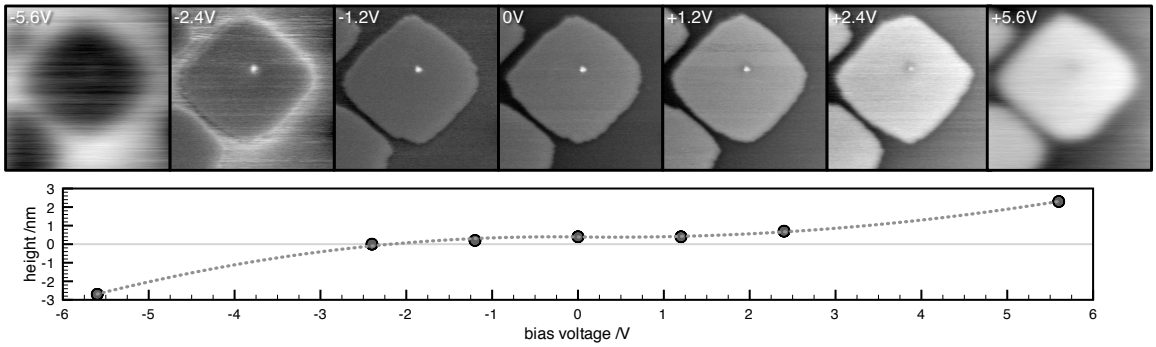

Figure 2.13: Nc-AFM topographic images of PTCDA on NaCl at different bias voltages (top), below is a plot of apparent island height as a function of the bias voltage with spline fit (dashed line) to indicate trend.

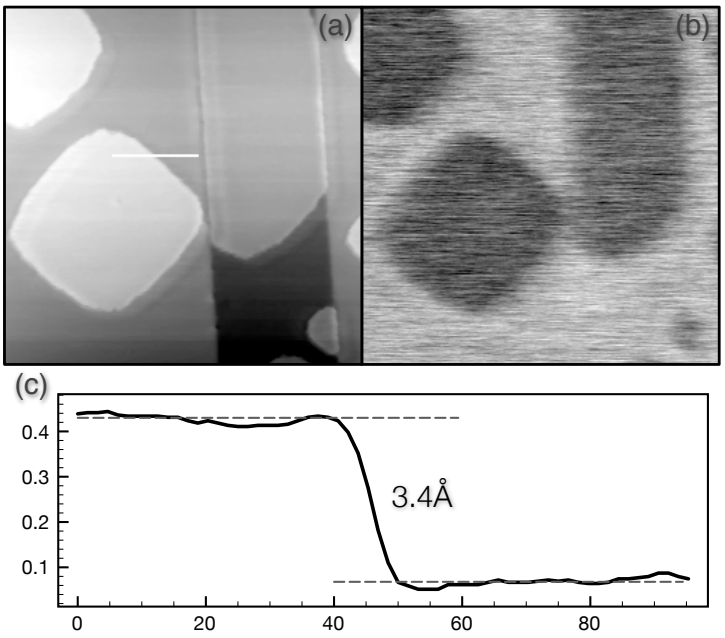

Figure 2.14: KPFM measurement of PTCDA on NaCl with topography (a) and CPD map (b). The height of the island is shown from a line section (c) taken from (a) indicated by white line. Imaging parameters: Δf=-4.8Hz, size: 400nmx400nm.

of these monolayer islands were found to be 3.4$\pm$0.2Å using this method which closely corresponds to the interlayer spacing of PTCDA of 3.3Å [102] and compares well with calculated values (see section 4.2.1). The corresponding contact potential difference for this measurement was found to be $\sim$0.7 V. Typical parameters for KPFM measurements of this system were a cantilever resonance of 160-170kHz, voltage oscillation of 1-2 V rms at a frequency of 800-1000Hz, lock-in amplifier reading with time constant of 1 or 3ms, and sensitivity of 20-50mV. Images were acquired at 6.667ms/point to generate 256$\times$256 pixel images.

In principle, the use of KPFM feedback to minimize electrostatic forces could also be used to obtain improved resolution across the boundary of two different materials, as in the case of an island of deposited material. In practice, other factors including the additional time required to make the measurement in the current KPFM configuration, have limited our ability to obtain atomic-scale resolution while minimizing the electrostatic contribution using KPFM feedback.

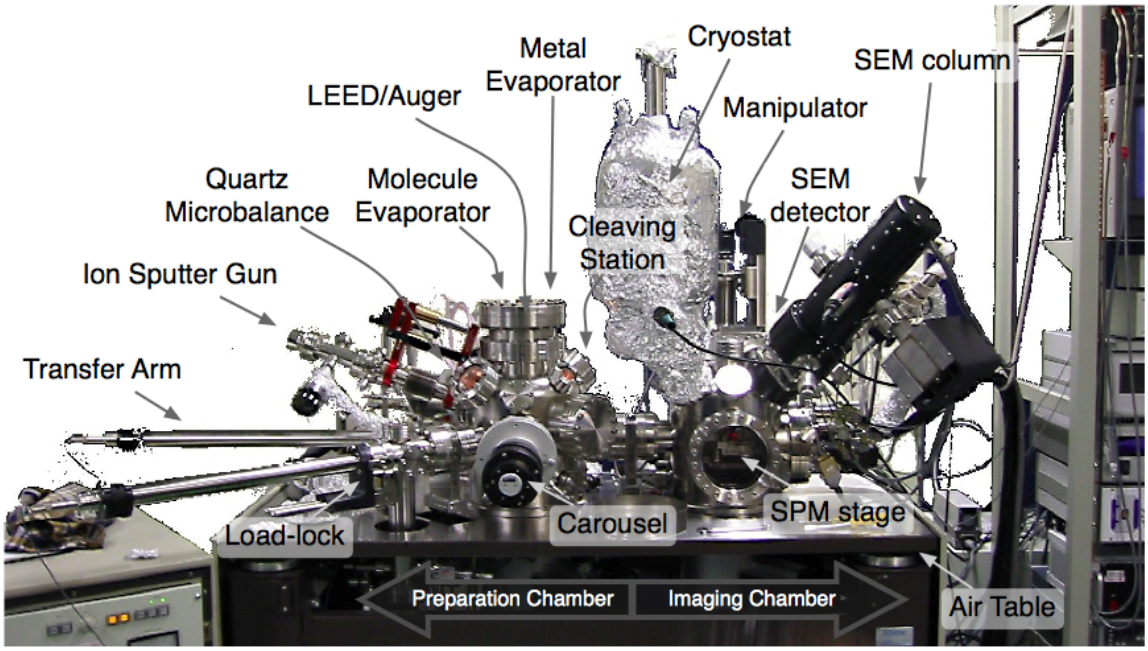

Figure 2.15: Labelled photo of UHV system. The imaging chamber is on the right containing the STM/AFM stage and SEM. The sample preparation chamber and load lock are on the left.

2.3 Description of Apparatus

All imaging and sample preparation was performed in the commercially available JEOL JSPM 4500a ultra-high vacuum (UHV) STM/AFM. The UHV system consists of two chambers, preparation and imaging, which are pumped by combined secondary-ion pumps and titanium sublimation pumps and typically base pressures of $1 - 3 \times 10^{-8}$Pa are achieved after bake-out of the chambers. The system also has a high-vacuum load-lock for exchanging samples and tips without breaking vacuum in the UHV chambers. The load-lock is pumped by a standard turbo-molecular pump (Pfieffer TMU 261), backed by a mechanical roughing pump (ULVAC G-100DC), and achieves sufficient pressure ($\sim 5 \times 10^{-7}$Pa) to exchange specimen after $\sim$30 minutes. The entire UHV system is mounted on a vibration damping air table and the turbo molecular pump is shut off during measurements to reduce vibrations for SPM imaging.

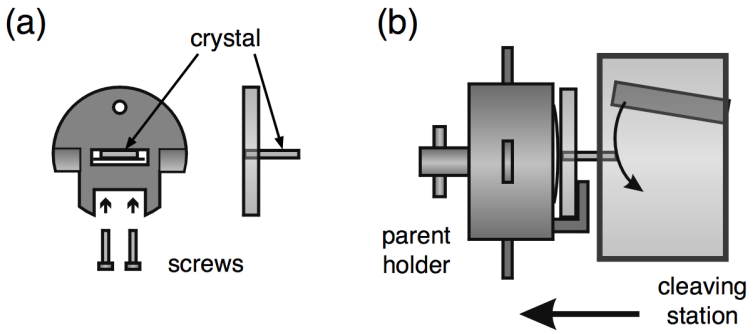

Figure 2.16: Cleaving holder, parent holder and cleaving station schematics. The crystal is held in the cleaving holder by two screws which press a stainless steel plate against the bottom of the crystal (a). The crystal must protrude at least 4mm from the face of the holder, and usually a line is scribed along the top edge close to the holder face to facilitate cleaving along this plane. The parent holder (b) holds the cleaving holder with solid L-brackets from the bottom and a spring pushes from the back to maintain tension. The parent holder docks with the cleaving station so that the carousel is not free to move when force is applied from the cleaving arm. The cleaving arm swings down with a gradual motion applying pressure to the protruding crystal until it breaks.

2.3.1 Preparation Chamber

The sample preparation chamber provides the ability to transfer samples from the load lock to a carousel with 4 positions for tip and sample carriers. Two transfer arms intersect at the carousel to allow transfer between the load lock, preparation chamber and main chamber. The carousel is positionable to allow tips and samples to be accessed by the various instruments in the preparation chamber for preparation and characterization. The carousel also provides electrical contact to 3 of the 4 positions.

The instruments used for sample preparation are briefly described as follows:

Crystal cleaving station The crystal cleaving station consists of three pieces, a specialized sample holder, sample parent holder, and a movable arm which can be advanced and docked with the carousel. Once docked, a block of

stainless steel is lowered against the protruding crystal until the crystal snaps off revealing a clean crystal plane (see fig. 2.16).

Crystal heater A tungsten heating filament was built into a parent holder [103], such that the sample holder sits in front of the filament and is heated radiatively and through contact with the surroundings of the holder. This allows heating of cleaved insulating samples to redistribute charged defects created in the cleaving process. The heating filament was calibrated using a low-temperature (150-450°C) optical pyrometer (IRC IR-CA P2CS) focused on a metal coated sample [104]. The correspondence between current and temperature at the sample surface from this measurement is used to determine the approximate temperature for heating samples.

Molecule Evaporator A three-source thermal evaporator with temperature feedback, commercially available from Kentax, was used to deposit molecules on surfaces. Molecules are evaporated from quartz crucibles surrounded by resistively heated coils. Water cooling prevents adjacent crucibles from being heated, and a specially designed shutter allows for all possible combinations of sources to be opened for co-evaporation if multiple power supplies are used. For the experiments performed only one molecular material was evaporated at a given time, and thus the shutter was positioned so that only the desired source was open to further reduce the possibility of contamination from adjacent sources. The evaporator was mounted on a set of retractable bellows and can be isolated from the preparation chamber by a valve and connected to a separate pumping line. This allows the replacement of the molecular sources without breaking vacuum in the preparation chamber. Parameters for evaporation and outgassing of organic sources are listed in Appendix B.

e-beam Metal Evaporator A four-source electron-beam (e-beam) evaporator is used to deposit metals and as a source of charge to create nanoscale pits in alkali halides by electron stimulated desorption [105]. Each of the four pockets has a tungsten filament heated to generate electrons which are emitted and accelerated by 2kV to bombard the target material either in the form of a solid rod of evaporant, or a crucible filled with the evaporant. Crucibles are used

for materials that melt near the desired evaporation temperature, and sometimes are needed in order to obtain larger rates to prevent changes in the target geometry at higher temperatures. Materials used (but not in this thesis) are: tantalum (rod), gold (crucible, or rod at low rates), platinum (rod, at low rates), and iron (rod). The evaporator is fitted with an ion retarding grid, however a small amount of charge is still emitted, and this very low current source can be used for the controlled formation of nanoscale pits in alkali halides.

Quartz Microbalance An Inficon bakeable sensor was used to monitor deposition rates and coverages. The sensor was mounted on a set of retractable bellows to allow for positioning at the sample location to measure the rate, and then retraction for deposition of the desired material. For densities used for different organic materials and typical rates achieved, see Appendix B.

The prepration chamber also has available a LEED/Auger system (Specs) for surface analysis, and a scannable ion sputtering gun (Specs) for surface preparation which were not used in the course of this work.

Removable elements

Sample holders and tip holders are exchanged using special carriers or "parent holders" which mate with the two transfer arms and carousel. The parent holder for STM tips or AFM cantilevers has two positions allowing for introduction and storage of two tips at a time. There are two types of parent holders for sample holders, one for cleaving (see fig. 2.16) which has a solid stainless steel base to withstand the force required for crystal cleaving, and a another which has electrically isolated spring clips to hold the sample which connect to the side ears of the parent holder. This allows electrical measurements or electrical contact to the parent holder when placed in any of the 3 carousel positions with electrical contacts, for example to provide a current for the filament of the aforementioned heating holder.

The cleaving sample holder, as shown in fig. 2.16, is a solid stainless steel piece with a rectangular cut-out in the middle for the crystal. The crystal is held solidly in place by means of a stainless steel plate which is pushed against the

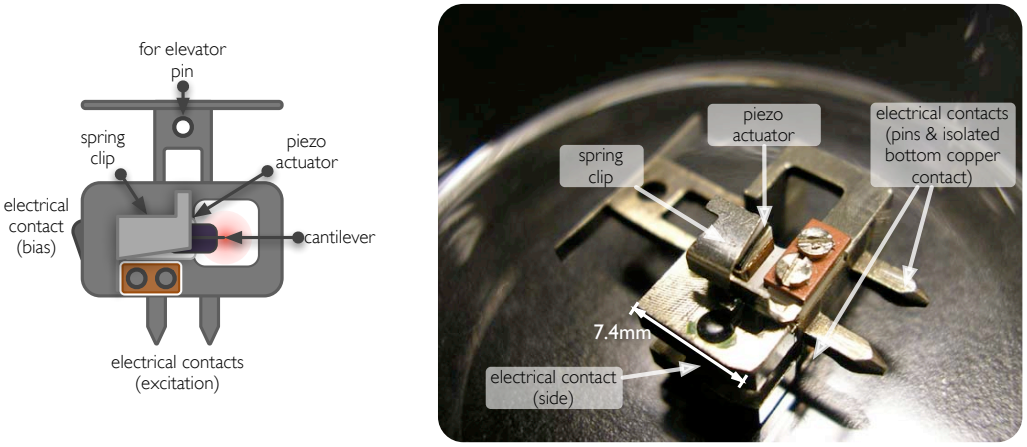

Figure 2.17: Schematic (left) and labelled photograph (right) of JEOL cantilever holder.

crystal by two screws. The plate helps to distribute the pressure of the screws more evenly and provides an edge to help initiate cleaving. Thus the shape and alignment of this plate is somewhat important for obtaining flat cleaved samples. This holder was used for all alkali halide substrates.

A second style of sample holder is used for flat samples, for example mica. Here two clips fixed with screws at the top and bottom of the sample area hold the sample in place on an insulating back piece. Samples can be mounted either alone or against a copper beryllium plate if greater mechanical stability or a continuous back electrode is needed.

The cantilever holder (see fig. 2.17) plays a crucial role in dynamic AFM imaging as the cantilever chip is held against a small piezo actuator which is used to excite the cantilever. The cantilever is held in place with a flat stainless steel spring which is adjusted[4] to have the correct tension to ensure solid clamping of the cantilever and electrical contact for bias application or grounding of the tip, but if the spring force is too strong the piezo cannot sufficiently excite the cantilever oscillation. The spring clip is also connected to a rotating side contact which provides the tip bias or ground connection. The holder has a cut out section for optical access to the cantilever for the optical beam deflection scheme used.

[4]The spring clip holding the cantilever in place must be readjusted periodically to ensure good mechanical and electrical contact.

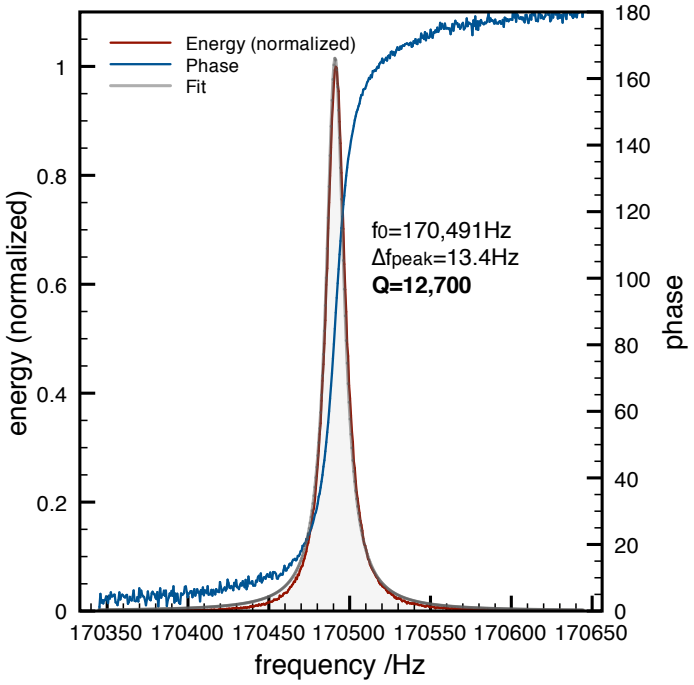

Figure 2.18: Typical resonance curve of Nanosensors PPP-NCLR in JEOL JSPM with NanoSurf EasyPLL+.

The cantilevers used are commercially available doped silicon cantilevers with a back reflective coating (Point Probe Plus NCLR, Nanosensors). Typical resonance frequencies are 160-180kHz, with spring constants of 40-50N/m. Measured Q-factors of these coated cantilevers are typically 7 000-10 000 *in situ* at room temperature. Uncoated cantilevers give higher Q-factors of around 15 000. An example of a typical resonance curve is given in figure 2.18. Cantilevers are baked at $\sim$150° C for 7 hours in the preparation chamber after introduction to the vacuum system to remove contamination. No other preparation, for example sputtering, is used and the tips are expected to have a native oxide layer intact[5]. Forces for typical imaging parameters used in this thesis are estimated to be less than 100pN.

[5]The native oxide may aid the imaging of weakly bound species by reducing the interaction strength between the tip and adsorbate. Should the tip–adsorbate interaction strength exceed the adsorbate binding strength there would be some likelihood of transferring adsorbates from the surface to the tip during imaging.

2.3.2 Imaging Chamber

The imaging chamber consists of the STM/AFM stage (see fig. 2.19), a cryostat which is connected to the stage by means of a cold finger, and an electron column and secondary electron detector for performing SEM measurements *in situ*. A two dimensional linear translator, referred to as the "elevator" or "sample chucking unit", allows exchange of samples from parent holders on the preparation to main/imaging transfer arm with the tip and sample positions on the imaging stage. The sample and tip holders are designed with a small hole near the top of the holder which mates with an electromagnetically actuated and spring loaded pin. This allows for safe retrieval of tips and samples as the pin does not release unless an upward force is applied to the elevator unit.

For observation by either STM, AFM, or SEM, the sample is placed on the stage at the sample position which is fixed to the end of the piezo-electric scanner used for SPM observation. The stage is mounted on large springs to minimize vibration coupling from the exterior of the instrument, but can be rigidly locked to prevent damage during removal from the system, or for high resolution SEM observation. The field-emission electron column for SEM observation is mounted at 45° azimuthal and polar angles with respect to the sample plane which gives the perspective of looking down from the side at the tip and sample (geometry described in more detail in [106]). For STM or AFM observation, the tip is placed opposite the sample position on a manually retractable portion of the stage allowing for safe transfer of both tip and sample and SEM observation without the tip.

The stage is contacted to the cryostat by two sets of flexible silver foils which attach to a cold finger for low temperature observation. The piezo is cooled only by the outer dewar which is filled with liquid nitrogen for any low temperature observation. The sample position is contacted by the inner dewar which can be filled with liquid nitrogen or liquid helium to achieve temperatures of $\sim$100K or $\sim$30K, respectively.

The sample is held by two electrically isolated spring clips to the front face of a piezo tube scanner which allows fine positioning in x, y and z. The scanner has a maximum range of 5μm in x and y and 1.4μm in z at room temperature. The piezo scanner is used for fine positioning and the final approach only. Three motors allow coarse positioning, reproducible to within several μm, in x and y, as

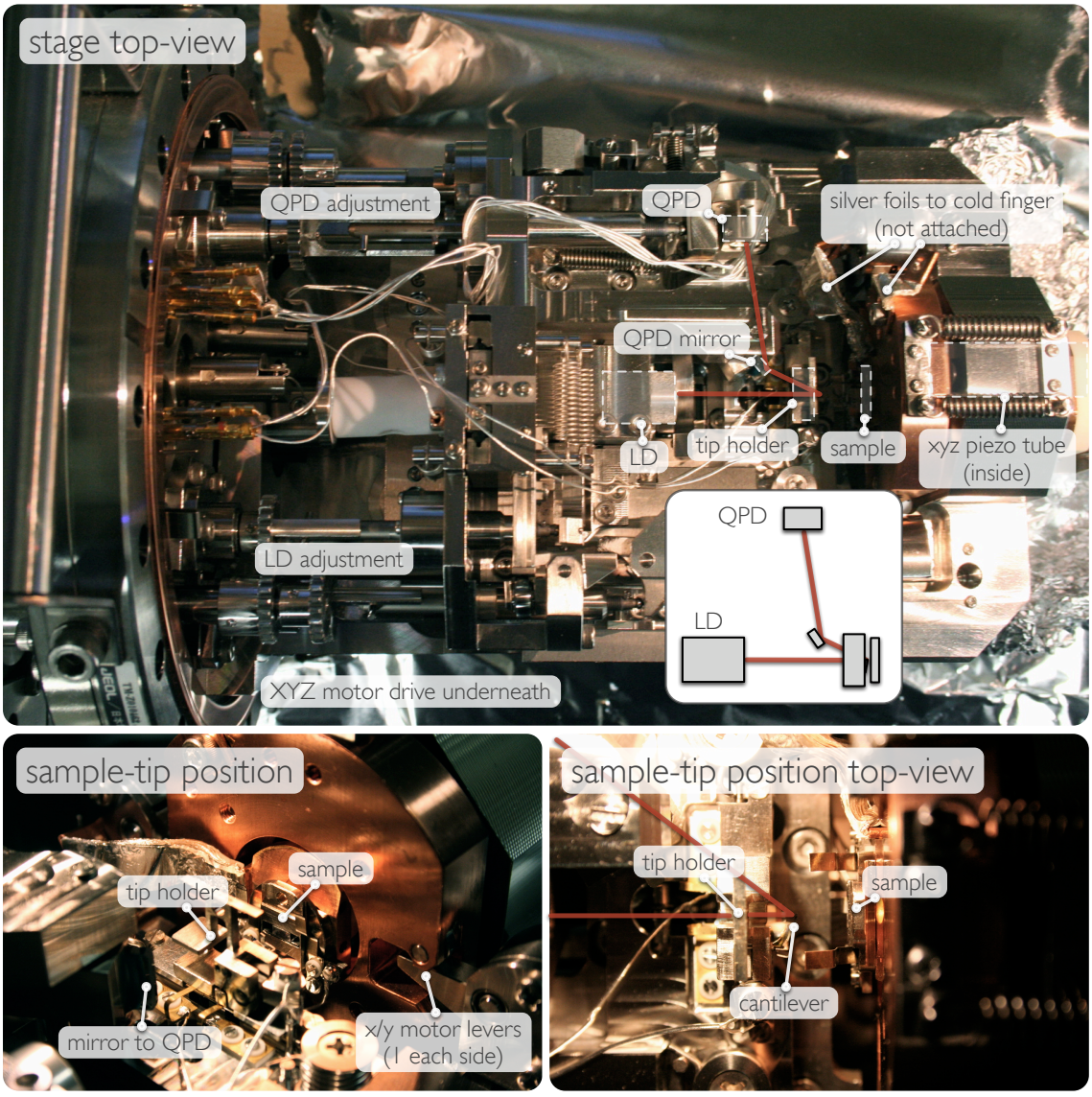

Figure 2.19: Labelled photos of JEOL JSPM 4500a stage. Top: top-view of full stage assembly with inset showing optical beam deflection geometry. Below: perspective (left) and top-view (right) of tip–sample position.

well as perform the approach to within the z-piezo range. The motors are mounted externally, and rotary feedthroughs connect to a series of gears and lever arms to provide motion of the stage (x,y) and tip (z). A solid lubricant of MoS_2 is used on the worm gears to prevent sticking[6].

For AFM observation, an optical beam deflection system is used (see fig. 2.19 and inset). A laser diode is mounted inside the UHV system on the stage and focused onto the cantilever position. The laser diode position can be adjusted via a series of gears and levers which connect to two rotary feedthroughs. The laser beam is reflected off the back surface of the cantilever onto a mirror where it is redirected into a quadrant photodiode. The photodiode and mirror are also positioned via a series of gears and levers connected to two rotary feedthroughs providing alignment of the two directions, "A-B" and "C-D" corresponding to normal and lateral deflection respectively. These "A-B" and "C-D" signals are the normalized difference signals which correspond to the displacement of the reflected laser beam on the quadrant photodiode. As mentioned above (section 2.3.1), the tip holder contains a small "shaker" piezo to excite the cantilever for dynamic modes.

2.3.3 nc-AFM imaging & acquisition

While STM, contact mode AFM, and "tapping" mode AFM with Q-control have all been applied in the system, the primary imaging mode used was nc-AFM, with optional KPFM feedback. This generally provides high resolution, and the ability to image insulating substrates. As described in section 2.2.3, the nc-AFM imaging mode relies on the detection of a change in frequency of an oscillating cantilever due to a tip–sample interaction.

The measurement of the induced change in frequency can be performed by the use of a self-oscillation mode, which guarantees constant phase by using the detector signal as the excitation signal, or a tracking oscillation mode using a phase-locked loop (PLL), which applies a feedback circuit to maintain a constant phase shift of $\pi/2$ between the cantilever oscillation and excitation signal (see fig. 2.20). In both cases, the PLL is used to measure the frequency shift, Δf. The

[6]The MoS_2 should be re-applied every few years to maintain the system, or if the motors appear to stick and slip.

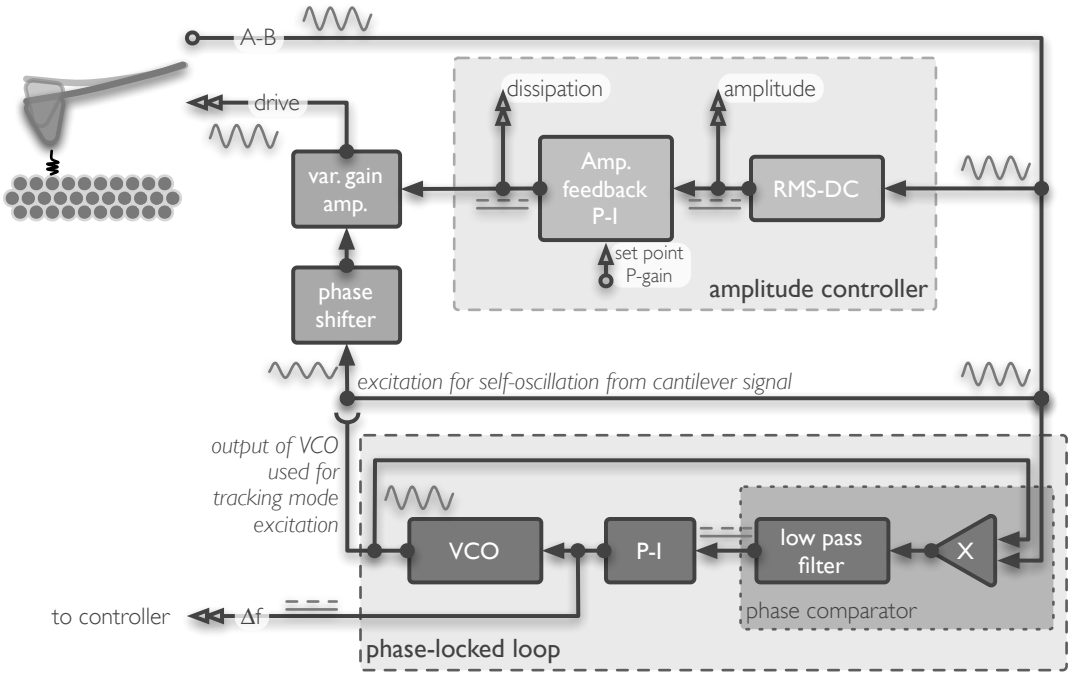

Figure 2.20: Schematic of PLL and sensor controller for nc-AFM imaging. [107]

oscillating deflection signal (A-B) is compared to a reference signal to determine the phase of the oscillation with respect to the excitation. The "phase-comparitor" multiplies the measured oscillation signal with a reference signal resulting in:

$$V_{phase} \propto [cos(\phi_{in} - \phi_{ref}) + cos(2\omega_0 t + \phi_{in} + \phi_{ref})] \tag{2.17}$$

where ϕ_{in} and ϕ_{ref} are the phases of the input (A-B) and reference signals, and the frequency of the two signals is considered to be approximately equal. The multiplier is followed by a low-pass filter to eliminate the second time dependent term, leaving only the term corresponding to the phase difference between the input and reference oscillations:

$$V_{phase} \propto cos(\phi_{in} - \phi_{ref}) \tag{2.18}$$

This phase dependent term is used to minimize the phase difference between the two signals by adjusting the frequency of the voltage controlled oscillator (VCO)

until the phase difference between the two oscillations is $\pi/2$, or V_{phase} is zero. This feedback on the phase difference constitutes the "phase locked loop" and provides the frequency shift as well as an output oscillation which can be used for excitation. In practice, in high-Q environments the self-oscillation mode is more commonly used, where the drive signal is derived from the input deflection signal, as this guarantees minimal phase error on the excitation signal and simplifies interpretation. The Δf output of the PLL is then used as the reference signal for the AFM z-control feedback for topographic imaging.

The implementation of the nc-AFM imaging mode for the JEOL JSPM 4500a used for the experiments herein makes use of an external NanoSurf EasyPLL, which has been modified to provide both proportional and integral gain for improved amplitude control[7]. The input detector signal is taken from the JEOL "AFM AMP" A-B output. The constant phase difference, center frequency, amplitude set point, and amplitude control parameters are set on the NanoSurf sensor controller, or through the NanoSurf software. The output Δf signal is input to the the JEOL SPM controller as "AFM" which provides z-feedback while scanning in x and y generating constant Δf topography. The feedback parameters (gain, and feedback filter settings) are set through the software as well as a "reference" set point. Scan size, speed, location and bias voltage are also all controlled through the JEOL WinSPM acquisition software.

Kelvin probe feedback and/or imaging can be performed with the use of an extra feedback loop provided as the JEOL SKPM controller. Here, a standard lock-in amplifier (Princeton Applied Research, 5110 Lock-in Amplifier) is used to provide a modulation bias (f_{mod}, V_{mod}), also used as the internal reference for detection, and added to a DC bias offset in the SKPM controller. This modulated output bias is applied to the tip by the spring clip which holds the cantilever chip in place. The sample is held at ground for KPFM measurements[8]. The modulation of the tip–sample bias produces a modulation of the frequency shift at f_{mod} which is detected by the lock-in amplifier. The Kelvin probe feedback attempts to null the component of Δf at f_{mod} by adjusting the DC bias offset to compensate for

[7]Modifications were made by Yoichi Miyahara.

[8]To compare KPFM results with spectroscopy results the voltage values should be inverted as in the normal imaging configuration the tip is held at ground and the bias is applied to the sample position.

varying CPD of the sample.

It should be noted that the interpretation and quantitative comparison of measured CPD values on thick dielectric substrates is somewhat complicated as the applied bias does not directly correspond to the potential difference between the sample surface and the tip apex. The measured bias and the actual sample surface–tip apex bias are related through geometrical factors. For a discussion of this matter and derivation of potential difference between the surface of a dielectric and a parallel plate across a vacuum gap, see Appendix D. Due to the complexity of the geometry for the JEOL sample holder (cleaving holder) used, this effect is not considered, and as such only a quantitative description of the directions and relative differences in CPD are discussed.

Auxiliary channels, for example the CPD or dissipation, can be recorded along with topography. These can be input to the controller as phase, labelled PHA (AUX3), or C-D (AUX2). The current configuration of the JEOL SPM controller allows only one or the other of these two channels to be recorded with topography. For weak auxiliary signals, for example dissipation, a low noise voltage pre-amplifier (Stanford Research Systems SR560) was often used to offset, amplify and filter the signal before digitization in the controller[9].

The JEOL software displays data line by line during acquisition and images are saved in a 16-bit TIFF format. All imaging parameters from the JEOL software[10] are stored in the header information, some of which are displayed in the information display window when images are opened in the WinSPM analysis package, but all of which can be accessed with a hexidecimal editor if necessary.

[9] In this case, the filter settings, offset used and gain had to be recorded in order to extract the original quantities.

[10] Notably, the frequency shift given by the NanoSurf PLL is *not* recorded by the JEOL software, and must be recorded separately.

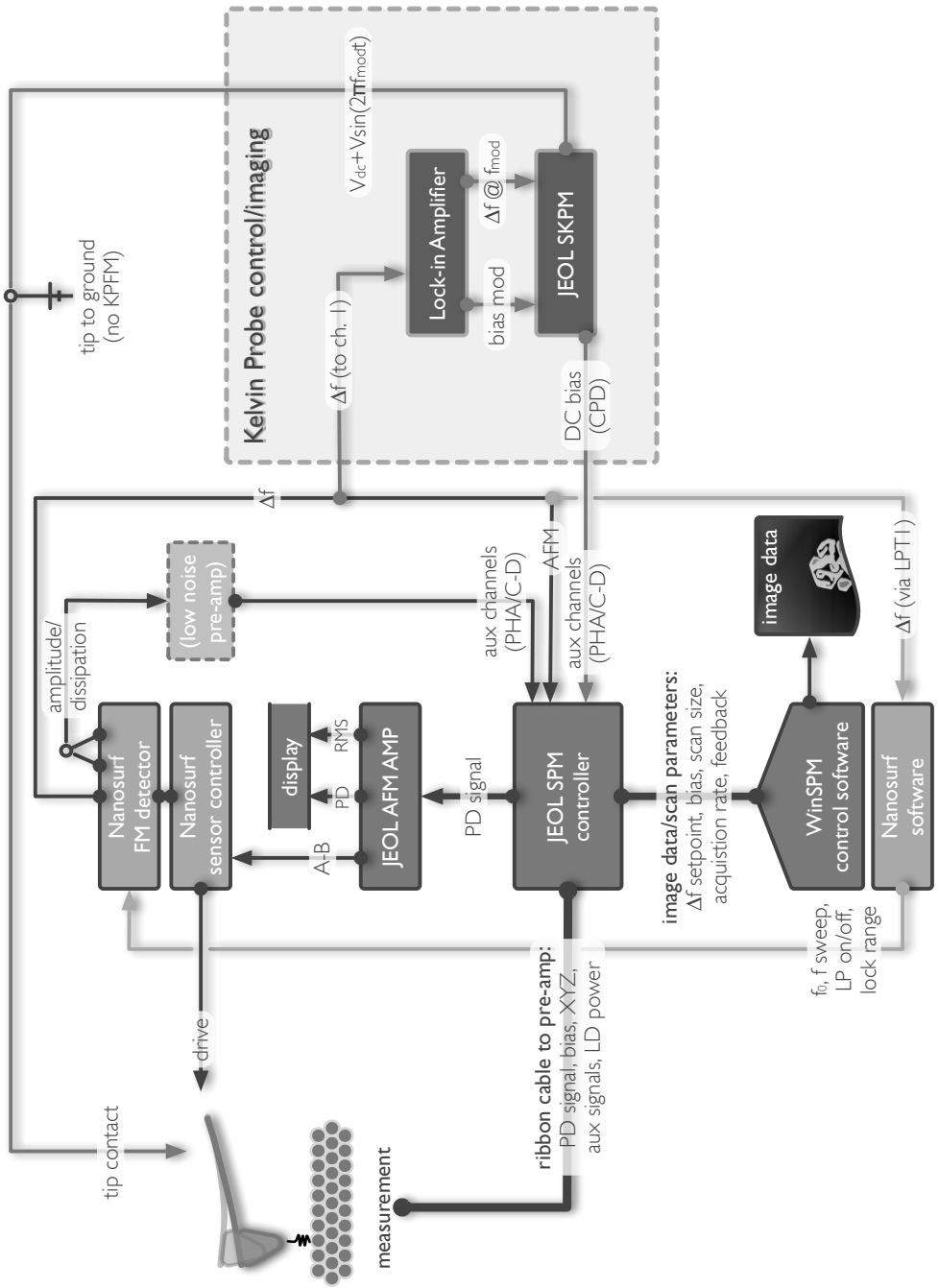

Figure 2.21: Block diagram of nc-AFM imaging mode with JEOL controller and Nanosurf PLL and optional Kelvin Probe feedback.

3

C_{60} on Alkali Halides

THE FOLLOWING SECTION IS BASED ON TEXT FROM:

S.A. Burke, J.M. Mativetsky, S. Fostner, P. Grütter. C_{60} on alkali halides: Epitaxy and morphology studied by noncontact AFM. *Phys. Rev. B* **76**:035419, 2007.

Includes expanded introduction additional material and analysis available subsequent to publication.

3.1 Introduction

Research into the optical and electronic properties of organic molecules, as well as the influence of structure on these properties, has received substantial interest in recent years due to the prospect of using molecules as active electronic and opto-electronic materials. The idea of fine tuning the properties of single molecules and molecular materials through functionalization, as well as controlling self-assembly and tailoring structuring by customizing the intermolecular interactions and interactions with substrate structures [108, 109], gives molecules and molecular materials much of their promise as "building blocks" for electronic and optoelectronic devices. Though there has been a great deal of excitement regarding the promise of single molecule electronics, there remain formidable challenges in implementing reliable devices with the characteristics demanded by our current technological needs [13]. In parallel, thin film organic electronics and opto-electronics has been developing, with some products already making their way into the marketplace [17, 18], though there remain challenges here as well in making organic devices competitive with current technologies.

In order to improve organic thin film devices, growth and morphology of organic materials on inorganic surfaces have been studied extensively [15, 110]. It has been shown that the structure of the films and the number and types of defects present are critically important to the properties to be exploited in device applications [19, 110]. As such, understanding the growth of such films is crucial to the development of better devices.

However, even though insulators play an important role in most device structures, the majority of molecular studies have been conducted on metallic and semi-conducting substrates. Difficulties with the use of typical electron beam based surface science tools on insulators include charging of the surface and electron beam damage of the substrate [109]. Additionally, scanning tunnelling microscopy, which has often been used for studies of molecules on surfaces [32], requires some degree of conductivity of the substrate. In contrast, non-contact atomic force microscopy (nc-AFM) has demonstrated the ability to image insulating surfaces with atomic resolution [111] and has, in recent years, also been applied to a variety of molecular systems on insulating substrates with molecular resolution [49, 50, 51, 53, 52, 112, 59, 54]. Nc-AFM also allows characterization from the atomic and molecular scale up to the micron scale providing a connection between the molecular structure and the resulting morphology. This detailed structural characterization of such sub-monolayer molecular films are important to understanding the early stages of growth on insulators and the origins of defects in such films, as well as giving insight into the delicate balance between intermolecular interactions and substrate molecule interactions.

The C_{60} molecule was selected as a prototypical organic molecule for study on insulating surfaces. The relatively large size ($\sim$1nm) and simple spherical geometry of the molecule facilitates high resolution imaging, in comparison to a flat-lying planar molecule. To first order, C_{60} can be considered as a sphere, an approximation expected to be more or less true at room temperature where molecules in the bulk crystal are freely rotating [113]. This simplifies determination of epitaxy and makes interpretation more intuitive. C_{60} is typically observed in close packed hexagonal structures when weakly adsorbed on surfaces (see fig. 3.1).

In comparison, the alkali halide substrates: KBr(001) and NaCl(001) have square "checkerboard" ionic lattices with lattice constants slightly more than half

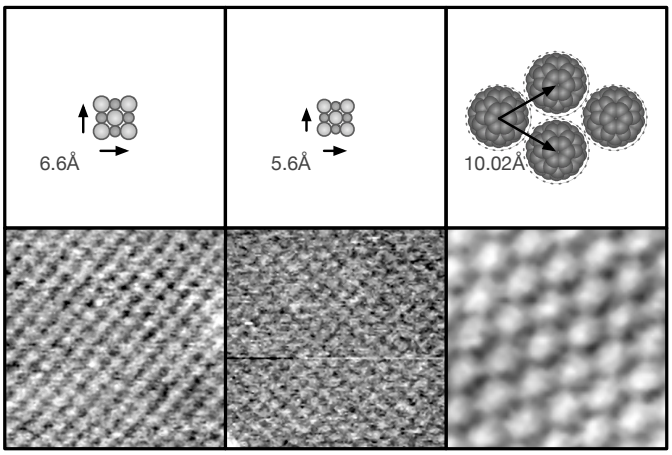

Figure 3.1: KBr, NaCl and C_{60} lattices with lattice constants with corresponding nc-AFM topographs (5nm $\times$ 5nm) below.

that of C_{60} . These alkali halide surfaces have similar chemical characteristics, while the lattice constant of KBr and NaCl differs by 1Å (see fig. 3.1) allowing for a comparison of the effect of substrate lattice constant without significant changes in adsorbate–substrate interaction. Additionally, these surfaces can be prepared cleanly and with very few defects and large terraces allowing for growth studies which are not dominated by the influence of factors which are difficult to characterize. These surfaces have been studied in detail by nc-AFM [111, 42, 44, 45] such that preparation techniques and imaging conditions for atomic resolution are generally known.

Sub-monolayer coverages of C_{60} on the (100) surfaces of alkali halides are examined herein. The C_{60} molecule has been studied on a variety of surfaces, including several studies of film growth on alkali halides [114, 115, 116, 51, 117], though the principle goal in many of these has been to achieve high quality thick films, rather than study the processes in the early stages of growth. Sub-monolayer coverages of C_{60}, deposited on room temperature, UHV-cleaved NaCl were observed by Lüthi *et al.* [117] with molecular resolution by AFM. Hexagonal and triangular islands typically 2-3 layers high were observed and found to nucleate predominately at step edges, and although atomic-scale resolution was obtained on both the C_{60} overlayer and NaCl substrate, no simple epitaxial relation could be determined. Kim *et al.* [114] used AFM to study the morphology of both islands

and films of C_{60} on KBr grown at elevated substrate temperatures. At the lower coverages examined, they observed large crystalites with triangular and hexagonal edges and concave centers similar to those discussed here for high temperature growth. Our own previous investigation [51] of submonolayer coverages of C_{60} deposited on room temperature, UHV cleaved KBr showed an unusual branched island morphology which had not been previously reported. The lack of explanation for these island shapes and their rather interesting form has compelled a more detailed investigation into the morphology and its connection, if any, to the atomic-scale structure of the crystallites. Here, both qualitative and quantitative characterizations of shape are used to examine the influence of growth parameters; namely the deposition rate, coverage, substrate and temperature, on the resulting island morphologies. Energetic considerations and equilibrium morphology are also addressed.

3.2 Experimental Details for C_{60} on Alkali Halides

The substrates used for these are single crystal alkali halides, specifically KBr and NaCl (see Appendix B for sources and preparation). Both have a cubic rock-salt structure with (100) cleavage planes. The (100) planes exposed by cleaving consist of a square checkerboard pattern of positive (K+,Na+) and negative (Br-,Cl-) ions. Though similar in chemical composition, the lattice constant of the two surfaces differs by 1Å with the conventional cell lattice constant of KBr being 6.6Å and the lattice constant of NaCl being 5.6Å with no significant deviation at the surface [118, 119]. The substrate surface was imaged with nc-AFM prior to deposition of molecules. KBr and NaCl (100) surfaces prepared in this way often exhibit atomically flat, defect-free terraces up to, and sometimes in excess of, 1μm.

C_{60} obtained from Alfa Aesar (99.95%) is further purified by heating to 220°C in vacuum for 14 hours. Molecules are deposited *in situ* by thermal evaporation from quartz crucibles (Kentax, Germany) at 330°C onto room temperature or heated substrates as prepared above. C_{60} molecules deposited on surfaces most often form a hexagonal structure corresponding to the (111) plane of the bulk fcc structure with lattice constants very similar to those in the bulk which exhibits a nearest-neighbour distance of 10.05Å while the molecule itself has a van der Waals

diameter of 7.1Å [113].

3.3 Morphology of C_{60} on KBr and NaCl

On both KBr and NaCl, C_{60} exhibits an island growth mode for deposition onto a room temperature substrate. Even at sub-monolayer coverages, molecular crystallites are two or more molecular layers high. Diffusion lengths on both substrates are estimated to be in the range of 600nm to 1μm as reported previously for KBr [51, 115]. The molecular islands predominantly nucleate at step edges on both surfaces, due in part to the large diffusion length and a preferred nucleation site at the step, particularly at kink sites [51]. The large diffusion length, as well as an island growth mode, indicate a relatively weak interaction with the surface on both substrates.

In most cases a combination of two different types of islands were observed after depositing C_{60} molecules: compact and branched (shown in figure 3.2). Compact islands maintain a generally hexagonal crystal border and are typically two or more layers tall, often with incomplete upper layers. Branched islands are generally two layers tall, often with enclosed first layer regions, and sometimes with incomplete additional layers. These islands maintain a hexagonal symmetry, but also exhibit a dendritic-like branched structure. However, these branches often wrap back in towards the center of the island which is not characteristic of most dendritic structures. Additionally, these branched islands are often composed of disconnected regions which appear to be associated and have the same orientation with respect to the substrate. High resolution imaging across a gap between disconnected regions confirms that the two separate pieces do indeed have the same orientational relation to the substrate (see fig. 3.3).

Measuring the distance across such a gap could potentially reveal whether the two disconnected regions formed independently or were originally a part of the same island which later became separated. However, unless a very small gap is measured, ie. a very small number of molecules is missing, even a small error in measuring the gap is amplified by the number of sites to be counted and the error in the determined lattice constant. For example, a cut across the gap from the image shown in fig 3.3 gives a distance of 18.90$\pm$0.05nm. Taking the lattice

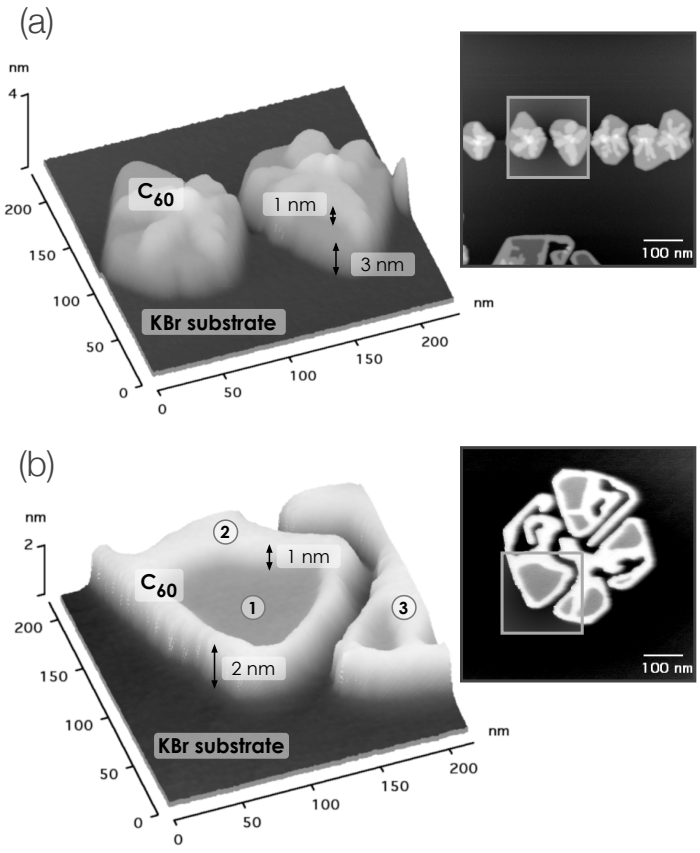

Figure 3.2: Examples of the two island types observed for C_{60} on alkali halides: (a) compact multi-layer islands with incomplete upper layers and (b) branched 2-layer islands (2) with enclosed 1st layer regions (1) and disconnected regions (3).

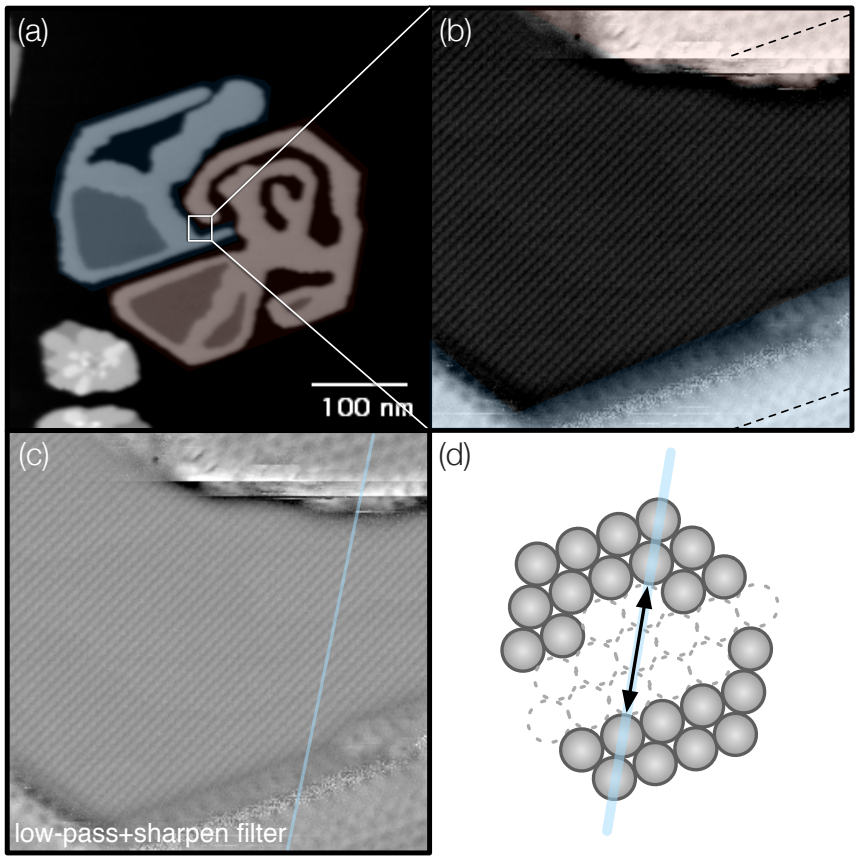

Figure 3.3: C_{60} island with two disconnected regions: (a) overview ($\Delta f = -1.9$Hz, 440×440nm) and (b) high resolution ($\Delta f = -13.0$Hz, 20×20nm, high pass filter + original image) showing alignment of molecular overlayer across the gap, dashed lines are parallel. Red and blue tinted regions in both images indicated the two disconnected regions, indicating that the top region of molecular contrast in (b) belongs to the lower right segment in (a) and the bottom region of molecular contrast is taken from an edge of the upper left segment in (a). (c) same image as (b) with low-pass filter and sharpen filter showing a slice along one lattice direction across the gap which is expected to be an integer number of lattice spacings based on the idea that the two segments originated as one island, schematically shown in (d).

spacing determined from the epitaxial unit cell (discussed in a later section) for this lattice direction, the number of "missing" molecules is 19.9±0.4. While this is very close to an integer number, the error is too large to confidently ascribe an integer value.

On KBr, several different coverages and rates were examined (see fig. 3.4 for an overview). There is little variation of the morphology with coverage. At lower coverages the island sizes are smaller, approaching the branch width, and thus the branches are less extended making the islands appear more compact. For all coverages, a mixture of compact and branched islands could be observed. There is also little variation in the character of the growth over the accessible range of rates for the same coverage. Again, both branched and compact islands appear and there is no obvious difference in the degree of branching. It should be noted that the island size is influenced considerably by the substrate structure, mainly the density of steps. The images in figure 3.4 were selected to be representative of similar substrate areas. Some apparent differences in the island morphologies are a result of different local substrate morphology. For example, in the image shown for 0.1 ML at 0.0077 ML/s the islands appear more compact. However, due to a higher density of steps in this region compared to some of the other areas shown for this coverage, the island sizes are smaller making them appear less branched. This effect, caused by the increased nucleation at step edges in combination with diffusion lengths often longer than terrace sizes, demonstrates the importance of preparing very clean flat surfaces for growth studies of these systems as well as understanding the role of steps and defects on film growth for device applications.

To quantify the shape information, the images were characterized based on perimeter and area measurements of individual islands. Figure 3.5 shows a typical dimensionality plot (log(Area) vs. log(Perimeter)), or Perimeter-Area relation (PAR) plot, taken from measurements of many [1] islands from the same sample, ie. identical rate and coverage. The most striking feature is a transition of the slope from a value of 2, as expected for compact shapes, to 0.9 ± 0.1. The value of this

[1] A total of 611 islands were parameterized using the JEOL WinSPM software, taken from 9 different samples, or 17-90 islands from each sample, representing different preparation conditions. To avoid systematic error introduced by inaccuracies in the area and perimeter measurement algorithms, islands with areas less than 100 pixels were excluded. By using the area in pixels as the cutoff, differences between image sizes are also reduced (above the cutoff, the differences for the same island are within the given error bars).

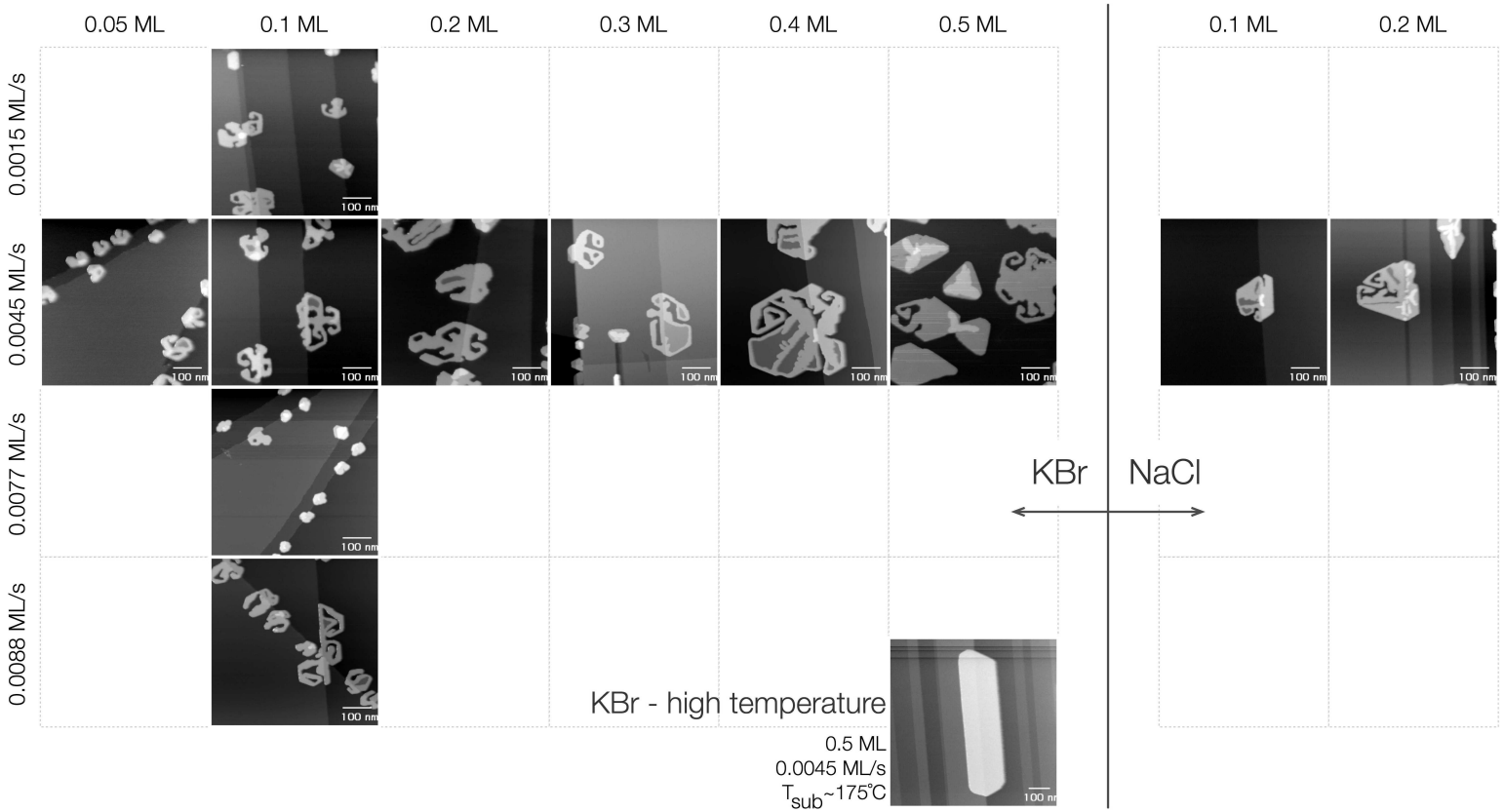

Figure 3.4: Overviews of C_{60} on KBr and NaCl with different rates, coverages, substrates, showing similar, representative areas. All images 600×600nm.

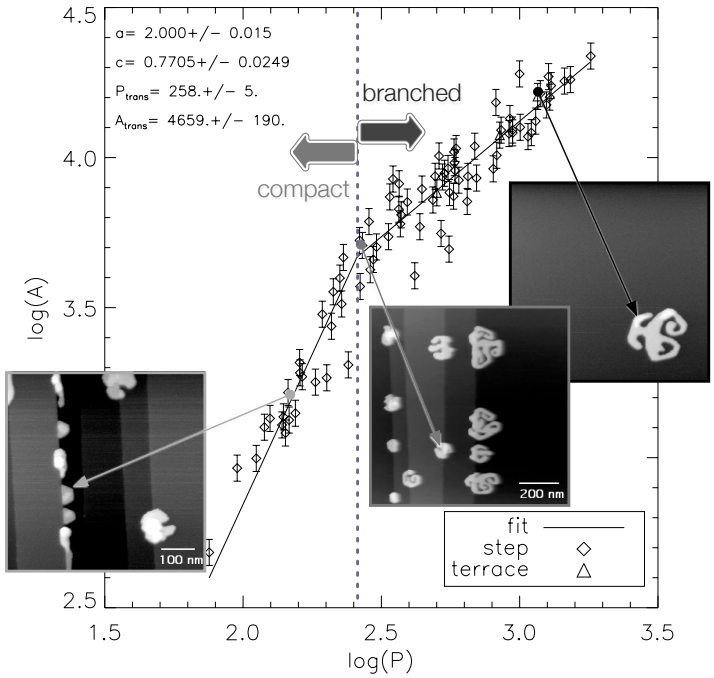

Figure 3.5: A typical dimensionality plot for a given rate and coverage (∼0.004ML/s, 0.1ML). Images of the particular islands corresponding to points on the graph are shown for three key regions: the compact, slope=2 region, near the transition, and above the transition where branching is fully developed. The parameters in the upper left corner are defined as: a and c are the slopes for the compact and branched regions respectively, P_{trans} and A_{trans} are the perimeter and area, respectively, at which the transition occurs.

second slope is related to the fractal dimension by [120, 121]

$$P = \alpha D' A^{D'/2} \tag{3.1}$$

where P is perimeter, A is area, α is a constant, and D' is the fractal dimension of the 2-dimensional island perimeter, yielding a fractal dimension of $D' = 2.2 \pm 0.2$ corresponding to islands after the transition. Interestingly, the fractal dimension remains constant, within error, over all rates and coverages explored for both substrates indicating that the degree of branching is not significantly affected by the growth parameters, ie. rate and coverage, or by the substrate (see fig. 3.6c).

The second parameter which can be extracted from the dimensionality plots

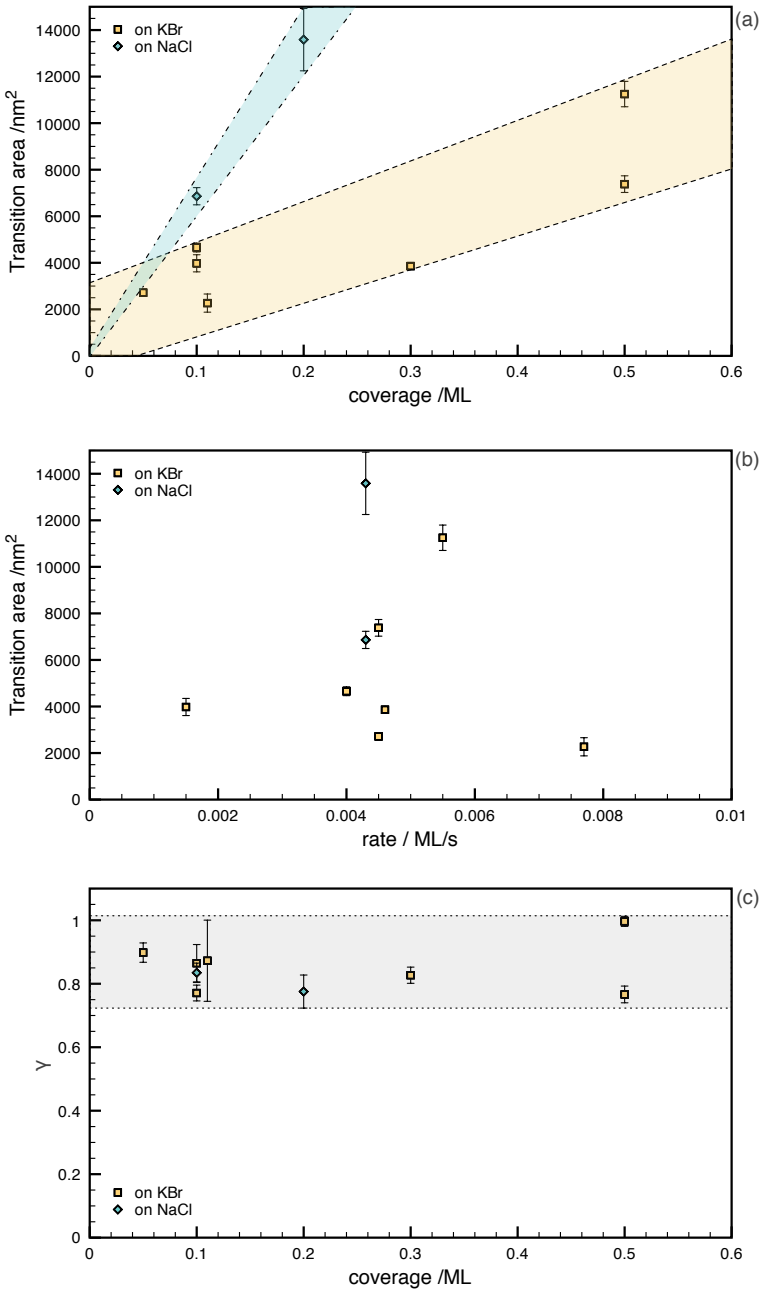

Figure 3.6: The plot in (a) summarizes the area at which the transition occurs as a function of coverage and shows the difference in trends for KBr and NaCl, represented approximately by the coloured areas. Plot (b) shows the area at which the transition occurs as a function of deposition rate. Over the range of rates available at the deposition temperature, there is no notable trend as a function of rate. The plot in (c) shows γ, the slope after the transition, as a function of coverage, which is constant over all rates and coverages within error.

is the island size at which the transition occurs (i.e. where the slope deviates from a value of 2). This transition area increases slightly with coverage for C_{60} on KBr (see fig. 3.6a). For islands on NaCl, the data shows that the transition consistently occurs at larger area, i.e. islands are larger before becoming branched, and has a steeper dependance on coverage. No significant trend was distinguished for the dependence on rate (fig. 3.6b). In contrast to the transition area, however, the branch width remains roughly constant regardless of coverage, rate or substrate. Average values and standard deviations of measured branch widths were 27.1 ± 8.2nm and 25.2 ± 8.7nm for KBr and NaCl, respectively, with similarly small variations in the average value and the standard deviation for different rates and coverages.

The second characterization which has been applied is a dimensionless shape factor which is normalized to a circle (sometimes also referred to as the compactness):

$$S.F. = \frac{4\pi A}{P^2} \tag{3.2}$$

where A is the area and P is the perimeter. This gives a way to characterize how compact the shape is, and in the case of particular shapes, allows an identification of the shape; for example, a regular hexagon has $S.F. = 0.906$. In the dimensionality plots a change in compact shape would appear as a change in the intercept, with the same slope, whereas the shape factor would exhibit steps for changes in shape making such a transition easier to identify. A typical plot of the shape factor as a function of island area is shown in figure 3.7. For the C_{60} on KBr data analysed, the shape factor indicates a roughly hexagonal shape for the compact region with no significant indication of a change in compact shape. After the transition to branched behaviour, the curve follows the trend extracted from the dimensionality plots towards a line-like shape; or in terms of the branching, an increasing branch length with increasing the island size.

Despite differences in orientation between islands nucleated at steps compared with those on free terraces, the trends in shape followed by the islands are the same regardless of where on the surface the island is located. The typical dimensionality plots shown in figures 3.5(a) and 3.7 include data points from both steps and terraces which clearly follow the same trend (see in particular the en-

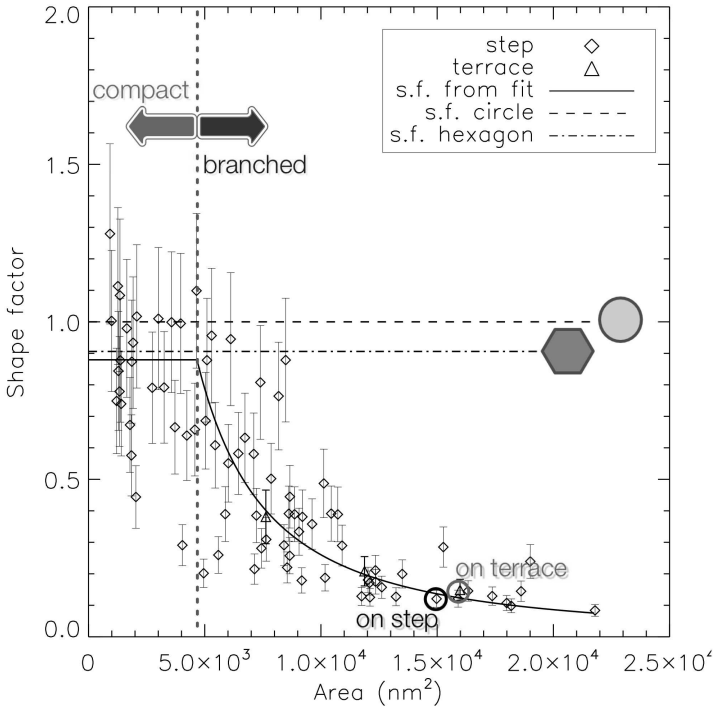

Figure 3.7: Typical plot of the Shape Factor (see equation 3.2) as a function of island area for the same sample shown in fig. 3.5(a). Up to the transition area, denoted by the vertical dashed line, the shape is roughly hexagonal. At areas greater than the transition area the shape approaches S.F.=0, or "line-like". The solid line corresponds to the fit from the dimensionality plot in fig. 3.5(a). The two encircled points show islands with both similar areas and similar shapes one of which was positioned at a step and the other positioned on an open terrace.

circled points in fig. 3.7). This indicates that the island shapes are not dependent on the details of nucleation or initial growth. This will be addressed further in relation to the molecular epitaxy.

3.4 Epitaxy on step and terrace on KBr

The high resolution imaging capability of the nc-AFM technique allows for real-space determination of surface structures. In particular, if both the overlayer and substrate structure can be resolved, the lattice parameters of the overlayer can be corrected for any drift, creep or non-linearities in the piezo, thus improving the confidence in the measured lattice constants (see Appendix E for details). In many cases, determination of the overlayer relation to the substrate is only possible when the substrate is also resolved, as the uncertainty in the measured lattice constants may be too large to ascribe a unique superstructure, especially for large epitaxial cells.

Nc-AFM topographic images showing resolution on both the substrate and the overlayer (see fig. 3.8(a)) over the edge of an island situated on a terrace are used to determine the overlayer relation to the substrate. As the KBr lattice parameters are well known [119], the lattice parameters measured from the image are used as a calibration and the determined transformation is then used to correct all other measurements within the image. Measuring the C_{60} lattice and applying the appropriate correction yields lattice constants of $b_1 = 10.3 \pm 0.2$Å and $b_2 = 9.8 \pm 0.4$Å with an angle between the two lattice vectors of $\beta = 61 \pm 2^\circ$. The rotation of the overlayer lattice relative to the <100> direction of the conventional unit cell of the KBr is also measured and corrected and found to be $\theta = 17.1 \pm 0.7^\circ$. Using these lattice constants and the overlayer rotation, with the known lattice constants of KBr, one can calculate the expected transformation matrix which describes the overlayer relation defined as [31]:

$$\begin{bmatrix} \mathbf{b}_1 \\ \mathbf{b}_2 \end{bmatrix} = [\mathbf{C}] \begin{bmatrix} \mathbf{a}_1 \\ \mathbf{a}_2 \end{bmatrix} = \begin{bmatrix} p & q \\ r & s \end{bmatrix} \begin{bmatrix} \mathbf{a}_1 \\ \mathbf{a}_2 \end{bmatrix} \tag{3.3}$$

where the $\mathbf{b}_i$ are the molecular overlayer lattice vectors, and the $\mathbf{a}_i$ are the substrate

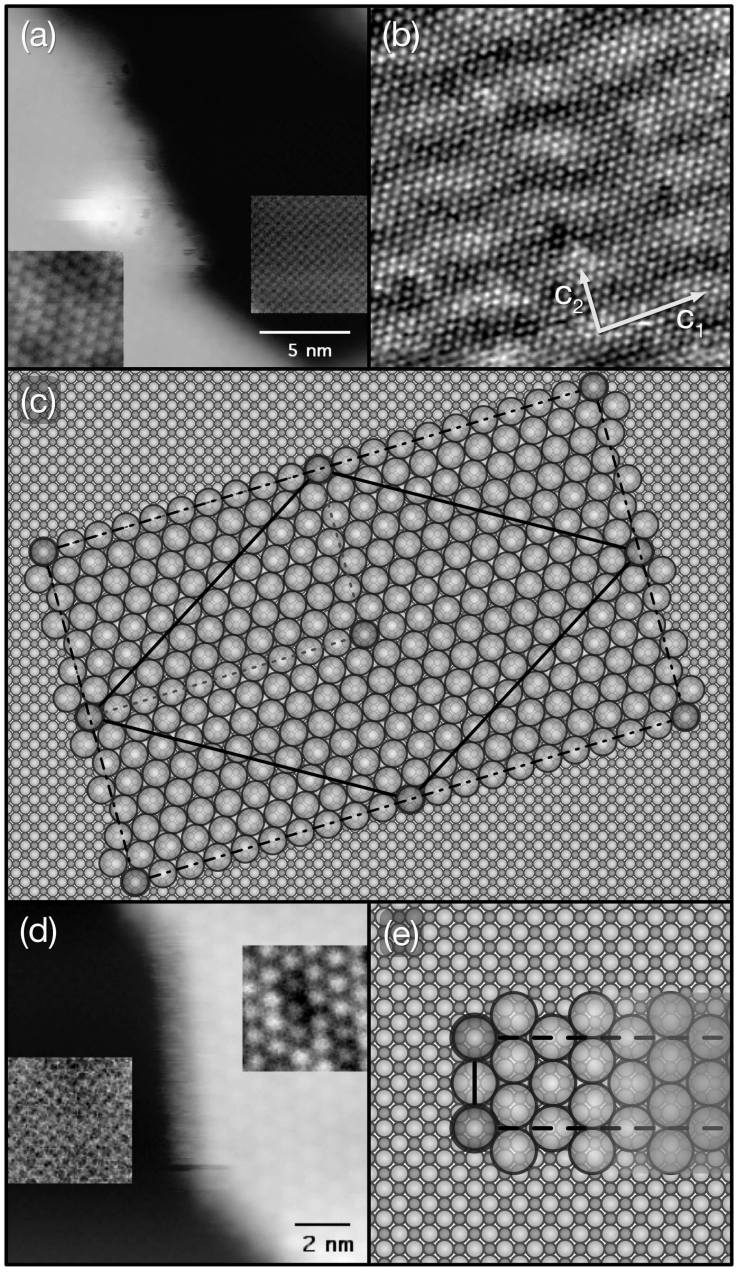

Figure 3.8: High resolution imaging of a C_{60} island found on an open terrace is shown over the edge of the island with KBr resolution in (a) ($\Delta f = -13.0$Hz, 20×20nm), and on a first layer region in (b) ($\Delta f = -7.0$Hz, 30×30nm) with the vectors c_1 and c_2 representing the periodicity of the moiré. The corrugation of the moiré is $\sim$10pm, with a C_{60} corrugation of $\sim$20pm. One of two possible coincident structures is shown in (c) based on high resolution imaging. High resolution imaging over the edge of an island found adjacent to a step is also shown in (d) ($\Delta f = -11.3$Hz, 13×13nm) [51] with the corresponding $n \times 3$ structure observed in (e).

lattice vectors. Classification of the type of epitaxy can be made from the matrix elements p, q, r, s which define the positions of the adsorbates relative to the substrate. In molecular epitaxy, coincident structures are far more common than in inorganic epitaxy and there are several sub-classifications which can be made (see ref [31, 122]).

In this case, the matrix calculated from the measured, and corrected lattice parameters gives the coincident relation:

$$\mathbf{C} = \begin{pmatrix} 1.49 \pm 0.03 & 0.46 \pm 0.02 \\ 0.31 \pm 0.06 & 1.45 \pm 0.06 \end{pmatrix} \tag{3.4}$$

In high resolution images of 1st layer C_{60} regions, a long range periodicity is observed with a weak corrugation of $\sim$10pm compared to the C_{60} corrugation of around 20pm. If it is assumed that this moiré pattern is a result of the overlayer - substrate correspondence then it can also be used to arrive at the transformation matrix. The periodicity of the observed moiré can be described by a new set of lattice vectors in terms of the C_{60} lattice vectors:

$$\mathbf{c}_1 = \quad 10\mathbf{b}_1 \tag{3.5}$$

$$\mathbf{c}_2 = -3\mathbf{b}_1 + 7\mathbf{b}_2 \tag{3.6}$$

Using the calibrated C_{60} lattice constants and measured angle of the overlayer with respect to the KBr to determine the moiré pattern in terms of the KBr lattice and equating the two, one arrives at the transformation matrix giving:

$$\mathbf{C} = \begin{pmatrix} 1.48 \pm 0.03 & 0.45 \pm 0.01 \\ 0.30 \pm 0.01 & 1.44 \pm 0.06 \end{pmatrix} \tag{3.7}$$

As the two matricies agree to within the small errors on each of the matrix elements, it is likely that the observed long range periodicity is caused by overlayer - substrate correspondence. Possible mechanisms for the observed moiré contrast in the nc-AFM topography include geometrical effects where the C_{60} lattice is in and out of registry with the KBr lattice minima changing the adsorption distance, geometrical differences between differing adsorption geometries and orientations

[123] and electrostatic effects caused by the interaction of the molecules with the underlying ionic lattice. From the matrix elements found there are two possible coincident structures that are consistent with the periodicity of the moiré within the range of errors given for the matrix elements:

$$\begin{pmatrix} 3/2 & 9/20 \\ 2/7 & 207/140 \end{pmatrix}, \begin{pmatrix} 3/2 & 9/20 \\ 2/7 & 197/140 \end{pmatrix} \tag{3.8}$$

The first of these is shown in figure 3.8(c). As it corresponds to C_{60} lattice constants which are more similar to the equilibrium spacing of C_{60}, it is a more likely structure given the weak interaction between C_{60} and KBr, though the two cannot be distinguished by the measurements presented here. In both cases, the periodicity of the moiré (shown in fig. 3.8c) by the grey dashed line) does not correspond to an integer number of KBr lattice constants, but rather 1/2-integer values corresponding to the position of the opposite ion. This tends to support a geometrical rather than an electrostatic mechanism for the observed contrast, as the contrast would be expected to differ over opposite ions if it were a purely electrostatic effect. It is hoped that detailed modelling of the overlayer structure and simulation of nc-AFM imaging of such an overlayer structure will shed light on the mechanism responsible for the observed moiré pattern.

Calculations were also performed[2] to determine the stable adsorption sites of C_{60} on KBr [124]. Based on these preferred sites a unit cell very similar to the experimentally determined cell can be derived:

$$\begin{pmatrix} 3/2 & 1/2 \\ 1/3 & 3/2 \end{pmatrix} \tag{3.9}$$

which results in rows of C_{60} on three of the stable adsorption sites, namely the pentagon-bridge, hexagon-Br^- top, and the pentagon-K^+ top, or a similar structure where the C_{60} is rotated to interact with the K^+ ion through bond between the pentagon and hexagon (5-6 bond). Despite the close comparison of this unit cell to

[2]DFT calculations determining the energetically favourable sites, binding energies, and changes in electronic structure due to interaction with the lattice were performed by Wei Ji of the Beijing National Laboratory for Condensed Matter Physics, Chinese Academy of Sciences in the group of Hong-Jun Gao, while visiting the group of Hong Guo at McGill University.

the experimentally determined unit cell above, we do not believe this is the final structure as the geometrical height differences between the different orientations would result in alternating rows of different heights rather than the long range 2-dimensional periodicity observed. Rather, this structure can be considered as maximizing the interaction with the surface, but may be energetically unfavourable when also considering the intermolecular interactions which were not included in the determination of preferred adsorption sites[3]. As the C_{60} lattice would be deformed to achieve the calculated adsorption structure, the intermolecular interactions would drive the system towards a structure closer to the equilibrium crystal lattice. We can envision these two competing interactions resulting in (a) undulations in the lattice as the molecular lattice comes in and out of phase with preferred adsorption sites altering the adsorption height, akin to the formation of solitons, and (b) possible metastable states whereby a layer following the preferred adsorption sites might be formed but not represent the energetic minimum due to intermolecular interactions.

The relation of the C_{60} overlayer to the KBr substrate for an island located at a step was previously reported [51]. In this case, a coincident epitaxy was determined with an 8×3 supercell. As the long direction of the supercell could not be determined exactly from the measured lattice constants an energetic consideration of possible cells was used to determine the most likely structure [106]. In similar situations where islands are found at <100> steps, other $n\times3$ structures have been observed where in the direction of the step there is an alignment with the KBr and two molecules for every three KBr conventional unit cells (shown schematically in fig. 3.8(e)). In the direction which is not aligned, there seems to be some freedom for different structures to occur. This alignment with the <100> direction is in contrast to islands found on free terraces which consistently show a rotation of $\sim20^\circ$ relative to the KBr lattice. This clearly indicates that the nearby <100> step influences the epitaxy by forcing an alignment of one of the overlayer lattice vectors with this direction.

It is interesting to note that although the epitaxy for molecular islands on open terraces and at steps differs significantly, the large scale morphology, as

[3]As intermolecular interactions are usually dominated by van der Waals interactions this could not be included readily in the DFT calculations required to determine stable adsorption sites.

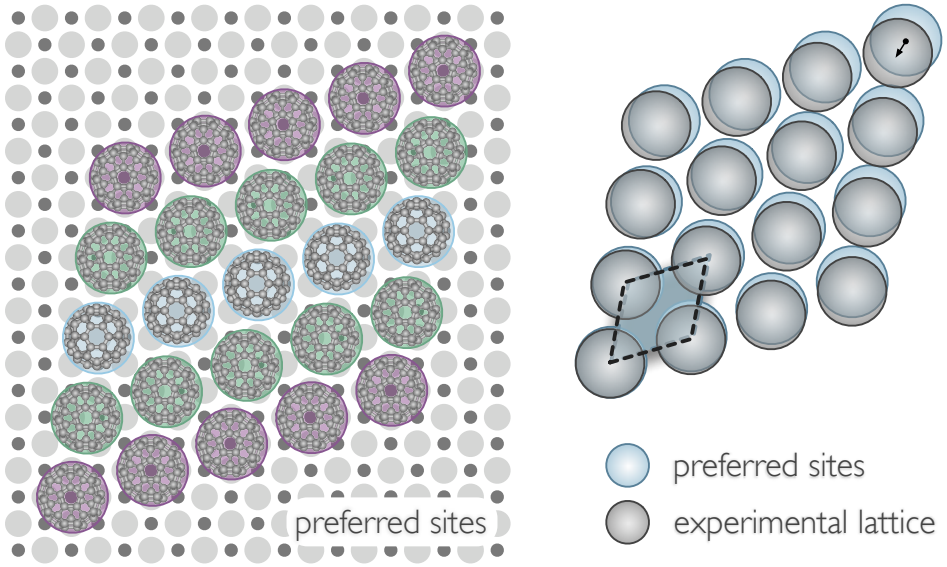

Figure 3.9: Left: lattice consisting of preferred adsorption sites; pentagon-K^+ top, hexagon-bridge, and hexagon-Br^- top, giving the theoretically predicted unit cell. Right: comparison of theoretically predicted unit cell and the experimentally determined lattice showing displacement of measured lattice from preferred sites.

stated previously, follows the same trend irrespective of location on the substrate. Additionally, the behaviour on NaCl, which has a smaller lattice constant compared to KBr, is also strikingly similar. Although simultaneous resolution on C_{60} and NaCl was not obtained, the epitaxy will be, by necessity, also somewhat different to fit the underlying substrate lattice. The lack of a connection between the morphology and the atomic/molecular scale features indicates that the mechanism responsible for the island shapes is dictated by a larger scale, collective interaction rather than through strain or the molecule substrate interaction.

3.5 Energetics and dynamics of growth

To explore the energy landscape of the growth, C_{60} was deposited on KBr, using the same coverage and rate, either onto a heated substrate or onto a room temperature substrate and later annealed or allowed to age. A coverage of 0.5 ML of C_{60} was deposited at a rate of 0.0045 ML/s on a KBr substrate held at 175°C, shown

in figure 3.10(b) as well as in the lower inset of figure 3.4. Compact islands ranging in shape from elongated hexagonal crystals to nearly triangular crystals, with heights greater than 4 nm were observed. Distances between islands were often larger than 1 μm despite intervening steps due to increased diffusion on the surface at elevated temperature. These observations, particularly the island shapes, are consistent with previously reported results for C_{60} on KBr at elevated temperature [114]. As compared to the growth at room temperature for the same coverage and rate which exhibits the branched island morphology described in section 3.3, and shown in figure 3.10(a), the island morphology is significantly influenced by the substrate heating.

In contrast, though annealing does have some effect, the islands do not transform to a compact island morphology. The room temperature deposited sample shown in figure 3.10(a) was heated to 175°C for 16 hours. The sample after annealing, shown in figure 3.10(c), does not contain any first layer enclosed areas as observed prior to annealing, indicating that this 1st layer region is meta-stable. A similar effect can be noted in an aged sample (9 days after deposition), shown in figure 3.10(d), where the majority of interior holes do not contain any 1st layer C_{60} and the small portions that are observed are broken up and surrounded by small branches.

Additionally, after annealing, there is evidence of some evaporation from the edges of the island exhibited by the increased roughness of the island edges. Annealing of a different sample to 250°C for 16 hours resulted in complete evaporation of the C_{60} from the surface. Although there may be an intermediate temperature where annealing causes a change in morphology from branched to compact islands, the evidence of some degree of initial evaporation even at the lower annealing temperature indicate that the barrier to the rearrangement of existing branched islands is quite large, likely similar to the desorption energy. In other words, the branched structures are relatively stable once formed, due to a significant C_{60}-C_{60} interaction in comparison with the binding to the substrate, and there is an inability even at this elevated temperature to achieve sufficient long range diffusion to enable such a rearrangement. However, when the system is given more energy during growth, as in the case of a heated substrate, the islands form compact shapes and this is taken to be the equilibrium morphology.

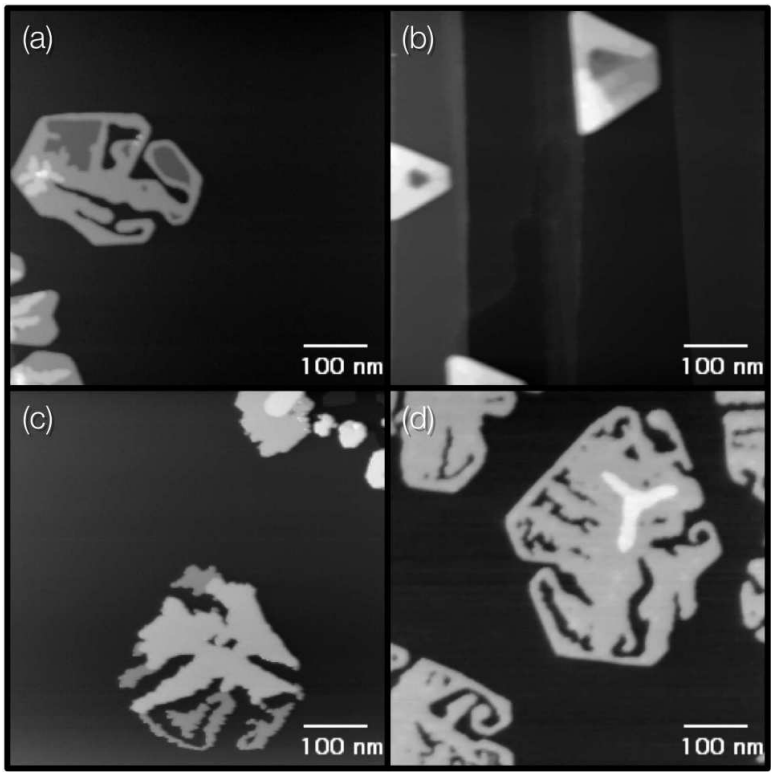

Figure 3.10: (a) 0.5 ML C_{60} deposited at 0.0045 ML/s on KBr at room temperature (Z_{max}=4.79nm), (b) 0.5 ML C_{60} deposited at 0.0045 ML/s on KBr at 175 °C (Z_{max}=16.6nm), (c) same sample as shown in (a) after annealing at 175°C for 16 hours (Z_{max}=5.63nm), (d) 0.5 ML C_{60} deposited at 0.0045 ML/s without annealing, aged for 9 days (Z_{max}=3.39nm). Though annealing, and similarly aging, has some effect on the structure the overall branched morphology remains, whereas depositing molecules onto a heated substrate results in a compact island morphology.

The detailed mechanism for creating the branched structures observed has yet to be determined. Generally fractal or branched structures caused by a "hit and stick" or limited edge and/or corner diffusion do not exhibit branches which wrap back toward the center of the island [125]. Rather, those structures tend to branch outward from a central nucleation point, unlike those seen here. The different appearance and correspondingly different fractal dimension makes this kind of growth mechanism an unlikely candidate for the formation of the structures formed by the C_{60} deposit.

An indication of a suitable mechanism comes from a series of images acquired before the structures had completed formation, seen in figure 3.11. The first of these images was taken $\sim$45 min after deposition of C_{60} onto NaCl, and shows three areas of first layer C_{60} which are *not* enclosed by a second layer rim as was shown and discussed for typical stable islands at later time (eg. figure 3.2(b)). As indicated by the annealing, and late-time observations, that the first layer is unstable, these exposed first layer areas are seen to recede from the edge in the subsequent images. At the same time as the first layer recedes, a second layer rim is built up which protects portions of the remaining first layer. The result, $\sim$40 minutes after the first image of the sequence was taken is a stable structure exhibiting branching, enclosed first layer regions, and two very nearly disconnected portions of the island; all of the features which have been observed for this type of island. Note that tip induced forces can be excluded as the cause of the changes observed on the basis that such dynamics were not observed during normal imaging of later time stable islands.

This dynamical sequence indicates that the branched island growth may occur by an initial wetting of the alkali halide surface by single layer islands of C_{60} followed by a dewetting, which due to additional factors, such as instabilities in the receding film edge and limited long range diffusion, forms the observed stable branched structures. The proposed process would proceed from the formation of large single layer islands during deposition (see fig. 3.12 for sequence of proposed process). After the deposition is completed, this single molecular layer would destabilize at the edges. These edge molecules, which have a lower coordination, could diffuse along island edges, across corners, on top of the existing layer, or away from the island. Though each of these processes occurs on

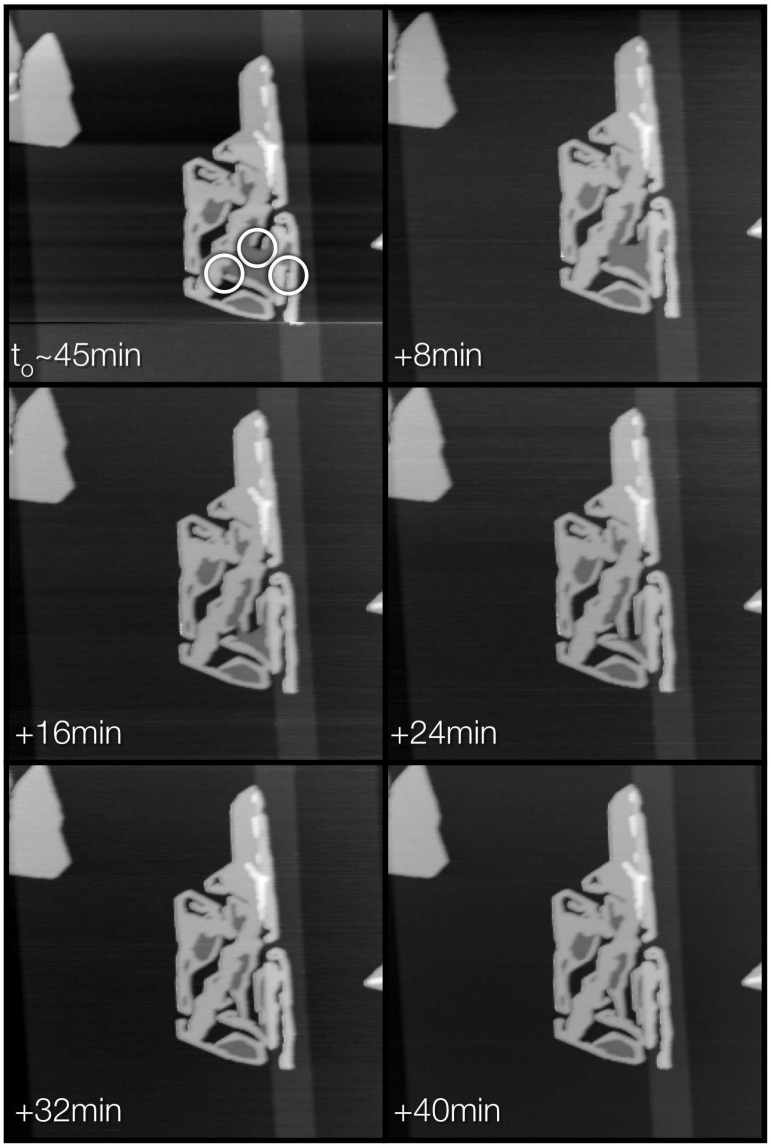

Figure 3.11: Sequence of nc-AFM images shortly after C_{60} deposition showing dynamics of the island morphology. The first images was acquired $\sim$45 min. after deposition. Three areas where a 1st layer edge are exposed are encircled. Subsequent images were taken $\sim$8 min. apart and the time from the first image is indicated. The exposed 1st layer region receeds from the edge building up a 2nd layer rim. Once enclosed, the remaining 1st layer regions are stable, as are the two layer branches. $\Delta f \simeq -2.8$Hz, 600×600nm

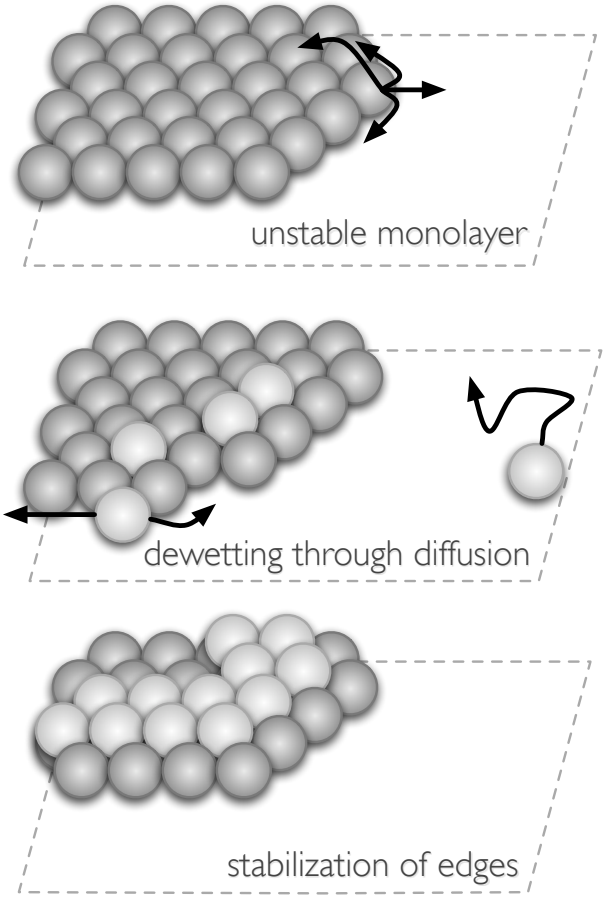

Figure 3.12: During the growth an unstable monolayer is formed through non-equilibrium processes. Upon cessation of the deposition, the layer becomes unstable and a number of diffusion processes can occur starting from the outermost edges of monolayer islands, including diffusion along the edges, away from the layer and up over the edge to form a second layer. Through random "trial-and-error" of these diffusive processes a stable configuration is found; in this case, the formation of a second layer stabilizes the edges by increased coordination. Molecules which have moved are shown as lighter grey.

very short time scales, each has a different probability associated with it, and each of many molecules must undergo such processes until a stable configuration is reached [126, 127]. The net result is a collective rearrangement process which would take significantly longer than the individual molecular motions allowing for observation of the structural changes. Those molecules which diffuse on top of the existing single layer can form a second layer rim which increases the coordination of the edge and appears to stabilize both the edge and the enclosed single layer region. The images shown here are assumed to be at a late stage of this rearrangement when most of the island structure is established, but some unstable regions remain and these are observed to change. It should be noted that although stable for a much longer time, the enclosed first layer also breaks and proceeds to dewet as seen for aged islands (fig. 3.10d), despite the greater co-ordination of the molecules within a layer compared to the first layer edge.

The formation of disconnected regions of island groups, and the apparent "communication" between these regions which exhibit the same orientation with respect to the substrate (see fig. 3.3) is readily explained by such a dewetting process. These related regions are initially part of the same single layer island whereby the orientation is set and later becomes disconnected through the dewetting of the film. Additionally, the epitaxy of the film is not expected to play a significant role as the interaction with the substrate in such a situation where dewetting occurs must be weak. Thus the observation that the epitaxy has little to no influence on the morphology, as shown by the uniform morphology at steps and terraces despite differing epitaxy, is also consistent with a dewetting scenario.

Although dewetting does not directly account for the formation of the branched island structures observed, similar morphologies have been observed previously as a result of dewetting phenomena. Dewetting has recently been reported in several systems of organic molecules deposited by organic molecular beam deposition on inorganic substrates [128, 129, 62, 65], and in particular, the "skeleton" island morphology described by Witte *et al.* for perylene on Cu(110) [62] exhibits some similar features to those described here. The thick branches and holes, though somewhat different than those described here due to a square rather than hexagonal symmetry, are visually similar. Also, the fairly uniform height of the observed branched islands and characteristic rim structures, which they suggest may be a result of a diffusion barrier at the edge of the island, are both features observed here for C_{60}. The presence of these similarities in conjunction with the direct observation of a single layer film receding to form these features strongly points to the occurrence of dewetting.

Furthermore, the details of the individual molecular processes mentioned above with the relative timescales and probabilities of each are likely responsible for the details of the final morphology. As such, the subtle differences in morphology between the two different substrates investigated are likely a result of differences in the molecular scale diffusion processes on each surface. Instabilities in the dewetting process, occurring on the length scale given by the transition from compact to branched islands, may initiate the formation of the branches. Though relatively fast short range diffusion can easily accomplish local stability, producing crystallographic edges and the two layers which seem to be required for stability,

it appears that there is insufficient mobility to fill in voids and troughs between branches at room temperature within reasonable experimental time scales to allow the system to reach the global equilibrium state of compact islands [126, 127].

In most cases, dewetting of a film is initiated by an increase in temperature or some other change in conditions after or during the initial deposition of the film. However, as growth is a non-equilibrium process, due to the flux of particles impinging on the sample, it is possible that a single layer film could become favorable during growth, whereas island growth may be favorable in the equilibrium case. For example, the balance of surface energies may differ during and after growth due to the flux of particles incident on the sample (which can also be interpreted as a background vapour pressure) [130, 131]. Should this occur, a layer growth mode may be favorable despite an anticipated island growth mode. However, upon ceasing exposure to the source, the balance of surface energies would shift back to favour an island growth mode, and one could expect the film to spontaneously dewet causing the structures to change shortly after deposition.

3.6 Summary of C_{60} dewetting

Nc-AFM has been used here as a surface science tool capable of bridging the characterization gap from the molecular scale up to the micron scale allowing connections between epitaxy and crystal structure to growth and morphology. Combined with quantitative characterizations of shape, this allows study of collective mechanisms, such as dewetting, and consideration of the effects of atomic and molecular scale interactions on such processes.

Molecular islands of C_{60} deposited on both the alkali halides KBr and NaCl exhibit a branched morphology above a critical transition area. These unusual morphologies are most likely a result of dewetting phenomena, though other factors related to diffusion and instabilities in the process presumably play a role in the resulting final shapes observed. Due to the domination of intermolecular interactions over molecule-substrate interactions and the collective nature of dewetting, the morphologies are seemingly unaffected by the differing epitaxies observed for islands on open terraces and those guided by <100> steps. The

similar morphology observed on the two different substrates also exhibits only subtle differences, as seen in the dependence of the transition area on coverage, whereas many aspects, such as the branch widths and fractal dimension observed, are strikingly similar again pointing to the limited role played by the substrate in the formation of the island shapes. The occurrence of dewetting in this system also gives an explanation for how disconnected regions of the same island group are observed to have the same orientation with respect to the substrate, as the regions would have been connected by a single layer at an earlier stage of the growth. In recent years, dewetting has become increasingly identified as an important process in the growth of many organic films on metals, and may also be a significant consideration in the growth of molecular deposits on insulators.

4

PTCDA on alkali halides

PTCDA, and other perylene derivatives, have been extensively studied as prototypical organic semiconductor materials. The perylene core of these molecules consists of a highly conjugated π-system making it promising for conduction. These molecules are also relatively easily functionalized with different organic groups attached to the ends of the molecule, making it attractive from a "molecular engineering" standpoint. The optical absorption spectra lie in the visible spectrum, and for PTCDA covers $\sim$400-650 nm [15]. The excellent crystallinity of PTCDA and $\pi - \pi$ stacking in the bulk crystal structure results in extended charge transfer states leading to size effects in the optical and electronic characteristics of this molecule[15, 132]. PTCDA also shows excellent crystalline ordering on a variety of substrates (for a few examples see reviews: [15, 110]).

3,4,9,10-perylene tetracarboxylic dianhydride (PTCDA) consists of a perylene core with carboxylic anhydride groups on the two ends of the molecule (see fig. 4.1). These oxygen atoms at the ends of the molecule are more electronegative than the conjugated carbons of the perylene core and draw electrons toward the ends of the molecule resulting in a quadrupole moment. It is this quadrupole moment which leads to the characteristic herringbone crystal structure of PTCDA. The bulk crystal presents two polymorphs termed "α" and "β", which differ primarily by the direction of the offset between adjacent layers of herringbone (102) planes. The lattice constants of the two polymorphs also differ by a small amount (lattice parameters with respect to the (102) plane given in table 4.1) making it possible to distinguish between the two by accurate lattice measurements alone. Typically when deposited on a surface a herringbone lattice is formed with the molecules and the (102) plane of the crystal parallel to the surface and good ordering is obtained [110].

The increased negative charge on the carboxylic anhydride end groups of

	a_1[102]	a_2 [102]	interlayer distance [133]	shift [102]
α	1.196 nm	1.991 nm	0.322 nm	0.190 nm
β	1.245 nm	1.930 nm	0.325 nm	0.195 nm

Table 4.1: Lattice parameters of (102) planes of PTCDA bulk polymorphs.

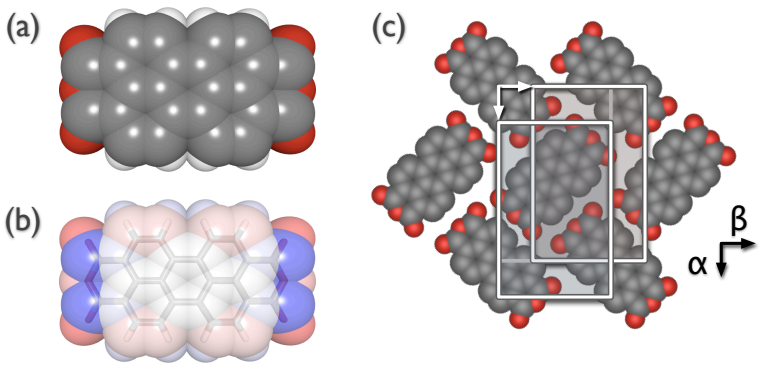

Figure 4.1: A van der Waals radius fill model representation of 3,4,9,10-perylene tetracarboxylic dianhydride is shown (a) along with an atom charge colour map (b) (generated using BALLview [70]), and a representation of the herringbone structure of the (102) plane of the bulk PTCDA crystal. Two polymorphs of PTCDA can be formed, referred to as α and β, in which there is a different shift between layers of the herringbone structure and a slight difference in lattice constants. [102]

the molecule also has the potential to interact through electrostatic forces with the positive ions of ionic surfaces such as alkali halides. Indeed, for alkali halides, the structures observed and discussed herein, indicate that such an interaction influences epitaxial structures and accompanying calculations have shown that the electrostatic interaction between the molecule and the ionic surface contribute significantly to the adsorption energy.

In this chapter, the growth, structure, and resulting properties of PTCDA on the alkali halides KBr and NaCl will be discussed.

4.1 PTCDA on KBr

To investigate the growth of PTCDA on the KBr(001) surface, different coverages, ranging from $\sim$0.2ML to $\sim$0.8ML were deposited at rates of $\sim$0.0075ML/s onto freshly prepared KBr surfaces (see Appendix B for preparation details). Island growth was observed (see fig. 4.2) similar to that observed previously for PTCDA on KBr [53], and even at low coverage only multilayer islands were found. Islands were found only at steps in the substrate even when terrace sizes exceeded 1μm indicating a very large diffusion length upon deposition. A minimum island height corresponding to three layers of PTCDA was found in agreement with that found for PTCDA in nanoscale pits on KBr [54]. It is thought that this is caused by a strained epitaxy at the interface which is stabilized by additional layers which relax to a nearly bulk structure.

The characteristic herringbone lattice can be observed on top of the PTCDA islands showing a well-ordered bulk-like structure (see fig. 4.3). Imaging over the edge of a three layer island with simultaneous resolution on the KBr substrate and the molecular island allows investigation of the overlayer relation to the substrate (see fig. 4.4). When comparing the structure of the third layer with the proposed p2x3 epitaxy [54] by means of a fourier transform (fig. 4.4 lower panel), we can see that the molecular lattice nearly fits a 2$\times$3 structure, although a small relaxation is expected for all layers beyond the interface.

A close examination of some of the KBr step edges reveals what appears to be nucleation of the PTCDA molecules along the step (see fig. 4.5a,b), which is consistent with the finding that islands are always found on step edges. A small square cluster of molecules was also found in a few cases which may indicate a dif-

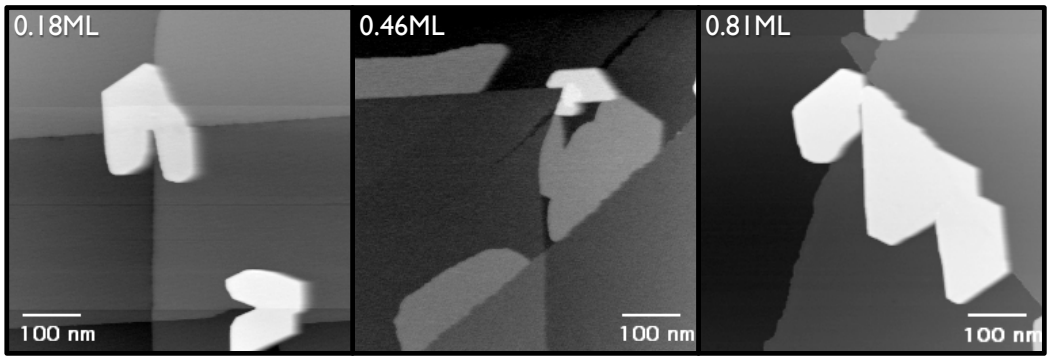

Figure 4.2: Overview images of 3 different coverages of PTCDA on KBr. Multilayer islands are observed even at low coverage. Despite terrace sizes of greater than 1μm in some cases, islands are only observed at step edges. (0.18 ML image courtesy of J. Topple.)

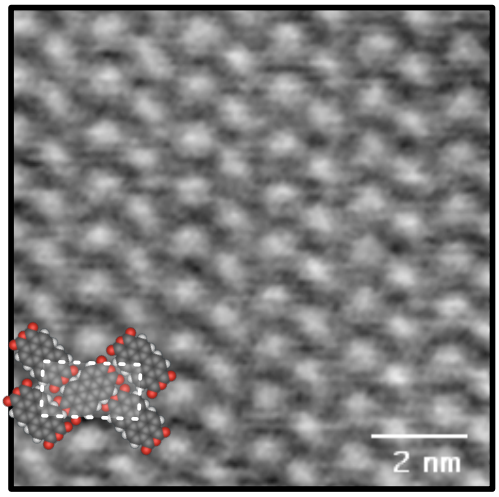

Figure 4.3: Typical herringbone lattice observed on top of a PTCDA crystallite on KBr. Herringbone unit cell is shown in lower left overlay. (Imaging parameter: Δf=-9.1, size: 10 nm $\times$ 10 nm, z-scale: 25 pm)

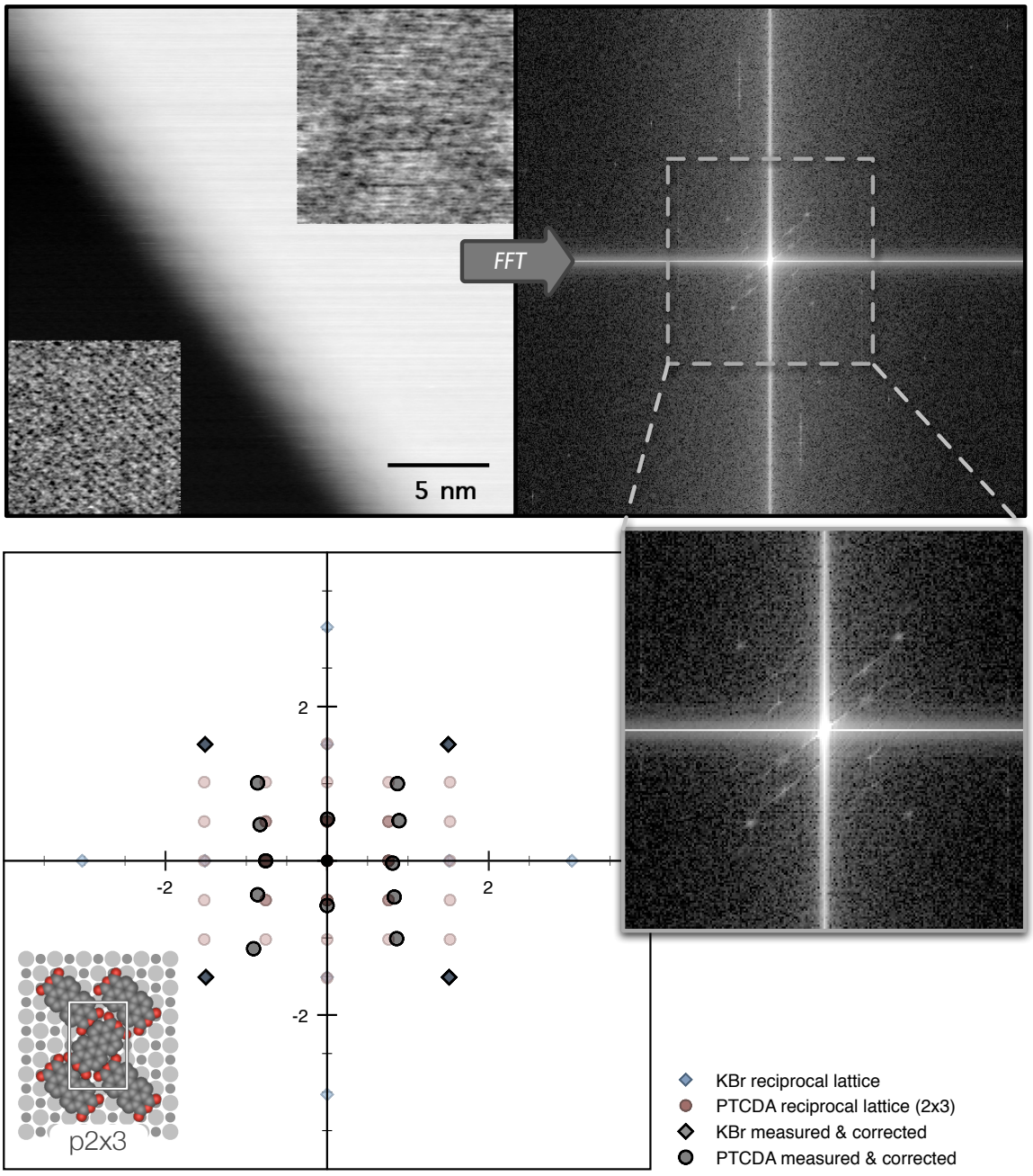

Figure 4.4: High resolution topographic image over the edge of a three layer PTCDA island showing simultaneous atomic resolution on the KBr substrate and molecular resolution on the island. (Imaging parameters: Δf=-22.5 Hz, size: 25 nm $\times$ 25 nm, z-scale: 1.3 nm, insets adjusted for optimal contrast) The fast Fourier transform (FFT) is also shown (top-right) and enlarged (below-right). The Fourier transform of the proposed 2$\times$3 structure is shown along with the measured points from the image FFT.

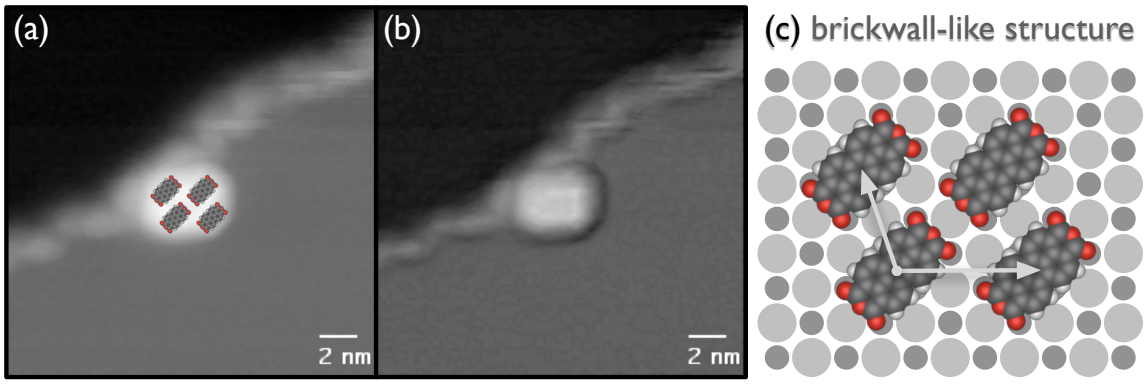

Figure 4.5: Nucleation of PTCDA at a KBr step (a) topograph (b) topograph + edge enhance filter. (Image parameters: Δf=-3.3 Hz, size: 20 nm $\times$ 20 nm, z-scale: 1.1 nm) Molecules can be seen along the step edge as well as an arrangement of four molecules which appears to have a brickwall-like structure (c).

ferent possible structure either co-existing with the primary herringbone-like epitaxy or forming as an initial stage of growth. The proposed structure of these small clusters is shown in figure 4.5c, as derived from processed images (to enhance edge contrasts) and optimizing interaction of the carboxylic anhydride groups with the K^+ ions of the surface. This structure, which can be given in matrix form as

$$\begin{pmatrix} -0.5 & 1.5 \\ 2 & 0 \end{pmatrix}$$

is similar to a "brickwall" structure where the molecules are aligned along the long axis but staggered from row to row. Brickwall structures have been observed for PTCDA on Ag(110) [134] and on KCl [57].

Growth of PTCDA on KBr occurs as island growth in an epitaxial fashion resulting in well ordered crystallites with a nearly bulk structure. A secondary structure was also found as clusters of four molecules which may represent a co-existing structure or an early stage of nucleation. As with C_{60} , islands are found to nucleate at step edges, and diffusion upwards of 1μm is deduced from the large size of terraces which do not nucleate islands.

4.2 PTCDA on NaCl

Growth of PTCDA on NaCl and nanotemplated NaCl was also investigated. Unlike on KBr, a more highly strained and metastable epitaxial monolayer was observed which initiates a dewetting process. At higher coverages, branched morphologies are again observed as a result. On templated NaCl, a co-existance of 3 structures is observed and the optoelectronic properties of each are probed.

4.2.1 The effect of epitaxy in initiating the dewetting process

THE FOLLOWING SECTION IS BASED ON TEXT FROM:

S.A. Burke, W. Ji, J.M. Mativetsky, J.M. Topple, S. Fostner, H.-J. Gao, H. Guo and P. Grütter. Strain Induced Dewetting of a Molecular System: Bimodal Growth of PTCDA on NaCl. *Phys. Rev. Lett.* **100**:186104, 2008.

Introduction

In recent years, there has been great interest in the characterization of organic molecules on solid substrates based on the promise of using such materials as active components in electronic and optoelectronic devices [17, 16]. Structural characterization of these molecular thin films and crystallites has proven to be of importance as the morphology of the film influences the electronic properties to be utilized [110, 19]. As such, the growth mechanisms and resulting morphologies of organic materials on inorganic substrates, including insulators which will be needed to isolate device regions, are of considerable interest in the pursuit of constructing optimized devices.

Both the energetics of a system and kinetic factors during growth determine the morphology of the resulting structures. While a particular growth mode is usually preferred, under certain conditions there can be a transition from layer growth to islands or 3D crystallites by removal of the wetting layer, often termed "dewetting". There have been several recent studies reporting dewetting in molecular systems, for example: perylene on Au and Cu [62], pentacene on Au [64],

phenylthiophene fulgide on glass [65], and C_{60} on alkali halides [55]. Where a metallic substrate has been used, the dewetting process is thought to be a result of strain and a re-orientation of the molecules from the typical co-planar adsorption geometry for monolayer films to a tilted or standing up phase consistent with the bulk crystal structure [62, 64]. While there is some evidence for this molecular scale mechanism for molecules adsorbed on metal surfaces, there has been little study of such dynamical processes and their molecular scale origins on insulating surfaces [55].

The molecule 3,4,9,10-perylene tetracarboxyllic dianhydride (PTCDA) has been studied extensively as a prototypical organic semiconductor material [110]. On many surfaces, crystallites are formed with a structure much like the two polymorphs found in the bulk, termed "α" and "β" [102]. These crystallites are most commonly oriented with the (102) plane parallel to the surface such that the planar PTCDA molecule lies flat on the surface and is arranged in layers of a "herringbone" lattice. Coverages exceeding one monolayer were studied on several alkali halide surfaces, including NaCl, by Schlettwein et al. [135]. In that study, *in situ* optical spectroscopy showed monomer-like emission characteristics during the initial stages of growth, indicating weakly interacting species on the surface, disappearing at $\sim$1ML where a lower energy excitonic peak dominates, indicating the presence of bulk-like crystallites [135]. The authors noted the need for molecular resolution imaging to determine the structures in order to fully understand their observations, however, such studies have not been forthcoming. More recently, PTCDA has been studied on KBr [53] and pit templated KBr [54, 136] with molecular resolution using noncontact-AFM (nc-AFM) to determine the structure of crystallites, and in several cases these molecular resolution images have lead to determination of the epitaxy of molecular systems on insulators [55, 54, 51].

In this paper, we describe the morphology of sub-monolayer coverages of PTCDA on the model insulating substrate NaCl. The use of nc-AFM allows molecular resolution imaging and determination of the detailed structure of the crystallites and monolayer islands observed. Based on these structures and accompanying calculations the molecular scale origin of a dewetting transition is elucidated, resulting in the bimodal growth found. Such bimodal growth with a dewetting transition triggered by increasing coverage is similar to that observed for Au on

$SrTiO_3$(001) [63], a vastly different system.

Experimental details

Single crystal NaCl substrates (Korth Kristalle, Germany) were cleaved in UHV with a base pressure of 3×10^{-8} Pa, and heated for 1hr at $\sim$175°C, yielding (001) surfaces with flat terraces of up to 1.2μm. Submonolayer coverages of PTCDA (Acros Organics 98% purity) were deposited on the room temperature substrates by thermal evaporation at 300°C after outgassing overnight at 200-220°C. Coverages ranging from 0.42ML to 0.85ML were deposited at rates of 0.007-0.009ML/s as measured by a quartz crystal microbalance.

A commercial JEOL JSPM 4500a UHV AFM operated at room temperature was used to study the molecular films by nc-AFM. In this mode, the change in resonance frequency of an oscillating cantilever caused by the tip-sample interaction is used to regulate the distance and create a topographic map as the tip is scanned over the surface. Excitation of the cantilever and measurement of the frequency shift is performed with a NanoSurf easyPLL which also provides constant amplitude feedback. Nanosensors cantilevers (PPP-NCLR) were used, which have typical resonance frequencies of 170kHz and spring constants of 40-50N/m. Typical oscillation amplitudes used were 6-7nm, and typical Q-factors were $\sim$6000.

Morphology and epitaxy

Several sub-monolayer coverages of PTCDA were deposited and characterized by nc-AFM (see fig. 4.6). At coverages of 0.74ML and below, roughly square-shaped monolayer islands with rounded corners showing alignment with <110> directions of the substrate were observed. To confirm that these are indeed monolayer islands, heights were measured with Kelvin probe feedback to compensate for differing electrostatic forces [101] over the PTCDA and NaCl (see section 2.2.3). The height of the islands was found to be 3.4$\pm$0.2Å which corresponds closely to the layer to layer spacing of (102) planes of PTCDA crystals of 3.2Å [17]. At 0.85ML, coexistence of two different types of islands was observed: the same monolayer islands as described for lower coverages and taller islands showing crystallographic edges typical for PTCDA growth on other surfaces such as KBr [53].

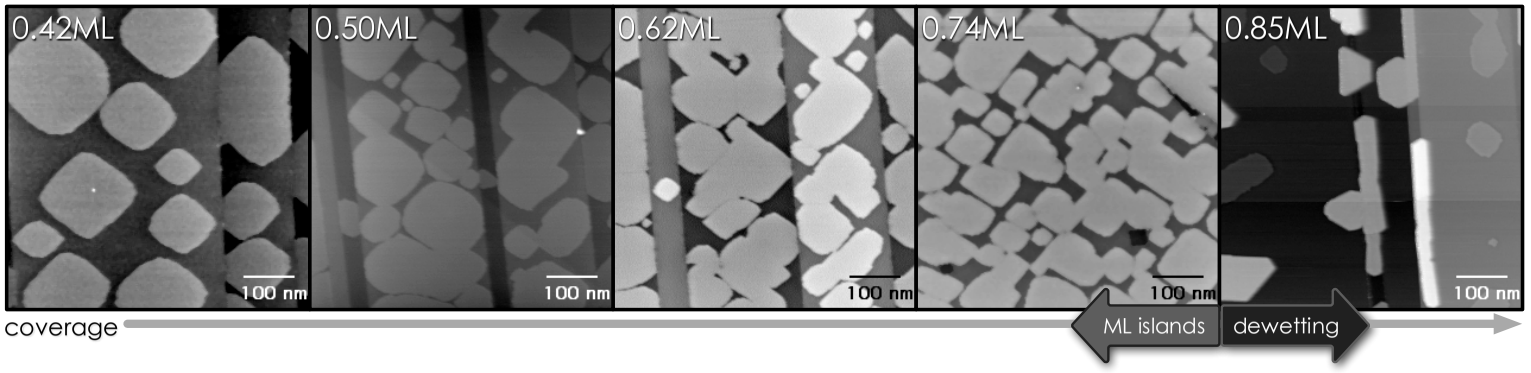

Figure 4.6: Overview images (600×600nm) of different sub-monolayer coverages of PTCDA on NaCl. At 0.74ML and below, only monolayer islands are observed, at 0.85ML, monolayer islands and tall crystalline islands co-exist.

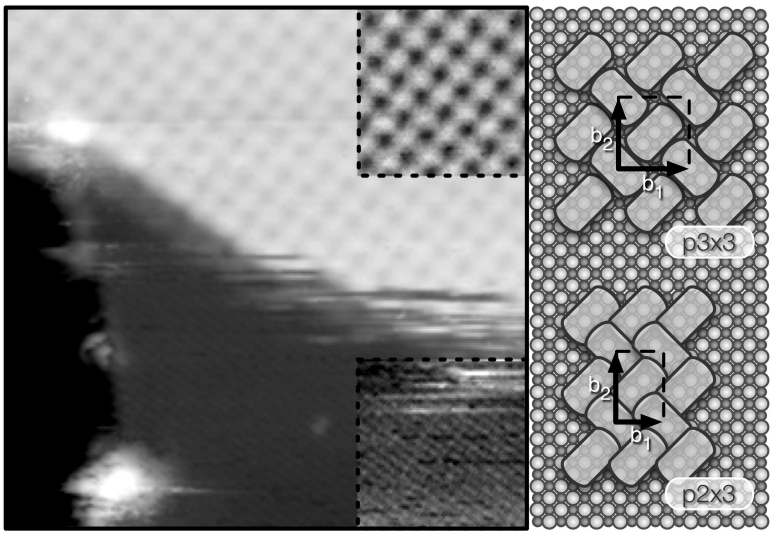

Figure 4.7: Left: nc-AFM topography (raw data) of a monolayer island showing molecular and atomic scale resolution on the overlayer and substrate with insets adjusted for contrast (Δf =-8.7Hz, size: 20 nm $\times$ 20 nm, z-scale=0.55 nm). Right: schematic of proposed p3$\times$3 monolayer epitaxy (top) and proposed p2$\times$3 multilayer interface structure (bottom).

High resolution imaging over the edge of a PTCDA monolayer island (see Fig. 4.7) allows determination of the epitaxial relation of the overlayer by calibration of all measured distances to the known lattice of the substrate. The monolayer islands exhibit a p3$\times$3 epitaxy (shown schematically on the upper right of fig. 4.7) where the center molecule has the opposite orientation to those at the corners of the unit cell, similar to the molecular arrangement of the square phase observed for PTCDA on other surfaces [137, 138, 139]. This p3$\times$3 structure introduces a rather large strain, as compared to a p2$\times$3 structure for example (see table 4.2), which was observed for PTCDA on KBr [54]. While the p3$\times$3 structure clearly forms, and may be allowed in a soft molecular system, it is not readily compatible with the typical herringbone arrangement observed for PTCDA, and one may infer that as multilayer structures form, the molecular arrangement at the surface is altered to accommodate the additional layers.

Table 4.2: Strain, presented as the percent change from the bulk PTCDA lattice parameters of the (102) planes of the α (b_1=1.196nm, b_2=1.991nm) and β (b_1=1.245nm, b_2=1.930nm) [102] crystal structures for p3×3 and p2×3 epitaxial structures on NaCl (a=0.56nm).

	p3×3		p2×3	
	Δb_1	Δb_2	Δb_1	Δb_2
α	40%	-16%	-6%	-16%
β	35%	-13%	-10%	-13%

Stability of structures and dewetting

To investigate the stability of these structures and the effect of the addition of a second layer, molecular mechanics (MM) calculations were carried out[1] using a force field which takes into account both electrostatic and Van der Waals interaction, methods described in [140]. Density functional (DFT) calculations were first performed to confirm that there is no significant contribution to the interaction through electronic hybridization or charge transfer between PTCDA and the NaCl(001) surface (see appendix F taken from supporting information, part 2). Both DFT and MM methods were used to determine the Cl-top site as the stable adsorption site, where the center of the molecule resides over a Cl- ion. In this position, the more negatively charged oxygen groups at the ends of the molecules reside over the Na^+ surface ions as a result of electrostatic interactions. Additionally, both the DFT calculations and MM calculations found molecule substrate distances closely corresponding to the measured height of the monolayer islands: 3.5Å molecule-substrate distance from DFT, and 2.73Å closest and 3.71Å furthest O-Na^+ distance from MM while a layer height of 3.4±0.2Å was determined from experiments. This good agreement between DFT and MM as well as the lack of a significant electronic contribution to the binding allow the use of the MM method which can better model the intermolecular interactions, which are primarily van der Waals in origin, as well as electrostatic interactions, shown to contribute significantly to the molecule-substrate interaction (see appendix F taken from sup-

[1]MM and DFT calculations determining the energetically favourable sites, binding energies, and changes in electronic structure due to interaction with the lattice were performed by Wei Ji of the Beijing National Laboratory for Condensed Matter Physics, Chinese Academy of Sciences in the group of Hong-Jun Gao, while visiting in collaboration with Hong Guo at McGill University.

Table 4.3: Calculated adsorption energies for p2×3 and p3×3 with intermolecular and molecule-substrate contributions.

	$E_{adsorption}$	$E_{molecule-molecule}$	$E_{molecule-substrate}$
p2×3	-30.2 kcal/mol	-13.4 kcal/mol	-16.8 kcal/mol
p3×3	-27.8 kcal/mol	-7.0 kcal/mol	-20.8 kcal/mol

porting information, part 2).

In the MM calculations, both the p3×3, and proposed p2×3 structures were considered. The p2×3 structure was found to be energetically favorable overall. Due to the compression of the lattice, the molecules adopt a small tilt away from the usual coplanar adsorption geometry to accommodate the close packing required for this structure (see fig. 4.8). However, while for the p2×3 structure the intermolecular interactions are comparable to the substrate-molecule interaction, for the p3×3 structure the molecule-substrate interaction dominates (see table 4.3). In forming a monolayer the p3×3 structure maximizes the interaction with the surface, though this structure is metastable.

As the p3×3 structure differs significantly from the bulk PTCDA crystal structures, the addition of a second layer was modeled for both the p3×3 and p2×3 structures by using a 3×6 cell. For both interface structures, several initial second-layer configurations were tested, however, for the p3×3 interface no ordered second layer could be found (see fig. 4.8). This is consistent with the findings of Gustafsson *et al.* that upper layers were not observed on the square phase regions [139]. For the p2×3 interface, the second layer forms a highly ordered structure with lattice parameters very close to those of the α-PTCDA crystal, differing only by 5%, -2% and +0.3% for b_1, b_2, and interlayer spacing respectively. This supports the idea that while a p3×3 monolayer can form initially, the structure is incompatible with a multilayer crystal and thus we anticipate that the interface adapts to accommodate the growth of additional layers. This change in the interface structure would also be accompanied by a change in the interface energy and surface energy of the molecular crystal resulting in the observed dewetting transition.

As the p3×3 structure is extended in one direction, the molecular packing is less dense than in the bulk crystal which has been used for the definition of the

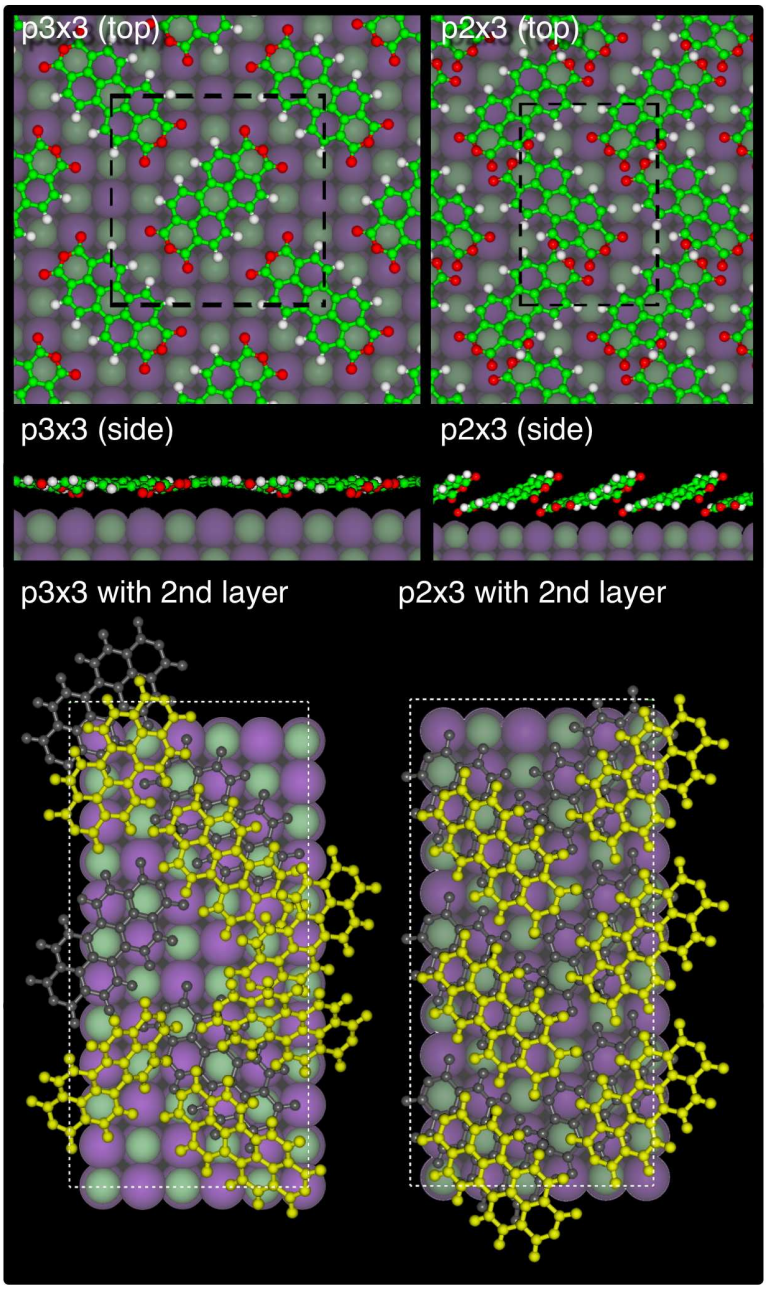

Figure 4.8: Top: Top and side views of p3×3 and p2×3 structures. Bottom: disordered and ordered second layer (yellow/light grey) on a p3×3 (grey) and a p2×3 interface layer, respectively.

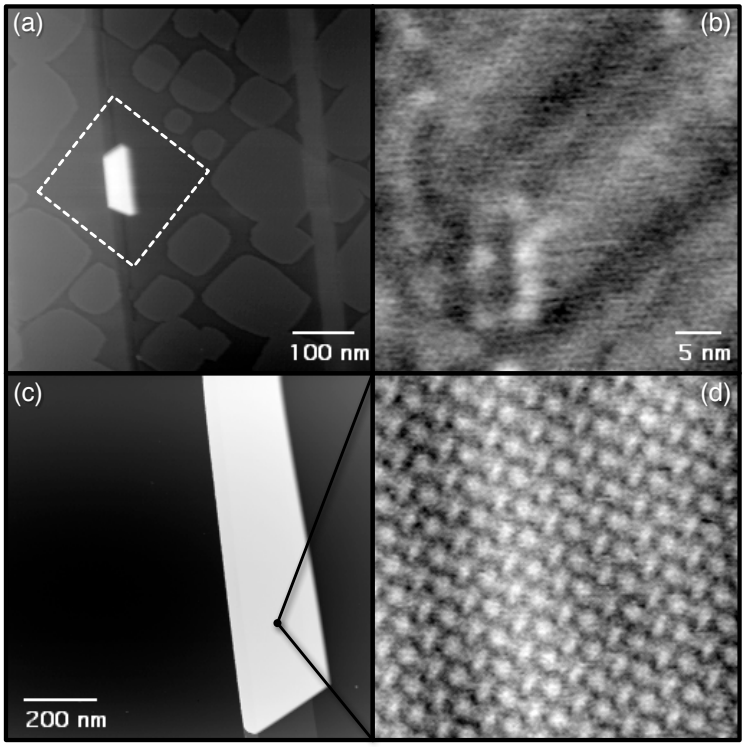

Figure 4.9: (a) A tall crystalline island surrounded by a depletion region (indicated by the dashed box) caused by substrate induced dewetting (Δf =-8.4Hz, z-scale: 3.6nm) and (b) zoom in on top of a tall crystallite showing larger range variations and grain boundaries in addition to the herringbone structure (Δf =-9.8 Hz, size: 40 nm $\times$ 40nm, z-scale: 55 pm). (c) PTCDA island after annealing (Δf =-2.3Hz, z-scale=7nm) and (d) molecular resolution of the herringbone structure observed on top of the annealed island (Δf =-25.5Hz, size: 15nm, z-scale=0.1Å).

coverage in ML. A completely covered surface is expected at 0.84-0.85ML (for α and β respectively) for the p3×3 structure, indicating that such a dewetting transition should occur near this coverage, as is indeed observed. Additionally, the transition from the less dense monolayer epitaxy to a structure resembling the bulk PTCDA crystal structure is consistent with the spectroscopic observations of Schlettwein et al. [135] exhibiting a shift in fluorescence from monomer-like signatures to bulk-like excimeric signatures starting near 1ML.

Substrate morphology also appears to play a role in inducing local dewetting. In regions where the substrate has a high step density or narrow troughs (such as in fig. 4.9a), multilayer crystalline islands are observed in some instances at coverages below the dewetting transition. On top of these tall crystallites the familiar herringbone arrangement with larger scale striped features and dislocation lines or grain boundaries is observed (not shown), indicative of a bulk-like structure under strain. These islands are surrounded by a depletion region, void in monolayer islands of an area closely corresponding to the volume of molecules in the crystallite. For example, the depleted region around the crystalline island in fig. 4.9a represents a volume of $\sim$16,300nm^3 if covered by monolayer islands, while the volume of the crystalline island observed is 15,900nm^3. Such a depletion region further indicates that the crystallites are formed by removal of the monolayer islands rather than two types of islands which grow independently of one another.

Annealing of the 0.74ML coverage, which had predominantly monolayer islands covering the majority of the surface, at 150° for 16 hours resulted in large crystalline islands (shown in fig. 4.9b) sometimes several microns apart. These crystalline islands were found to have heights upwards of 5nm corresponding to 15 or more layers, and were several microns in length in many cases. These crystalline islands had a clear herringbone lattice with a longer range topographic pattern on the top surface (see fig. 4.9b inset) indicating a strained bulk-like structure, similar to that seen on those crystalline islands observed with no annealing. No evidence of the metastable monolayer islands was found after annealing.

Summary of PTCDA dewetting

In summary, we have presented an example of a dewetting transition in a molecular system which is driven by strain, and is accompanied by a change in crystal structure. It is proposed that the observed monolayer islands are metastable and are incompatible with a multilayer structure. Thus, as coverage is increased beyond the first monolayer the interface structure is adapted to accommodate the growth of additional layers triggering a dewetting transition. This is supported by MM calculations which show that while there is no ordered structure possible on the p3×3 interface, the second layer on the more stable p2×3 interface is not only ordered, but similar to the bulk crystal structure for PTCDA. The observation of dewetting in this prototype molecule-insulator system and the determination of the molecular scale origin of the dewetting transition is an important step in understanding key growth processes of such systems.

4.2.2 Analysis of PTCDA island shapes on NaCl: effect of dewetting on morphology

To determine whether the dewetting of PTCDA on NaCl results in similar morphological effects as in C_{60} on alkali halides, a high coverage of PTCDA was also investigated. At a 2ML coverage, quasi dendritic islands appear, exhibiting crystallographic edges expected for PTCDA (see fig. 4.10, right). The observation of dendritic islands is consistent with the observations of Schlettwein *et al.* [135] where *ex situ* AFM observation of 1-2ML of PTCDA deposited onto NaCl at elevated temperature (90-110° C) revealed large dendritic islands. The authors also speculate that the surface between islands is covered with a monolayer of PTCDA both from the observation of pinholes in the AFM data approximately corresponding to the height of a PTCDA layer and from spectroscopic observations showing a monomer-like emission for up to 1ML coverage. Here, monolayer islands in the space between multilayer crystallites are clearly evident from the *in situ* nc-AFM topographs, even in this high coverage regime.

As with C_{60} on KBr and NaCl (see section 3.3), quantitative analysis of islands shapes can be applied by measuring the island areas and perimeters. A

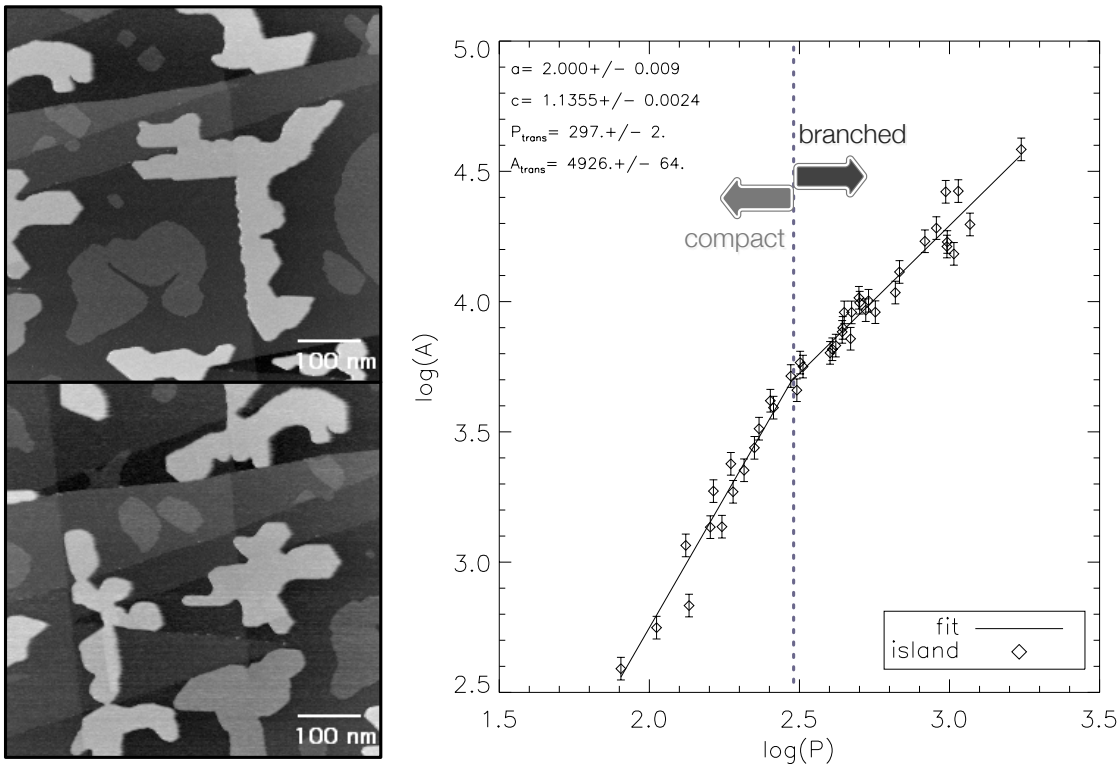

Figure 4.10: Morphology of 2ML PTCDA on NaCl: topographic images (600nm×600nm) of branched island and monolayer islands (left) and PAR plot showing transition from compact to branched (right).

perimeter-area relation (PAR) plot, or dimensionality plot, shows a transition from a compact regime (PAR slope of 2) at smaller island sizes to a branched morphology beginning at a critical size. This behaviour is strikingly similar to the previous case of C_{60} on alkali halides. For comparison, the fractal dimension of the branched region is $D' = 1.75 \pm 0.06$, differing significantly from the fractal dimension of the branched C_{60} islands which gave $D' = 2.2 \pm 0.2$.

The continued presence of monolayer islands suggests a possible mechanism for the formation of quasi-dendritic structures in this case. At coverages leading up to the first dewetting transition, monolayer islands dominate and fill the available surface. As the monolayer islands dewet into multilayer crystallites, fresh areas of the substrate are exposed and become available for growth. If growth proceeds, attachment to the multilayer crystalline can occur, as well as growth of monolayer islands on the freshly exposed substrate. These monolayer islands can again grow to fill the surface causing subsequent dewetting events. This would lead to the somewhat haphazard addition to multilayer crystallites with each dewetting event. Similar to the case of C_{60} , it would then appear that while there is sufficient diffusion to reach local equilibrium and form faceted edges, there is *not* sufficient diffusion along island edges to rearrange these islands to form compact and defect free structures.

Shape factor analysis (see section 3.3, equation 3.2) can also be applied to the growth of PTCDA on NaCl. In figure 4.11 the shape factor distributions of four different coverages are plotted. At low coverage, where the rounded diamond shape monolayer islands dominate, the majority of islands exhibit a shape factor close to 1 ($\sim$0.9). With increasing coverage, the influence of the trapezoidally shaped multilayer crystallites becomes evident with a secondary peak appearing at shape factors between 0.5 and 0.8, the spread in values being a result of variation in the aspect ratio of the crystallites. At 2ML, the peak corresponding to monolayer islands is reduced, and a broad peak centred around 0.5 appears. This broad peak corresponds to the wide-branched dendritic structures observed at this higher coverage. While the shape factor does not easily distinguish between the two populations of islands due variability in the aspect ratio, and the fractal islands at higher coverage also give a wide variation in shape factor, the evolution from rounded to compact to branched islands with increasing coverage is evident.

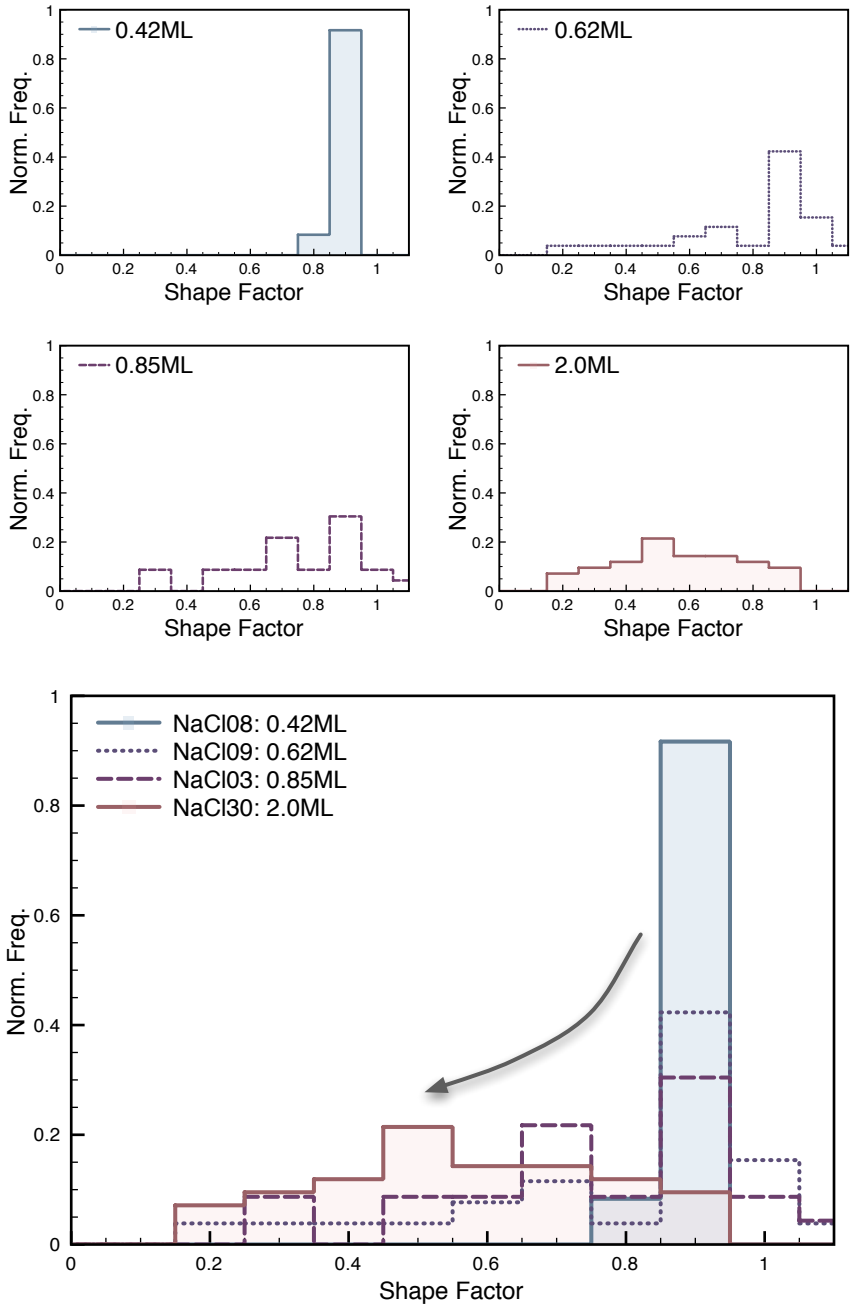

Figure 4.11: Histogram of shape factors showing a progression of S.F. with increasing coverage. The dominance of the rounded diamond shape islands (S.F.∼0.9) at low coverage moves toward a broader distribution of shape factors with lower values with increasing coverage.

Similar to that observed for C_{60} on alkali halides, the dewetting process has a strong influence on morphology, again resulting in fractal-like growth. The evolution of morphology as a function of coverage presents an interesting challenge for the growth of well defined films but also a possible method for controlling morphology if well understood.

4.3 Structure dependence of functional properties: PTCDA on nanotemplated NaCl

THE FOLLOWING SECTION IS BASED ON TEXT FROM:

S.A. Burke, J.M. LeDue, J.M. Topple, S. Fostner, P. Grütter. Relating the functional properties of an organic semiconductor to molecular structure by nc-AFM. Submitted to *Advanced Materials*.

4.3.1 Introduction

It is well known in the field of thin-film organic electronics that film morphology plays a critical role in device properties [17, 19]. In the related field of single molecule electronics, the local environment, ie. nanoscale structure, is crucial in determining possible device related properties such as conductance characteristics [13]. While this has sparked significant study in the structure of molecular deposits on solid surfaces [110, 32], it is an understanding of the connection between local structure variations and functional properties which are needed to control and optimize materials for device purposes. Moreover, despite the necessary use of insulating regions in device applications, there has been little study of structural influence on properties of molecules on insulating surfaces due to a lack of available tools. We combine the high spatial resolution of noncontact atomic force microscopy (nc-AFM) with local electrostatic characterization by Kelvin Probe Force microscopy (KPFM) under laser illumination at multiple wavelengths. This allows a determination of how the observed variability in molecular scale arrangements influences the optoelectronic properties of this prototypical organic semiconduc-

tor 3,4,9,10-perylene tetracarboxylic dianhydride (PTCDA) on a nanostructured insulator.

The electrostatic properties and surface photovoltage of various surfaces have been studied using both amplitude modulation-KPFM (AM-KPFM) and frequency modulation-KPFM (FM-KPFM) in ultra-high vacuum (UHV) and in air, including both inorganic [141, 142] and organic [143, 144, 145] model photovoltaic materials. While these studies have provided considerable insight into differences in work function and generation of charges, there has been little focus on connecting the electrostatic properties measured with local structure of the material. The use of nc-AFM in UHV allows the determination of molecular scale structures (epitaxies) of ordered deposits, even on insulating substrates [56, 55, 51, 54, 60]. Similarly, FM-KPFM and local electrostatic force spectroscopy can provide quantitatively accurate measurements of the tip-sample contact potential difference at scales approaching the tip diameter (typically tens of nm). In this work, detailed determination of the molecular scale structure is combined with a local measurement of optical excitation by using FM-KPFM and local electrostatic force spectroscopy to examine the influence of different molecular scale structures of a model organic system on its opto-electronic properties. As this technique does not require that the sample be conducting, in contrast to conducting AFM and scanning tunnelling microscopy, even thick (bulk) insulating substrates may be used, though this complicates quantitative interpretation. The addition of illumination at multiple wavelengths allows excited molecular states to be probed, thus providing a local signature of excitation which can be connected to local structure.

The organic semiconductor (PTCDA) was selected due to its well known ordered crystalline structure [102], easily accessible optical absorption spectrum [15], and the ability to trap molecular crystallites in single monolayer pits in alkali halides [54, 50, 136]. Previous study of PTCDA on NaCl has shown a coexistence of monolayer structures with multilayer crystallites [56]. Using nanoscale pits in the NaCl to template the growth, these structures are observed along with confined molecular monolayers found in the pits.

4.3.2 Experimental details

Single crystal NaCl (Korth Kristalle GmbH, Germany) is cleaved in situ in ultra high vacuum (base pressure 10^{-8}Pa) to reveal (001) surfaces with atomically flat terraces of up to 1.2μm. Pits are made in the surface by exposing the sample to charge from an electron beam evaporator (operated below the deposition power for the target material) as described in [105]. The charge was generated using a tantalum target with the evaporator operated at 24W, below the evaporation threshold. The sample was heated to 250° C and exposed to the charge source for 104min producing a total charge dose of $\sim$1.31μC/cm^2. This resulted in removal of 9% of the surface and pits of average area of 120nm^2 with densities of 550-1000 pits/μm^2. PTCDA (Alfa Aesar, 98%) molecules are deposited by thermal evaporation at 300°C after outgassing overnight at 200-220°C. Coverages ranging from 0.3ML-0.5ML at rates of 0.006-0.013ML/s were deposited as measured by a quartz crystal microbalance (Inficon).

The sample surface is investigated by nc-AFM, using a JEOL JSPM 4500a, at each stage of preparation. The change in frequency of an oscillating cantilever due to tip-sample interaction is measured, and a topography is generated by recording the z variation required to maintain constant frequency shift [100]. A Nanosurf easyPLL is used to drive the cantilever oscillation, monitor frequency shift and maintain constant amplitude. Highly doped Nanosensors (NCLR) Si cantilevers are used with the native oxide intact. Typical cantilevers have a resonance frequency of 170kHz, spring constant of 40N/m, tip radii of <7nm, measured Q-factor in UHV of $\sim$10,000, and oscillation amplitudes of 6-7nm are used.

Among the interaction forces detected by the nc-AFM method, is the electrostatic force which contains information about the work function of the sample through the contact potential difference [80, 100]. This information can be accessed by performing local spectroscopy (Δf vs. V), or through an imaging mode known as KPFM. In KPFM, an oscillating bias is added to a DC offset which generates a response of the frequency shift at the bias modulation frequency. This response at the modulation frequency is measured with lock-in techniques (Princton Applied Research, 5110 Lock-in amplifier) and an additional feedback circuit (JEOL SKPM control module) is employed to adjust the DC bias offset in order to null the electrostatic force, ie. the DC bias is adjusted to compensate for the CPD. In

this way the DC bias can be recorded to generate a map of the CPD of a heterogeneous sample. Typical parameters used for this system were f_{mod}=1kHz, A_{mod}=1-1.5V$_{rms}$, τ=1.0ms, V_{sens}=50mV (corresponding to Δf =0.9Hz), with a scan speed of 6.67ms/point, ensuring all measurements are sufficiently separated in frequency.

Illumination of the sample was performed by directing laser light through the front glass port of the instrument at an angle of $\sim 10^{\circ}$ (see fig. 4.12). A diode-pumped solid state laser (Melles-Griot 85-BCA-015) was used free-beam for illumination at 473nm by mounting the laser directly on the air-table of the AFM. At an output power of 7.5mW and spot size of 0.6mm, this results in a power density of 1mW/mm^2. Illumination at 488nm and 514nm was achieved using a tuneable Argon-ion laser (Melles-Griot 35-LAP-431). Due to the size of the laser and to avoid coupling vibrations from the cooling fan to the AFM, the laser was fiber coupled and only the fiber end with a collimator were mounted on the table. The collimated beam size was 2mm with output power and power density of 26.6mW or 0.4mW/mm^2 at 488nm and 25.1mW or 0.3mW/mm^2 at 514nm. All power densities are well below bleaching thresholds as determined from *ex situ* fluorescence measurements. The same polarization was used for both lasers, aligned along the sample surface (no component normal to the surface).

4.3.3 Morphology of pit templated growth

The pits in the NaCl (001) surface which are used to template the growth of the molecular deposit were created by charge irradiation at elevated temperature, and result in well defined rectangular holes in the surface one atomic layer deep. The parameters used result in pits with edge lengths of 7-15nm, or an average area of 90-160nm^2 (some sample to sample variability), with 9% of the surface removed. Similar to that which is observed for pits in KBr, some PTCDA islands are templated by the pits [54, 146], while some islands grow in the same manner as on the untemplated surface [56]. This results in three types of structures: multilayer crystallites, "free" monolayer islands, and confined monolayer islands in pits. Unlike the case of PTCDA on nanotemplated KBr where only multilayer islands were found in pits [54], these were only rarely observed on NaCl (as in fig. 4.13b), while the vast majority were filled with only a single layer.

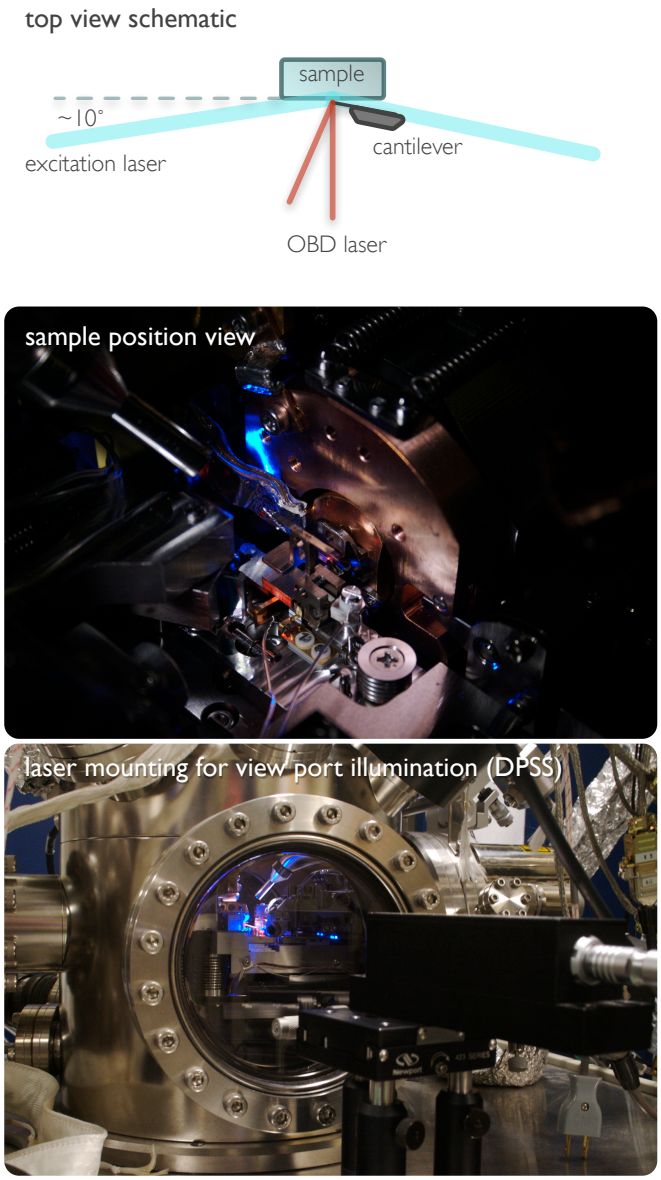

Figure 4.12: Schematic (top) and photographs (middle and bottom) of experimental apparatus for sample illumination through front viewport. The sample surface is illuminated at a grazing incidence ($\sim$ 10°) which allows the light to illuminated the majority of the sample surface without significant shadowing by the cantilever, chip and holder or other obstructions of the stage. Also, the PSD used for the optical beam deflection does not receive significant scattered light from the illumination in this configuration as the total signal from all quadrants (SUM) differs by less than 1% with illumination. For convenience, the DPSS laser was mounted directly on the vibration isolation table using magnetic post holders (see bottom photo), while the Ar-ion laser was fiber coupled and the fiber end and collimator only were placed on the table to reduce vibrations.

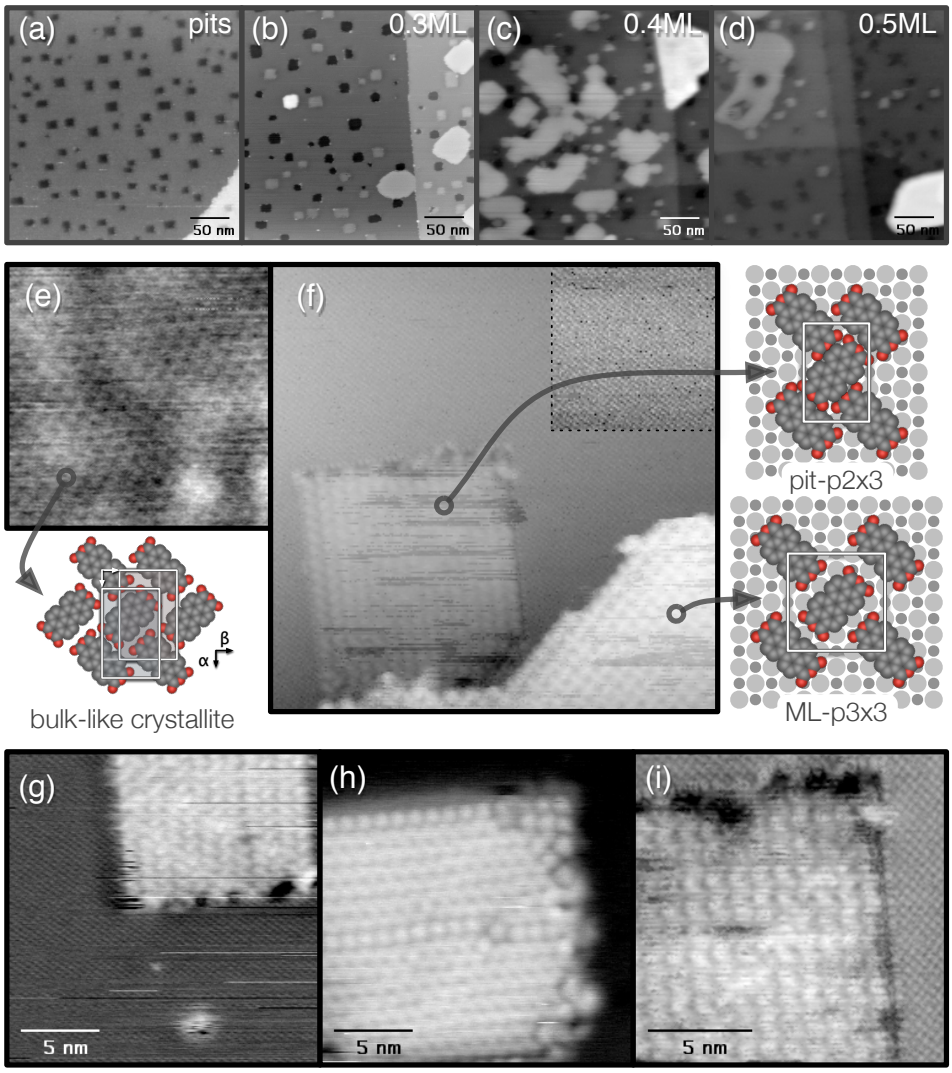

Figure 4.13: Top: (a-d) Overview of templated PTCDA growth from pits without molecules to 0.5ML. 3 types of structures are observed for all coverages: crystallites, monolayer islands, and confined monolayer islands. Middle: Molecular scale structures with schematics of 3 island types (e) crystallite with bulk-like herringbone structure Δf=11.1Hz, size: 15nm $\times$ 15nm, z-scale: 101pm), (f) monolayer trapped in pit with p2$\times$3 structure and a free monolayer with p3$\times$3 structure with contrast enhanced inset to show NaCl lattice (Δf=-9.3, size: 35nm $\times$ 35nm, z-scale: 520pm). Bottom: (g-i) examples of some different defects in monolayers confined in pits.

As the coverage is increased, the dominant type of structure evolves. At 0.3ML, primarily monolayer structures are observed, both in the pits and on the surrounding substrate. Increasing the coverage to 0.4ML, many more multilayer crystallites are observed, with a mixture of all three structures. Increasing further to 0.5ML, more larger multilayer crystallites are observed often spaced further apart, and much less of the surrounding surface is covered with monolayer islands, though confined monolayers are still quite prevalent. Compared to the untemplated growth which exhibits a dewetting transition at 0.85ML, the evolution from monolayer islands to multilayer crystallites appears to be shifted to lower coverage by the presence of the pits. This is consistant with the finding that highly stepped areas of the surface induce local dewetting (see section 4.2.1 and [56]).

Using the high resolution imaging capabilities of nc-AFM, we can identify the molecular arrangement of each type of structure. The multilayer crystallites exhibit a bulk-like herringbone structure (see fig 4.13e), with evidence of grain boundaries and buckling of the lattice (long range periodicity). The confined and free monolayer structures have different molecular arrangements (see fig 4.13f) as observed by obtaining simultaneous molecular and ionic contrast on the overlayer and substrate, respectively. The "free" monolayers have the p3×3 epitaxy observed previously for untemplated growth (see section 4.2.1 and [56]), whereas the confined monolayers exhibit a herringbone-like structure with a p2×3 registry, which has been proposed as the interfacial structure for PTCDA crystallites on NaCl [56]. Due to the strained nature of this structure and the requirement imposed on the molecular crystal to fit in the confined area of the pit, a variety of defects are observed in the confined p2×3 monolayers [examples shown in fig 4.13(g-i)].

4.3.4 Measurement of functional properties and correlating with structure

The electrostatic properties of each of these three structures differs as measured by KPFM and local spectroscopy (see fig. 4.14). While KPFM provides a map of the local contact potential difference (CPD) even for the thick insulating substrate used, a more reliable measure of the CPD was obtained through Δf vs. V

spectroscopy using a parabolic fit to locate the minimum resulting in an error on the CPD determination of 0.01V. Most notably, the p3×3 monolayer structure exhibits a significantly lower CPD in the dark state compared to both the NaCl as well as the two herringbone-like structures, indicating a lower work function. The confined monolayers also show a slight negative shift of the CPD compared to the crystallites. While differences in the effective CPD can be readily measured, the applied biases are not necessarily representative of the voltage between the tip apex and the sample surface due to the capacitive voltage dropped across the large (3mm thick) dielectric substrate used in this study. As such, care must be taken to account for the full geometry of the capacitive system involved, ie. where the biases are applied, the sample geometry and dielectric properties, and the position of the tip and cantilever beam relative to the applied biases, in order to make quantitative comparisons between measurements from different instruments [147, 148]. While great effort has been made to model the effect of tip geometry on resolution limits and accuracy of CPD measurements and KPFM [80, 149, 150, 151], previous intepretation for molecular and insulating thin films assumes metallic-like behaviour [59, 151]. As the dielectric properties of a thick insulating sample will clearly influence the quantitative interpretation of the CPD values here, a more complete theoretical framework for the interpretation of such data is needed. As such, due to the complex geometry of our apparatus, these effects are not considered and as such only the direction and relative magnitudes of CPD shifts are considered.

Illumination of the sample provides further indication of electronic differences between the three structures. Molecules which absorb light from the laser illumination will be in an excited state effectively lowering the work function and shifting the CPD (for this configuration, to more negative values). Three excitation wavelengths were used: 473nm, 488nm, and 514nm, all of which lie within the absorption spectrum of PTCDA in solution and thin-films (see fig 4.15a). For all three wavelengths there is a slight upward shift of the CPD over the NaCl substrate which is likely a result of a small surface photovoltage excited in the Si tip. The PTCDA crystallites are the only feature which show a consistent and significant shift for all three excitation wavelengths. Given that these have a bulk-like structure we expect the behaviour to be similar to PTCDA thin-films which show

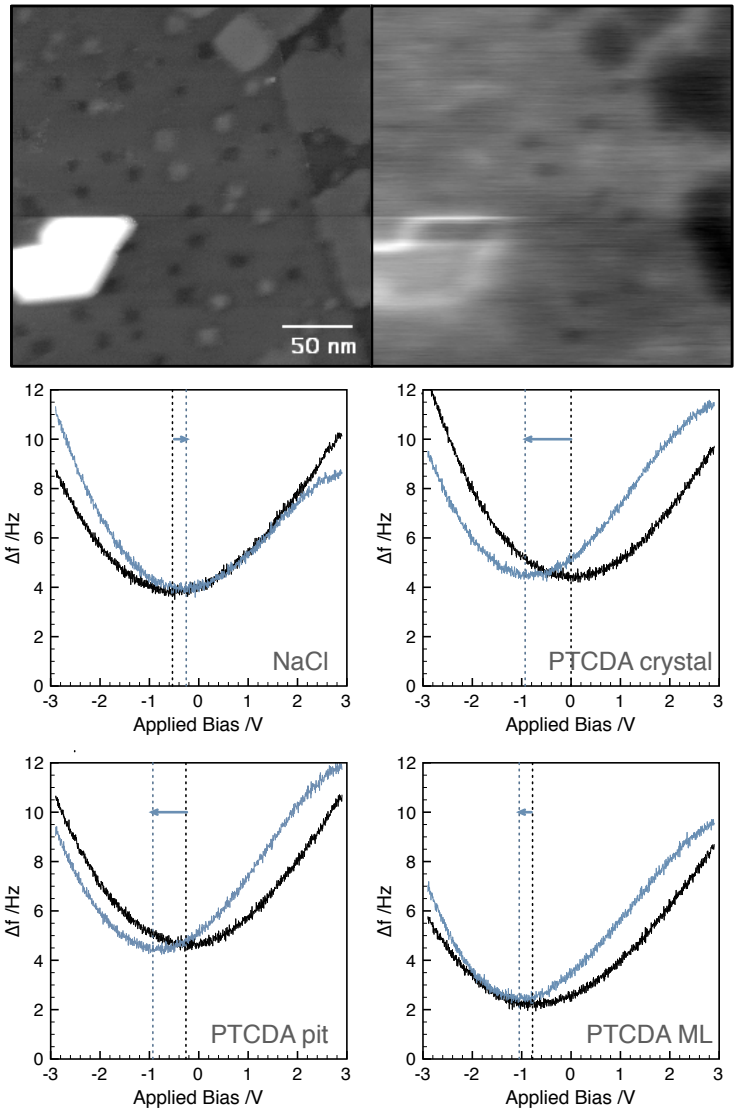

Figure 4.14: Topography and KPFM image of area with all three structures showing difference in CPD of each without illumination (Δf=-6.9Hz, f_{mod}=998Hz, V_{mod}=1.4V_{rms}). Δf vs. V spectroscopy for each site shown without illumination (black) and with 488nm (blue).

significant absorption for all three of these wavelengths.

The trapped monolayer structures show a similar trend with wavelength to the bulk-like crystallites, though much reduced in magnitude, and with no significant shift with illumination at 473nm. The small size of the pits compared to the tip radius may somewhat influence the measurement of the CPD by averaging the pit structure with the surrounding NaCl substrate effectively reducing the observed shift [80]. Also, as the structure is only a single layer, electronic properties of the molecules will be more strongly influenced by the presence of the substrate, and the tightly packed nature of the structure may distort the molecules influencing orbital energy levels [124] resulting in an alteration of the absorption spectrum. As the charge transfer states are not probed at these wavelengths, the lack of such extended states in the confined structure should not effect the measurement, though the effect of confinement on these states is a subject for future study. Interestingly, the statistical variation of the CPD measured for different pit structures is significantly larger than for the other structures. The variety of defects observed in the confined monolayers [see fig. 4.13(g-i)] are expected to influence the electronic properties resulting in a larger variation in the measured electronic properties than for well ordered monolayers or crystallites. Further study correlating specific types of defects with variations in the CPD may be of future interest in understanding the influence of defects on functional properties.

The p3×3 monolayer structure does not show any significant photoinduced shift except at 514nm. The extended nature of the p3×3 structure increases the intermolecular distance, thus reducing intermolecular interactions which are expected to influence molecular orbital energies [152]. The lack of a shift except at 514nm is indicative of a monomer-like species, ie. the molecules are only weakly interacting. Schlettwein et al. [135] observed a monomer-like signature in luminescence during the early stages of PTCDA thin film growth on NaCl where this structure has been observed to dominate [56]. Control over the intermolecular spacing by judicious selection of substrate and the use of templating strategies could be utilized to achieve desired functional properties.

While the interpretation of the photoinduced CPD shift as representing electronic excitation may be over-simplified, to fully understand the represented processes requires significant modelling effort on multiple scales. The CPD shift also

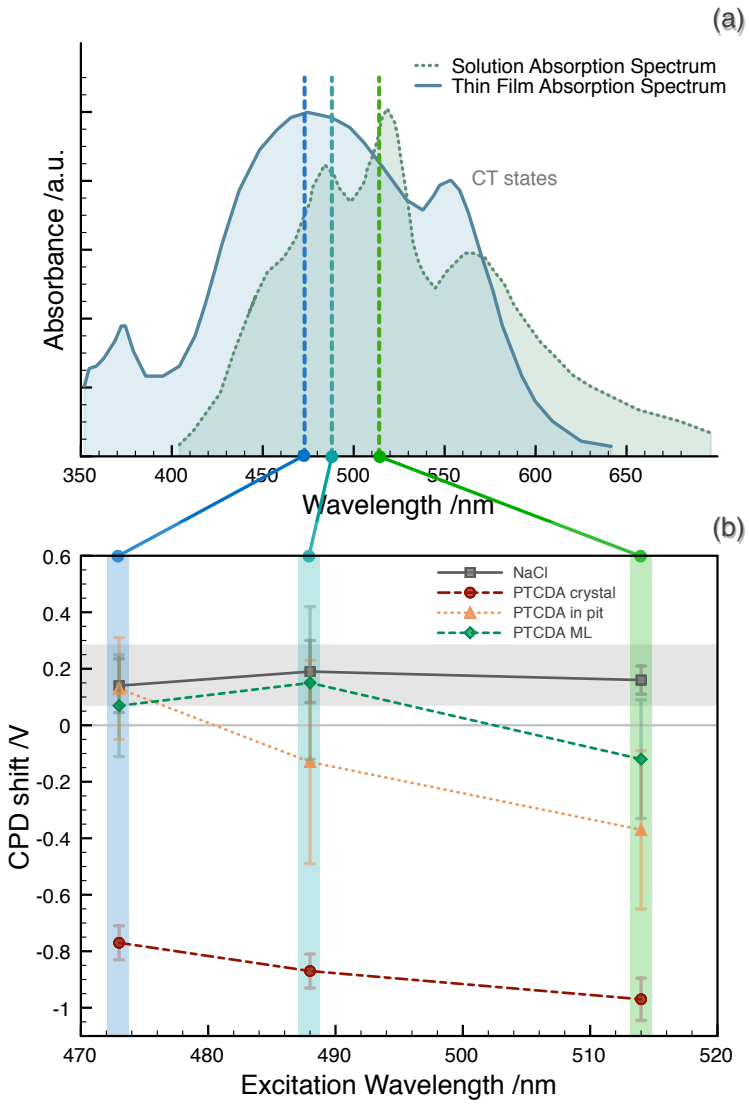

Figure 4.15: (a) Thin-film and solution absorption spectra reproduced from Forrest [15] (see reference for detailed identification of states represented in absorption spectra) showing the three excitation wavelengths used, and (b) mean photoinduced CPD shift as a function of wavelength for each site, error bars represent the standard deviation of measured CPD values at different locations, individual measurements carry an error of ∼0.01V.

likely includes contributions by exciton/charge generation, and the electronic levels are expected to be modified by vibrational levels of the molecules as well as interactions with neighbouring molecules and the substrate, as seen in a recent experimental study on a similar system [57]. Additionally, modelling of the substrate, particularly for monolayer films, need be included to understand the effects of substrate interactions, even for insulating surfaces, on electronic states [124]. To our knowledge, no theoretical framework currently in use can account for all of these effects, though advances are being made in the individual areas of electon-vibrational coupling [153, 154, 155, 156], substrate effects [124, 152], and charge generation and movement in molecular crystals [157].

4.3.5 Summary

In summary, nc-AFM has been used to determine the molecular arrangement of three types of structures of an organic semiconductor on a nanotemplated insulator and locally probe the optoelectronic response of each in order to correlate structural detail with functional properties. The wavelength dependant photoinduced shift of the measured CPD differs over each of the PTCDA structures, revealing that herringbone structures show bulk-like characteristics while the extended, and therefore more weakly interacting, p3$\times$3 monolayer exhibits behaviour more consistent with monomer-like species. By understanding the formation and influence of different molecular arrangements, the desired properties of an organic material could be tuned by simple selection of appropriate substrate or templating strategies. Our successful characterization of this oft-studied opto-electronically active molecule illustrates that nc-AFM is poised to unravel the connection between nanoscale structure and electronic properties, applicable even to insulating surfaces, which is of critical importance to future organic based devices.

4.4 Summary of PTCDA on alkali halides

Growth and epitaxy of PTCDA has been investigated for the alkali halides, KBr and NaCl. For KBr, an epitaxial structure compatible with multilayer growth is

proposed leading to immediate islanding. For NaCl, a strained metastable epitaxial layer was observed which is *not* compatible with additional layers leading to a dewetting transition. The additional dewetting events occurring with increasing coverage may lead to the branched structures reminicient of those formed by dewetting of C_{60} on alkali halides.

Characterization of pit templated growth, both in terms of structure and optoelectronic properties exemplify the influence of molecular scale structure on functional properties. The finding that three co-existing structures produce three different opto-electrostatic responses indicates the importance of understanding and controlling molecular scale arrangements to acheive the desired properties for a device.

5

Other molecules

5.1 PTCDI on KBr and NaCl

In addition to PTCDA, a wide variety of perylene derivatives can be synthesized, primarily in use as commercial dyes [135, 158]. This customizability combined with the highly conjugated nature of the perylene core has made these molecules of particular interest for single molecule and organic electronics and optoelectronics. A large proportion of perylene derivatives are based on the functionalization of the imide groups (-NH bewteen two acyl groups) of PTCDI (shown with PTCDA in fig. 5.1).

From the perspective of investigating growth, a comparison of the behaviour of PTCDI with PTCDA provides an interesting case study of how a small change in the chemical structure or composition can influence growth behaviour. An understanding of this influence will be significant for the use of customized molecules containing functional groups to be engineered to give specific functional properties, but which will also influence growth.

In the case of PTCDI, the imide groups at the ends of the perylene core interact differently than the carboxylic anhydride groups of PTCDA. While the charge distribution is similar, the -NH favours the formation of hydrogen bonds with the -CO acyl groups of the adjacent molecules leading to an end-to-end arrangement (see fig. 5.1) in the bulk crystal [158, 159] as well as on several surfaces [158, 160, 161, 138]. This different intermolecular bonding motif also leads to different island morphologies, but overall similar behaviour on KBr and NaCl, when compared to PTCDA, as is discussed in the following sections.

To compare the bulk monoclinic crystal lattice to the layered structures observed on KBr and NaCl, the lattice constants within the $(10\bar{2})$ plane have been

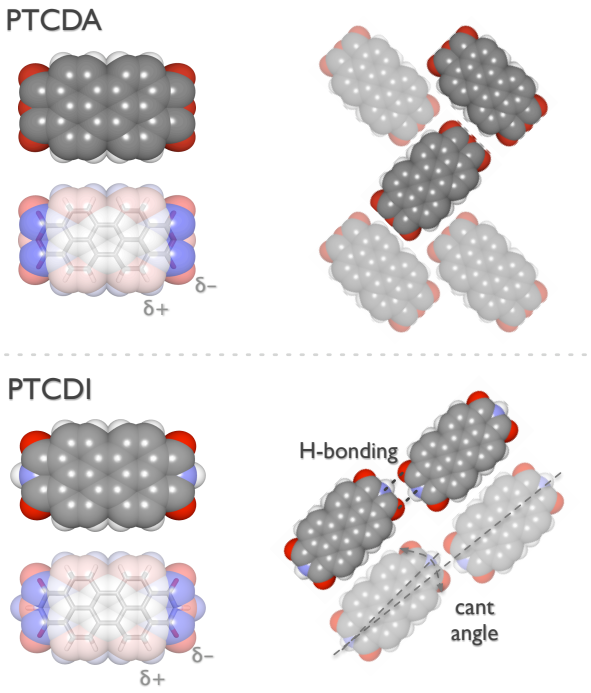

Figure 5.1: PTCDA and PTCDI spacefill models, atomic partial charges (generated using BALLview [70]) and intermolecular bonding motifs. In PTCDA crystals, a herringbone motif is adopted, whereas in PTCDI, the hydrogen bonding between the -NH and -C=O of adjacent molecules dominates the intermolecular interaction resulting in rows of molecules aligned end-to-end. The axis of PTCDI molecules is often rotated with respect to these rows, and the molecules are said to be "canted". [138]

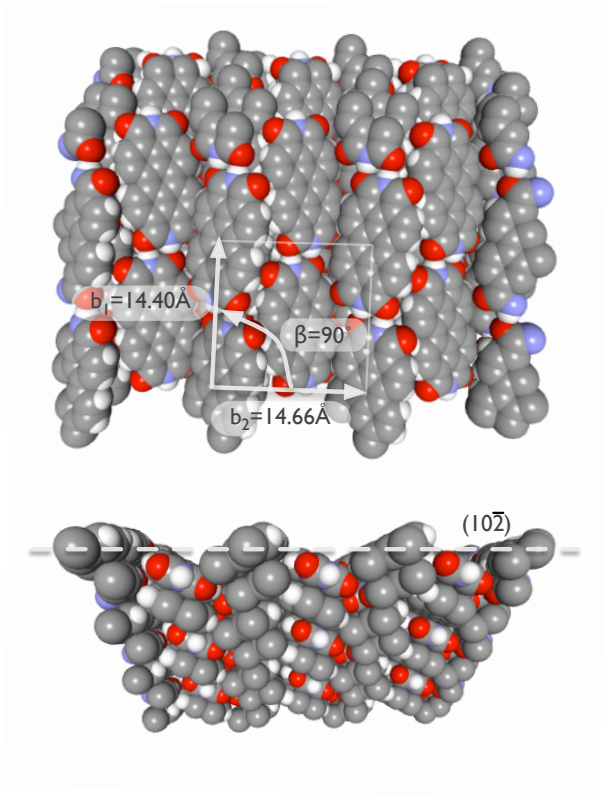

Figure 5.2: Bulk PTCDI crystal with $(10\bar{2})$ termination showing in-plane lattice parameters of b_1=14.66Å, b_2=14.40Å and $\beta = 90.0°$ for comparison with adsorbed layers. Rendered from Tojo *et al.* [159] crystallographic data file using VESTA [71] and BALLview [70].

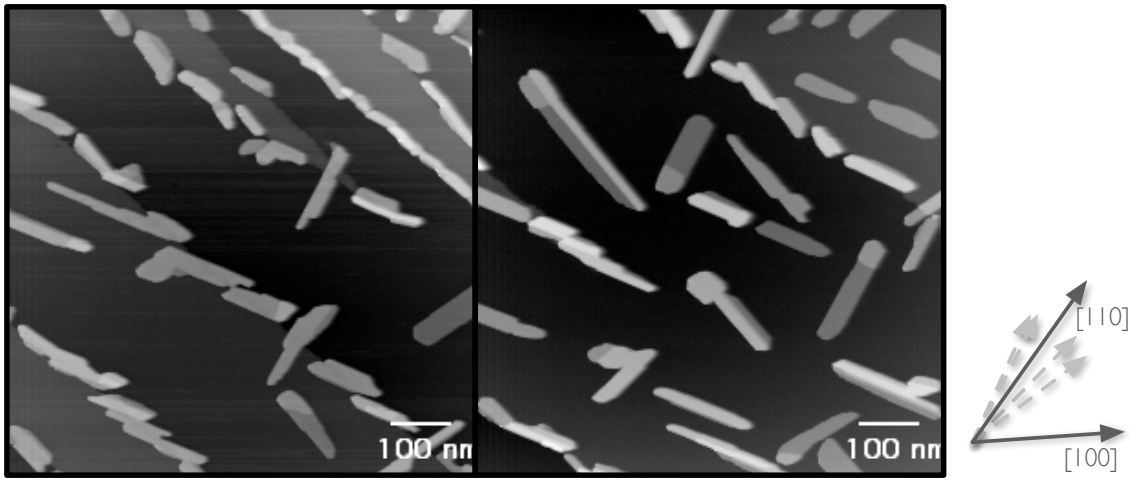

Figure 5.3: PTCDI forms needle-like islands on KBr angled slightly away from the <110> directions of the substrate. No single layer structures are observed.

determined using crystallographic data deposited with the Cambridge Crystallographic Data Center [159]. This plane was selected such that both orientations of the planar molecule lie close to flat on the surface (as shown in the lower panel of fig. 5.2), as opposed to the $(\bar{1}2\bar{1})$ plane considered by Guillermet *et al.* which follows the planar alignment of one orientation of PTCDI, but is nearly edge on for adjacent molecules. The lattice constants in this plane are: b_1=14.40Å parallel to rows of PTCDI and b_2=14.66Å perpendicular to rows of PTCDI with an angle between of $\beta = 90°$. As will be described in the following sections, these lattice constants from the $(10\bar{2})$ plane agree well with those measured on PTCDI crystallites deposited on KBr and NaCl.

5.1.1 PTCDI on KBr

PTCDI was deposited onto a room temperature, freshly prepared KBr surface at $\sim 300°$ C to give a coverage of 1.6Å, or ∼0.5ML, at a rate of 0.019Å/s (∼0.006ML/s). The molecular powder was outgassed overnight at ∼200° C to reduce volatile impurities.

Imaging of the deposited PTCDI revealed long needle-like crystallites ori-

ented at a range of small angles away from the <110> directions of the substrate (see fig. 5.3). These needle-like crystals are somewhat similar to the "molecular wires" observed for di-methyl-PTCDI on KBr [162], but with less well defined orientation and a lower length:width aspect ratio. The islands are several layers (two or more) high even at submonolayer coverage and often have incomplete upper layers. As no single layer regions are observed, it is assumed that the growth proceeds as pure island (or Volmer-Webber) growth with no dewetting processes under the conditions used. Also, as with PTCDA and C_{60} , the islands are observed predominantly at step edges, indicating large diffusion lengths on flat terraces.

High resolution images reveal a molecular arrangement consistent with the expected hydrogen bonding motif described above for PTCDI. Images acquired on top of an island show what appear to be rows of molecules oriented end-to-end with a superstructure of stripes with a spacing of 2.7±0.2 nm at an angle of ∼28° ±2° with respect to these rows (see fig. 5.4c). This superstructure, which was consistently observed over many crystallites even when molecular resolution was not achieved, may be a result of strain in the crystallites or may be due to coincidence with the underlying substrate.

The lattice constants of the PTCDI crystallites were determined from high resolution images over the edge of an island resolving both the molecular structure of the island and the ionic lattice of the KBr substrate (see fig. 5.4b). Correction of the molecular lattice measurements to the known lattice of the KBr substrate yielded lattice parameters of $b_1 = 14.3 \pm 0.2$Å, $b_2 = 15.1 \pm 0.3$Å, $\beta = 92 \pm 1°$, and $\theta = 54 \pm 1°$, where β is the angle between b_1 and b_2, and θ is the rotation of b_1 with respect to the substrate lattice. Comparing to the lattice constants determined for the $(10\bar{2})$ plane of the bulk PTCDI crystal of b_1=14.40Å, b_2=14.66Å and $\beta = 90°$ there is a slight extension (3%) perpendicular to the rows, but a generally bulk-like structure corresponding to this plane parallel to the surface. Based on these lattice constants, a unique epitaxial cell could not be ascribed, however a possible structure (taken as the closest lowest fraction within error) with a matrix of:

$$\begin{pmatrix} 1.27 \pm 0.03 & 1.75 \pm 0.03 \\ 1.90 \pm 0.05 & 1.28 \pm 0.05 \end{pmatrix} \sim \begin{pmatrix} 5/4 & 7/4 \\ 15/8 \sim 2 & 5/4 \end{pmatrix}$$

is shown schematically in figure 5.4a, along with a schematic of the expected

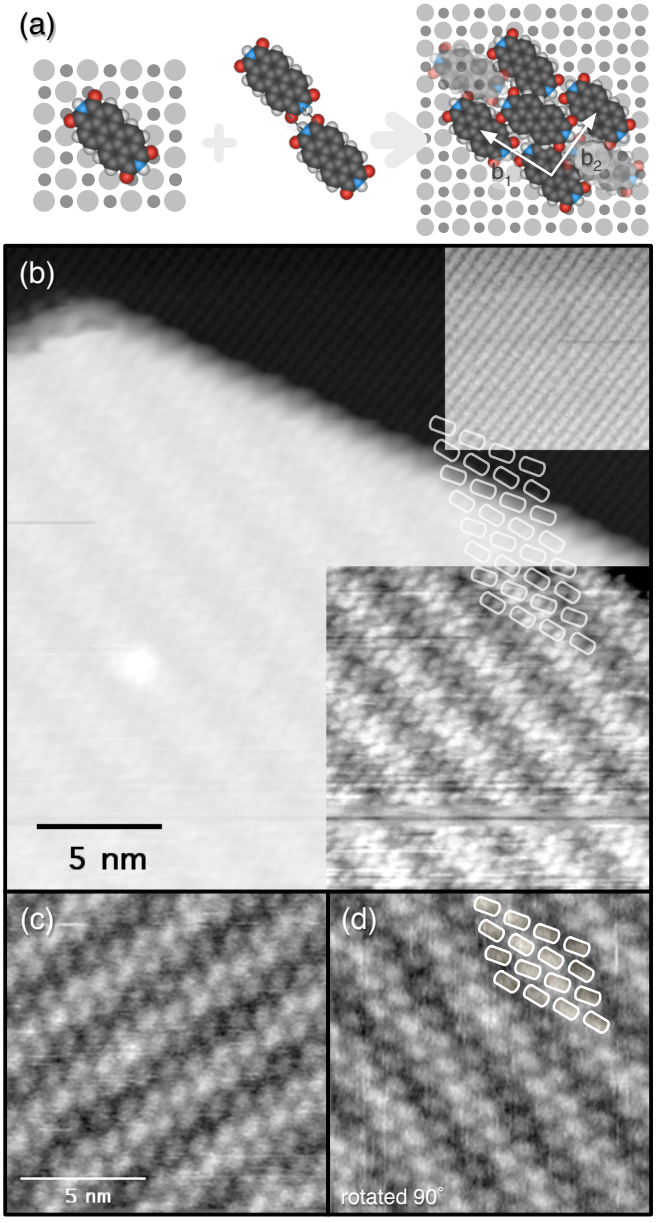

Figure 5.4: PTCDI overlayer relation to KBr. The proposed adsorption of PTCDI on KBr is shown in the far left of (a) with the H-bonded intermolecular arrangement at the middle. The epitaxy determined from the high resolution image (Imaging parameters: $\Delta f = -5.7$Hz, size: 20 nm $\times$ 20 nm, z-scale: 680 pm) in (b) is shown schematically on the far right of (a). In (c) the molecules appear as single oblong protrusions, whereas in (b) they appear as pairs of two protrusions. The image in (c) from a different crystallite (Imaging parameters: $\Delta f = -9.2$Hz, size: 10 nm $\times$ 10 nm, z-scale: 50 pm image acquired by J. Topple) is shown rotated in (d) for comparison to (b).

adsorption site based on a similar interaction with the surface as PTCDA, and the intermolecular bonding motif for comparison. Given the lattice constants determined, and a close examination of other high resolution images, the PTCDI molecules are expected to be canted (rotated with respect to the row direction) by a small angle as shown in the schematic as well. Structural modelling both to determine the preferred adsorption sites and the detailed molecular arrangement, for example the canting angle which is difficult to accurately determine from images, is needed.

It should be noted that the image shown in figure 5.4b appears to exhibit sub-molecular resolution. While this is of interest, and the ability to obtain sub-molecular resolution opens many possibilities for investigation, it also complicates the interpretation of the images. In the image shown, pairs of protrusions are identified as PTCDI molecules (see overlay in fig. 5.4b) based on a comparison with an image (fig. 5.4d) where molecules seem to appear as single protrusions. While the appearance of the molecule as a pair of protrusions is sensible based on the charge distribution of the molecule, for rigourous interpretation of the image and therefore a more confident determination of structure, detailed modelling of the contrast mechanisms should be undertaken.

In summary, PTCDI forms needle-like islands on KBr with no evidence for a dewetting process. As in the bulk PTCDI crystal, the molecules are arranged end-to-end in rows, and a small cant angle is anticipated. A superstructure of repeating stripes is prevalent on PTCDI islands and maybe a result of coincidence with the underlying substrate or due to a strained epitaxy. Submolecular resolution was obtained for this molecule, and preliminary analysis indicates that the molecules appear here as two bright protrusions, however, accompanying modelling of the relevant contrast mechanisms is needed.

5.1.2 PTCDI on NaCl

PTCDI was deposited on NaCl under similar conditions. A range of coverages from 0.1–0.7ML has been examined thus far, deposited at rates of $\sim$0.01Å/s (or 0.003ML/s), all of which show similar growth behaviour.

Imaging of the morphology shortly after deposition reveals bimodal growth

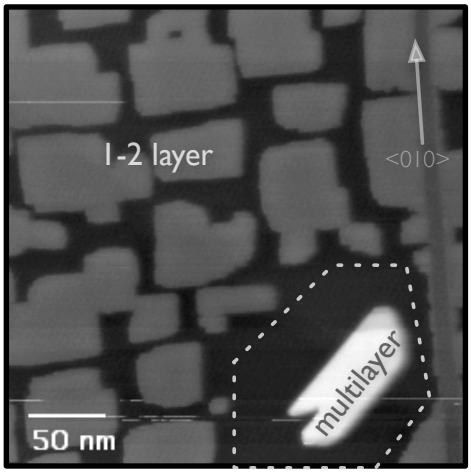

Figure 5.5: Bimodal growth PTCDI on NaCl. 1-2 layer square islands coexist with multilayer needle-like crystallites shortly after deposition but spontaneously dewet, leaving only needle-like crystals. [163]

similar to that observed for PTCDA on NaCl (see fig. 5.5). Square islands consisting of 1-2 layers of PTCDI cover the majority of the substrate exhibiting alignment with the <100> directions of the NaCl. These islands are typically only 1 layer, however transient second layers have been observed on smaller islands, and stable second layers have been observed on large islands with this morphology. Co-existing with these square islands are mulitlayer needle-like crystallites which have a similar appearance to the PTCDI crystallites observed on KBr. These consist of two or more layers, and similar to those on KBr, are oriented at a small angle, $\pm \sim 16^\circ$ (error $\pm 1^\circ$), from the <110> directions of the substrate. Depletion of the square mono- to bi- layer islands around mulitlayer islands is also observed, similar to that seen for PTCDA on NaCl (see fig. 4.9a). [163]

Unlike PTCDA on NaCl, however, the dewetting occurs spontaneously, ie. without annealing, on a timescale readily observable with nc-AFM. Over the course of hours up to several days, the multilayer needle-like crystals grow at the expense of the square mono- to bi- layer islands. This is shown in the sequence of three images of the same area spanning $\sim$10 hours in figure 5.6. Some unstable second layer regions can be seen on the monolayer islands, and the needle-like crystals expand from nucleation centers at the step edges with additional layers continuing to grow on top. An image taken shortly after the end of the sequence in a different area of the sample is shown as well where only needle-like crystals are observed and the monolayer islands have similarly disappeared indicating that the tip does not induce the observed dewetting. The time required for complete

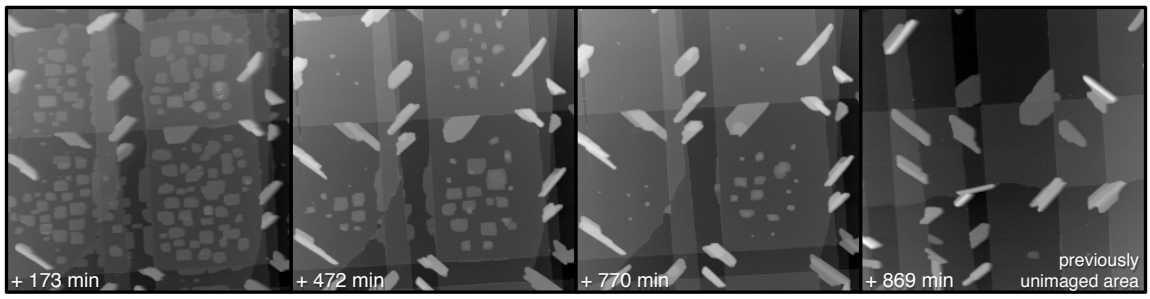

Figure 5.6: Sequence of three images of the same area spanning ∼10 hours showing growth of needle-like multilayer crystals at the expense of mono- to bi- layer square islands. The fourth frame was acquired after the sequence in a region of the sample several hundred nanometers away, indicating that the tip does not drive the dewetting process while acquiring the sequences. (Image parameters: Δf ≃4Hz, size: 770 nm× 770 nm) [163]

dewetting of the square islands is highly dependant on the substrate morphology as this dictates the number of nucleation sites for the needle-like crystals, thus the process can occur over the course of ∼1 day up to 1 week as observed so far. Characterization of the dynamics of the dewetting process is currently underway. Factors believed to contribute to the dynamics include the stability of each island type, capture rates of each island type and diffusion rates for PTCDI. [163]

To investigate whether the dewetting is similarly driven by a rearrangement of the molecular lattice, the epitaxy of each structure was determined. Again, the known NaCl lattice is used as a reference in images resolving both the molecular overlayer and the ionic lattice of the substrate. The square mono- to bi- layer islands exhibit a 2×2 brickwall structure with the molecular axis aligned with the <110> directions of the substrate, with all molecules in equivalent adsorption sites. Based on the calculations performed for PTCDA on NaCl [56], we believe this allows the partially negatively charged acyl oxygens on either side of the -NH group to interact with the Na^+ ions of the surface, thus maximizing the interaction with the surface. The needle like PTCDI crystallites exhibit a similar structure to those observed on KBr with rows of molecules aligned end-to-end. As with the structure observed on KBr, the molecules appear to be canted (molecular axis is rotated with respect to the rows) by a small angle. One possible structure (taken as the lowest fraction within error) determined from the image shown in figure

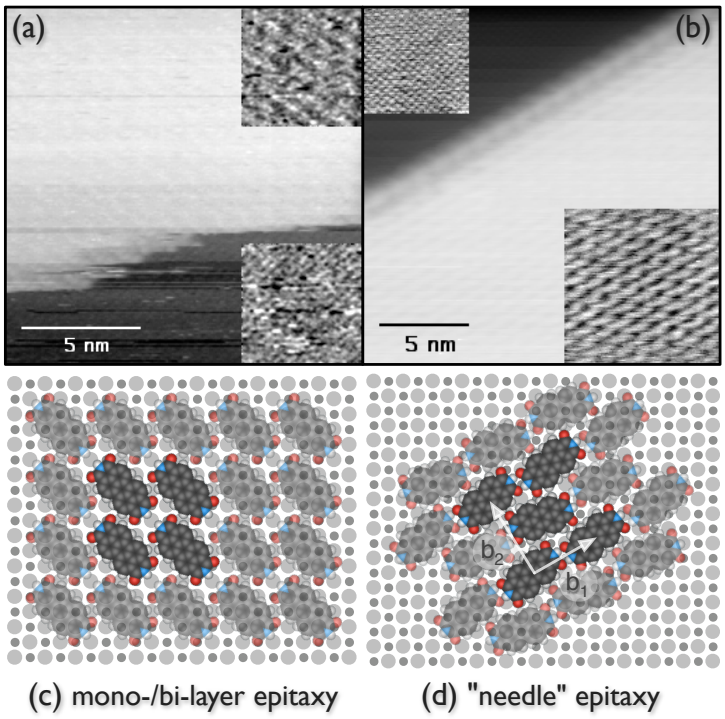

Figure 5.7: High resolution images of a monolayer island (a) (Imaging parameters: $\Delta f = -15$Hz, z-scale: 0.6 nm, insets enhanced for contrast) and a multilayer needle-like island (b) (Imaging parameters: $\Delta f = -24$Hz, z-scale: 1.2 nm, insets enhanced for contrast) used to determine the epitaxy of PTCDI on NaCl with schematic representations of each epitaxy (c and d). [163].

5.7b with a matrix of

$$\begin{pmatrix} 2.15 \pm 0.09 & 1.24 \pm 0.04 \\ -1.5 \pm 0.1 & 2.55 \pm 0.09 \end{pmatrix} \sim \begin{pmatrix} 17/8 & 5/4 \\ -3/2 & 5/2 \end{pmatrix}$$

is shown schematically in the lower right of figure 5.7. However, it is possible that the different orientations of these needle-like crystals have different epitaxies. [163]

The structure shown was derived from the measured lattice parameters which are b_1=13.9$\pm$0.5Å, b_2=16.5$\pm$0.4Å, and β=90$\pm$2° , with a rotation of θ=30$\pm$2° , which corresponds closely to the measured angle of the island edges. Recalling that the bulk $(10\bar{2})$ plane, in which we have b_1=14.40Å, b_2=14.66Å, and β=90° , the resulting molecular lattice is still comparable to the $(10\bar{2})$ plane but is somewhat distorted due to a greater degree of mismatch between the substrate and overlayer lattices.

As with PTCDA on NaCl, PTCDI exhibits both two different island morphologies and two different accompanying epitaxies. While the intermolecular interaction changes the bonding motif of the molecular crystal, the same modality

	PTCDI bulk $(10\bar{2})$	PTCDI on KBr	PTCDI on NaCl
b_1	14.40Å	14.3±0.2Å	13.9±0.5Å
b_2	14.66Å	15.1±0.3Å	16.5±0.4Å
β	90°	92±1°	90±2°

Table 5.1: Lattice parameters for bulk PTCDI $(10\bar{2})$ plane, compared with multilayer crystallites on KBr and NaCl.

is observed whereby a metastable epitaxy drives the formation of layer-by-layer type structures, but is likely not the energetically favourable structure.

5.1.3 Summary of PTCDI results

For both substrates, multilayer islands of PTCDI show a bulk-like structure which appears to correspond reasonably well with the $(10\bar{2})$ plane of the bulk crystal (see table 5.1). This is in contrast to the structures which have been found on other surfaces which more closely correspond to the $(\bar{1}2\bar{1})$ plane discussed by Guillermet *et al.* [158]. Moreover, the metastable 1-2 layer structure observed shows a commensurate epitaxy indicating the presence of a strongly preferred adsorption site.

Despite a significantly different intermolecular bonding motif resulting in different epitaxies and different morphologies, the overall growth behaviour of PTCDI is strikingly similar to that of PTCDA. A pure island growth mode, with a bulk-like structure, is observed for PTCDI on KBr, resulting in needle-like crystallites formed predominantly at step edges. For PTCDI on NaCl, a bimodal growth with two different accompanying epitaxies is formed leading to a dewetting scenario much like that observed for PTCDA on NaCl. Again, the formation of a metastable structure which appears unable to support additional (more than two in this case) layers leads to the spontaneous dewetting of these initial structures into bulk-like crystallites.

The prevalence and commonalities of dewetting in these molecular systems on insulating surfaces is intriguing and the development of a predictive framework for the occurance and timescales of dewetting in such systems could greatly increase our ability to grow films with the desired structure.

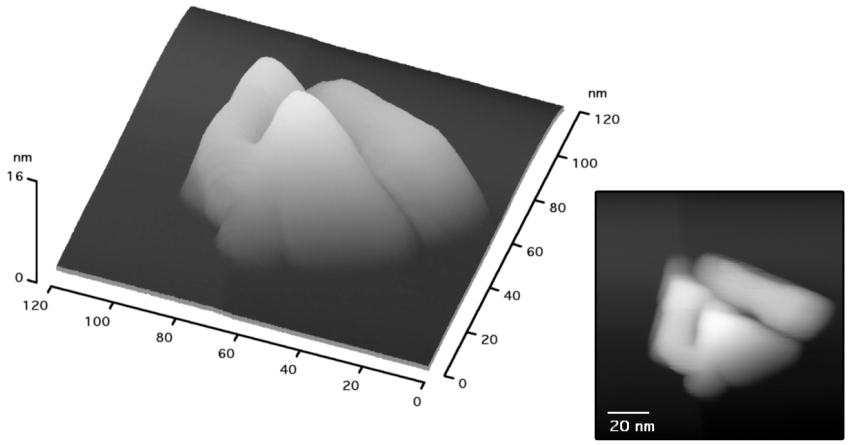

Figure 5.8: CuPc island formed on an NaCl substrate. Islands observed were typically 15-20nm high.

5.2 Preliminary results for CuPc growth on NaCl

Copper (II) Phthalocyanine (CuPc) is a common commercial dye and is often studied in the context of organic thin film electronics for use in thin-film transistors, organic LEDs and as a donor material in organic heterojunction solar cells [15]. As with other metallo-Pcs, the metal ion is located at the center of a conjugated organic ligand. Due to the small size of the Cu^{2+} ion, the ligand retains a planar structure [164]. It has been postulated that metallo-Pcs would form ordered epitaxial or quasi-epitaxial (coincident) structures on alkali halides through interaction of the metal ion with the negative ions of the surface leaving the ligand free to rotate and accommodate intermolecular interactions [15]. Hence, given the correct kinetic conditions, it might be expected that monolayer structures of this description may be formed.

Approximately 2Å of purified CuPc was deposited on a freshly cleaved NaCl surface by thermal evaporation at 400° C. See Appendix B for details concerning purification method.

As seen in figure 5.8, relatively tall islands were observed. As with other molecules investigated, the majority of these islands were found at step edges, indicating the ability of molecules to diffuse distances of at least a few hundred nanometers. These islands appear to have facetted edges, but the presence of multiple edges may indicate that they are either polycrystalline, or defected structures.

Molecular resolution was obtained on the top surface of a CuPc island (see 5.9b) revealing a slightly distorted square arrangement of molecules similar to

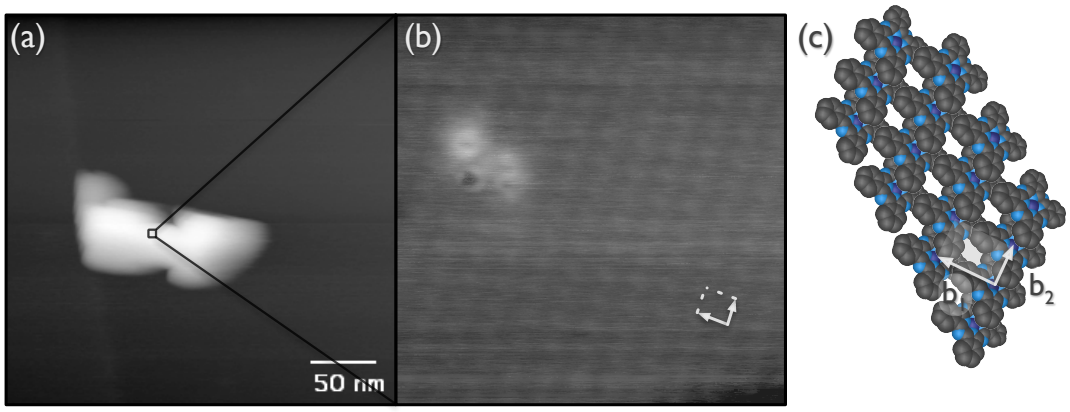

Figure 5.9: High resolution imaging on an island shown in (a) showing ordered CuPc (b) (imaging parameters: Δf=-4.9Hz, 15nm$\times$15nm, corrugation $\sim$20 pm). Possible stacking shown in (c) similar to that described in [165] for thick films of CuPc on Si(111).

that observed by Fukuma *et al.* for multilayer islands of CuPc on MoS_2 [164]. However, in contrast to Fukuma and co-authors, we observe the CuPc molecules as elongated features, possibly indicating that the molecules are tilted out of the plane of the top surface of the crystallite, as reported for thick films of CuPc on Si(111) [165]. The lattice parameters measured from this image, $b_1 = 1.3 \pm 0.1$nm, $b_2 = 1.0 \pm 0.1$ and $\beta = 85 \pm 1^\circ$ without calibration to the substrate, indicate a lattice that is smaller in the b_2 direction than is typically observed, consistent with the idea that the molecules are tilted out of the surface plane here.

In addition to the islands observed at step edges, some molecular scale features with a spacing of $\sim$2nm were observed along NaCl steps (see fig. 5.10). These features are most likely attributable to CuPc molecules adsorbed at the step edge, and may be an indication of the formation of a structure similar to that previously proposed for metallo-phthalocyanines on alkali halides [15]. It may then be possible to form monolayers at reduced substrate temperatures or under other different kinetic conditions during growth (eg. rate, crucible temperature, etc.). It should also be noted that the ionic lattice of the NaCl surface can be seen in figure 5.10b, indicating the absence of a CuPc monolayer and a pure island growth mode.

The results shown for CuPc here are merely preliminary and further investigation including refinement of the deposition conditions, variation of coverages and rates, the use of additional substrates and careful determination of the ob-

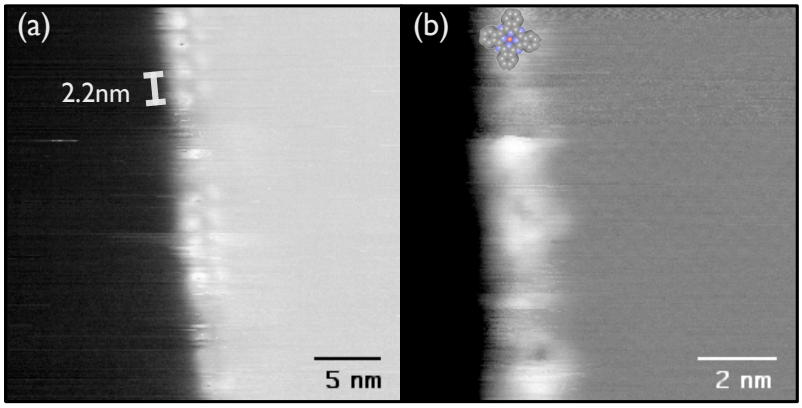

Figure 5.10: High resolution images of features at NaCl step edges showing molecular scale features adsorbed at the step edges. Spacings are consistent with proposed molecular arrangements on alkali halides [15]. (b) also shows the ionic lattice of the NaCl surface indicating that there is not a monolayer present on the open surface. (Imaging parameters: (a) Δf=-6.4Hz, 30$\times$30nm, (b) Δf=-9.5Hz, 10$\times$10nm)

served structures, is needed for comparison with the other systems investigated herein.

6

Conclusions and Future Directions

6.1 Ubiquity of dewetting and a generalization framework

While dewetting has been observed for several organic molecular materials on metallic substrates [62, 64, 65], there have been relatively few growth studies to date of molecular deposits on insulating substrates. Of those studied in this thesis and otherwise reported on insulating substrates, dewetting phenomena appear to be exceptionally common. In attempting to understand the prevalence of dewetting among molecule–on–insulator systems, one may ask *what factors make molecular deposits on insulators susceptible to dewetting phenomena?* Why is dewetting so likely to occur for molecules on insulators?

First, we may examine the relative surface energies of molecular materials and insulating crystals (for some examples, see table 6.1). The surface energies of the (100) cleavage planes of alkali halides are expected to be of the order a few hundred mJ/m^2 [166]. While the surface energies of molecular materials have only more recently been investigated, calculated values for a few molecular crystals can be found in the literature and lie in the range of 50-200 mJ/m^2 [167, 168]. The close competition of these values leads to a situation where the interface energy plays a primary role in determining the growth mode of molecular materials on insulating surfaces, and it is this subtle balance with which we are concerned.

As the interface energy (and to some extent the molecular crystal surface energy) is sensitive to the details of the structure, we may look more closely at the epitaxies observed for the various systems. Table 6.2 contains a summary of the structures observed (including one example from the literature) and whether

Material	Surface Energy
KBr(100)	0.151 J/m^2 [166]
NaCl(100)	0.188 J/m^2 [166]
LiF(100)	0.169 J/m^2 [166]
C_{60}	0.116 J/m^2 [113]
pentacene	0.0496 J/m^2 [167]
anthracene	0.0528 J/m^2 [167]
Au	1.333 J/m^2 [169]
Pd(111)	1.64–2.00 J/m^2 [170]
Ta	2.493 J/m^2 [169]

Table 6.1: Surface energies of some alkali halides, organic crystals and metals for comparison

dewetting occurs. Two measures of the correspondence between the overlayer and substrate lattices are included: the ratio between overlayer lattice constant and the substrate lattice constant (or preferred sites, where the symmetry of the overlayer and substrate differ) denoted as g_i, and the fractional strain of the molecular lattice for the observed structures denoted as Δb_i. The first of these, the g_i, are an indication of the epitaxy which would most closely match the molecular lattice, for example, for PTCDA on KBr, $g_1 \simeq 2$ and $g_2 \simeq 3$, which corresponds to the stable 2×3 herringbone structure observed.

Of particular interest, is the correspondence between *polymorphic epitaxies* and the occurrence of dewetting. As the interface energy will be sensitive to these different possible epitaxial structures, it is then understandable how dewetting may arise. The formation of a metastable structure has the potential to produce a different balance of surface energies than that of the energetic minimum giving rise to two different growth modes, as suggested by F. Silly *et al.* for Au on $SrTiO_3$ [63]. For both PTCDA and PTCDI, where two different epitaxial relations were observed dewetting occured. For both of these molecules, no dewetting and only one epitaxy was observed on KBr, likely due to closer lattice matching and a different balance between the intermolecular interactions and molecule–substrate interactions. Such polymorphic epitaxies, the occurance of more than one stable epitaxial relation, are more highly probable for molecular systems, and perhaps for molecule–on–insulator systems in particular due to the expectation of a weaker molecule–substrate interaction in this case. The origin of this lies in the both weak,

system	g_1	g_2	observed	Δb_1	Δb_2	dewetting
C_{60} | KBr	0.963*	0.991*	$\begin{pmatrix} 3/2 & 9/20 \\ 2/7 & 207/140 \end{pmatrix}$	-0.01	-0.03	**yes** (<1hr)
C_{60} | NaCl	-	-	-	-	-	**yes** (<1hr)
PTCDA | KBr	1.81 (α) 1.89 (β)	3.02 (α) 2.92 (β)	p2x3	0.124 (α) 0.075 (β)	-0.011 (α) 0.05 (β)	no
PTCDA | NaCl	2.14 (α) 2.22 (β)	3.56 (α) 3.45 (β)	p3x3	0.48 (α) 0.44 (β)	-0.31 (α) -0.25 (β)	**yes** (>1 week without annealing)
			p2x3	-0.08 (α) -0.12 (β)	-0.31 (α) -0.25 (β)	
PTCDA | KCl†	1.9 (α) 2.0 (β)	3.2 (α) 3.1 (β)	2x2 (brickwall)	-	-	**yes**
			$\begin{pmatrix} 1.70 & 2 \\ -3.57 & 3 \end{pmatrix}$	-0.02 (α) -0.06 (β)	0.04 (α) 0.08 (β)	
PTCDI | KBr	2.2	2.2	$\begin{pmatrix} 5/4 & 7/4 \\ 2 & 5/4 \end{pmatrix}$	-0.007	0.03	no
PTCDI | NaCl	2.6	2.6	2x2 (brickwall)	0.097	0.078	**yes** (2 days-1 week)
			$\begin{pmatrix} 17/8 & 5/4 \\ -3/2 & 5/2 \end{pmatrix}$	-0.03	0.12	

* relative to preferred adsorption sites
† T. Dienel et al. Adv. Materials 20, 959 (2008)

Table 6.2: Overview of structures observed and occurrence of dewetting for organic molecules on alkali halides determined by nc-AFM. g_i denotes the ratio between the molecular lattice vector and the substrate lattice vector, and Δb_i denotes the strain induced in the molecular lattice for the observed structure. The g_i are given with respect to the preferred lattice sites where symmetries do not match, and the Δb_i are not defined where a different molecular motif is observed compared to the bulk.

and *soft* interactions between molecules which also give rise to polymorphism in bulk organic crystals. While the detailed interaction mechanisms between large organic molecules and insulating substrates such as alkali halides are only beginning to be investigated [56, 124, 171], these are also likely to be dominated by van der Waals and electrostatic interactions. Additionally, as the interaction is integrated over the large area of the molecule, the molecule–substrate interaction is expected to be similarly both weak (physisorption) and soft. The close competition between these interactions, the low stiffness of these interactions allowing deformation of the overlayer lattice as well as coincident lattices, and the typically differing lattice geometries of molecular crystals and inorganic substrates will more likely give rise to rich energetic landscapes leading to multiple stable structures.

Figure 6.1 shows a simple 1D example of how a metastable epitaxy could arise from a lattice mismatch. In the top graph, the equilibrium distance for the intermolecular potential (modelled as a simple Lennard-Jones 6-12 potential) is set to twice the substrate lattice constant (l.c.), and a deep well in the total adsorption potential results at 2 l.c. from the first particle. In the bottom graph, the equilibrium distance for the intermolecular potential is changed to an incommensurate value of 2.3 l.c. resulting in a global minimum at $\sim$2.2 l.c. and a second minimum of similar energy at ~ 3 l.c. with a barrier of nearly $1/3$ the total adsorption energy. This energy barrier will influence the timescale and temperature at which a transformation of structure could occur, in addition to the diffusion barriers which control mass transport from one structure to the other. It is also interesting to note that the metastable minimum in this example occurs at a distance commensurate with the substrate lattice, whereas the global minimum would result in an incommensurate adsorption. This effect can also be seen in the metastable structures observed (refer to table 6.2) as these metastable epitaxies show commensurate registry with the substrate, favouring the the molecule–substrate interaction rather than the intermolcular interaction. The final stable molecular structure is then a compromise between the intermolecular interactions and the molecule–substrate interaction and can be incommensurate or coincident with the substrate. While the model example is simplistic compared to the complexity of the adsoprtion of a large organic molecule, it illustrates the ease with which a metastable epitaxy can be formed.

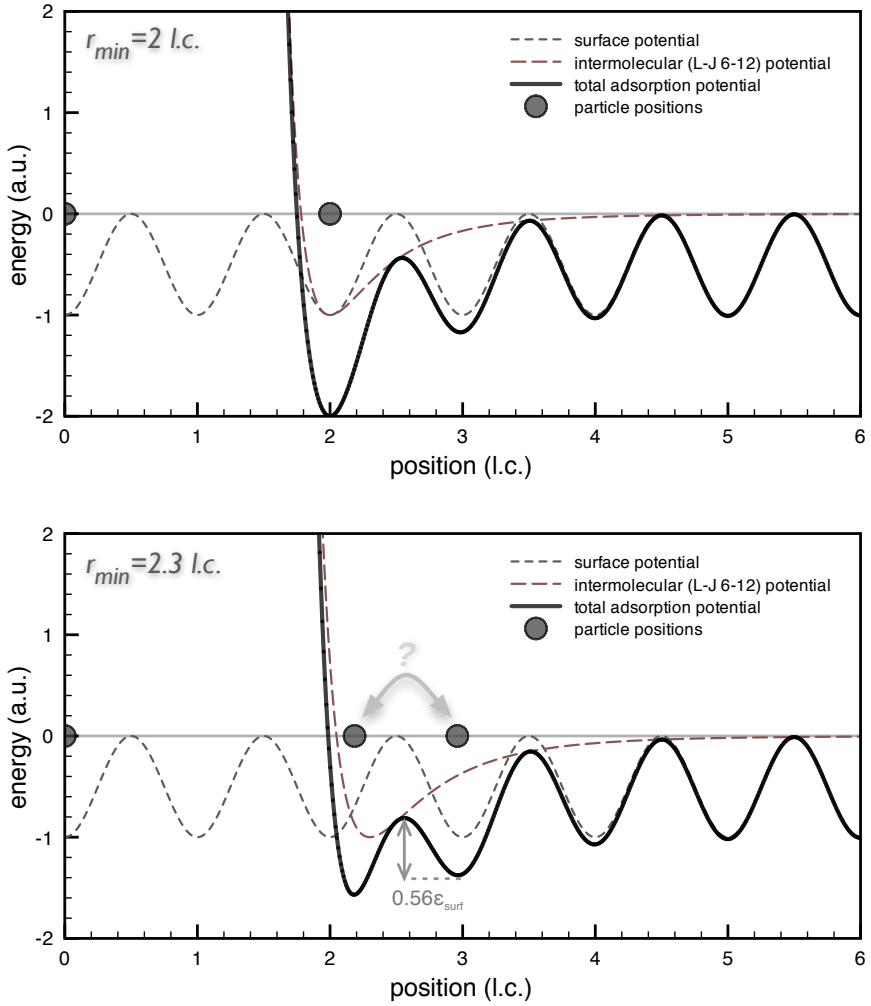

Figure 6.1: Simple 1d model showing the deep potential minimum for a commensurate adsorbate pair (top) and the formation of a metastable state as a result of an incommensurate adsorbate pair (bottom).

For a deeper look at the richness of the energetic landscape which can occur when adsorbate–adsorbate interactions compete closely with adsorbate–substrate interactions we may look to the description of commensurate–incommensurate phase transitions by a Frenkel'–Kontorova model [172] which characterize many physisorption systems [30]. By considering a simple ball and spring model with an equilibrium separation smaller than the surface corrugation upon which this overlayer is placed, the system will move from a lattice commensurate with the substrate, through a phase containing both commensurate and incommensurate regions (giving rise to solitons) to a true incommensurate phase with a lattice constant matching the equilibrium position of the springs. When modelled for a 2-dimensional surface for the specific case of Krypton on graphite, regions of different commensurate domains can be found separated by grain boundaries, or solitons [30, 173]. At elevated temperatures, these boundaries become less ordered, forming intricate structures. The often nearly commensurate lattices of molecular overlayers on insulators may well follow similar structural transitions. In particular, a comparison of the observed C_{60} lattice with the calculated preferred lattice sites reveals a situation similar to Krypton on graphite whereby the equilibrium overlayer lattice constant is slightly smaller than the lattice of preferred adsorption sites. The origin of the intricate morphology of the C_{60} islands formed as a result of dewetting may well be a network of solitons which by their unstable nature initiate and lead the dewetting process. While such an approach disregards much of the complexity of the interactions, a similar analysis may yield a predictive framework for the occurence of molecular dewetting as well as some insight into the resulting morphologies.

Given the close competition of overlayer and substrate surface energies, closely competing intermolecular and molecule–substrate interactions, compliance (softness) of these interactions and common lattice mismatch as a result of different lattice geometries and scales, it is perhaps not surprising that dewetting appears frequently for molecular deposits on insulating substrates. The latter two conditions give rise to metastable structures, while the first suggests that multiple interface structures (epitaxies) are likely to result in a dewetting scenaro.

6.2 Open Questions

Regarding growth

Although many of the unique and interesting morphologies of molecular islands on alkali halides appear to be formed through dewetting processes, the detailed formation mechanisms of these patterns is not yet known. The conceptualization of an "ungrowth" process rather than a growth process explains some of the rather unique features observed, for example the disconnected regions and branches which wrap inwards for C_{60} islands, and perhaps examination of the processes involved in dewetting of a molecular film will lead to an understanding of the formation of these interesting structures.

Perhaps more importantly in the context of growth, *can one predict, and even control the occurrence of dewetting?* Through analysis of epitaxial structures formed within the framework of commensurability, combined with an understanding of the competing interactions present in molecule–on–insulator systems, it may be possible to *a priori* predict which systems are likely to exhibit bimodal growth and dewetting. Thorough knowledge of the stability of the differing structures and the dynamical processes involved in dewetting may further lead to understanding of the time scales and kinetic conditions under which the prerequisite metastable structures form and dewetting occurs pointing to methods for controlling growth in these systems.

Regarding the molecule–substrate interaction

A more critical issue perhaps, to both the understanding of molecular growth on insulators and for possible future device applications, is the elucidation of the interaction mechanisms between molecules and insulating surfaces. *What is the strength of the interaction? What mechanisms are involved? Is the surface benign towards the molecule, or does it influence properties one hopes to use (eg. conductance)?*

Through the synergy of the experimental data shown here and parallel theoretical efforts, advancements in understanding the interaction mechanisms of organic adsorbates on insulating surfaces are being made. For the C_{60} on KBr system, there appears to be a charge transfer according to DFT calculations accompanied

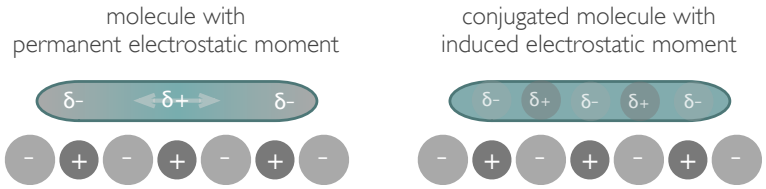

Figure 6.2: Conceptualization of molecule with permanent electrostatic moment vs. an induced charge distribution in a delocalized conjugated region as a result of the charge distribution of the substrate. The partial charges of the molecule with a static charge distribution are expected to interact strongly with the surface ions. Conjugated molecules, or conjugated regions of molecules, may show a redistribution of charge as a result of the electric field from the substrate giving an induced partial charge distribution.

by a redistribution of charge within the molecule in response to the ionic surface [124]. For PTCDA on both NaCl and KBr, the interaction mechanism between the molecule and substrate was found to be primarily a combination of van der Waals and electrostatic interactions (see section 4.2.1, appendix F, and [124]). Perhaps of particular interest is the importance of electrostatic interactions for adsorption of large organic molecules on ionic crystal surfaces, both in the static moment case where a charge separation is inherently present in the molecular species and in the induced moment case where a highly polarizable species responds to the substrate (see figure 6.2).

Furthermore, the nature of the molecule–substrate interaction speaks to the influence of the substrate on molecular properties. While for PTCDA there is no evidence for charge transfer, and the changes in electron density resulting from the ionic surface do not produce significant distortion of the energetic structure, the presence of a slight charge transfer between C_{60} and KBr indicates that transport properties may be influenced. Consideration of the substrates to be used for single molecule transport experiments will likely be of importance when comparing with theoretical calculations, even when a supposedly inert insulating substrates are used.

In order to compare with theoretical calculations of the influence of insulating substrates on molecular states, experiments involving insulating thin films on metal substrates may provide insight by allowing electronic characterization through techniques such as photoemission spectroscopy and electron energy loss

spectroscopy.

6.3 Future Directions

The example given here of PTCDA and PTCDI demonstrates how a small chemical modification can significantly influence morphology. An understanding of how changes in intermolecular interactions influence growth will be of considerable importance when considering functionalization of molecules for specific tasks. For example, the attachment of functional groups, such as thiols (–SH), which provide good electrical and mechanical connections to metal contacts is frequently used in measurements of single molecules. It is likely that the attachment of such functional groups will also influence adsoprtion geometries and growth morphologies. Additionally, for the assembly of molecular devices the presence of metal structures may also influence growth [136] which could be used as a templating strategy. However, better understanding of the interplay between the intermolecular, molecule–substrate, and molecule–metal interactions and how this influences growth is still needed. Studies of the influence of molecular functionalization on growth and modifcation of growth in the presence metal clusters is ongoing.

To further investigate the occurance and process of dewetting, continuing studies should include a greater exploration of accessible kinetic phase space including deposition at lower substrate temperatures and a wider range of deposition rates. As the formation of a metastable monolayer is a kinetically controlled, non-equilibrium process, alteration of rates and substrate temperature should influence whether or not dewetting occurs. Although dewetting was not observed for PTCDA or PTCDI on KBr, it may be possible under certain conditions to form the pre-requisite monolayer triggering dewetting upon annealing or over time. Additionally, the dynamics of the dewetting process are currently under investigation [163] and the influence of kinetic factors on the temporal evolution of islands may be of future interest.

Lastly, though the growth and structure of molecular films on insulating substrates are alone of interest to the fields of single molecule electronics and thin-film organic electronics, it is the connection between structure and electronic or

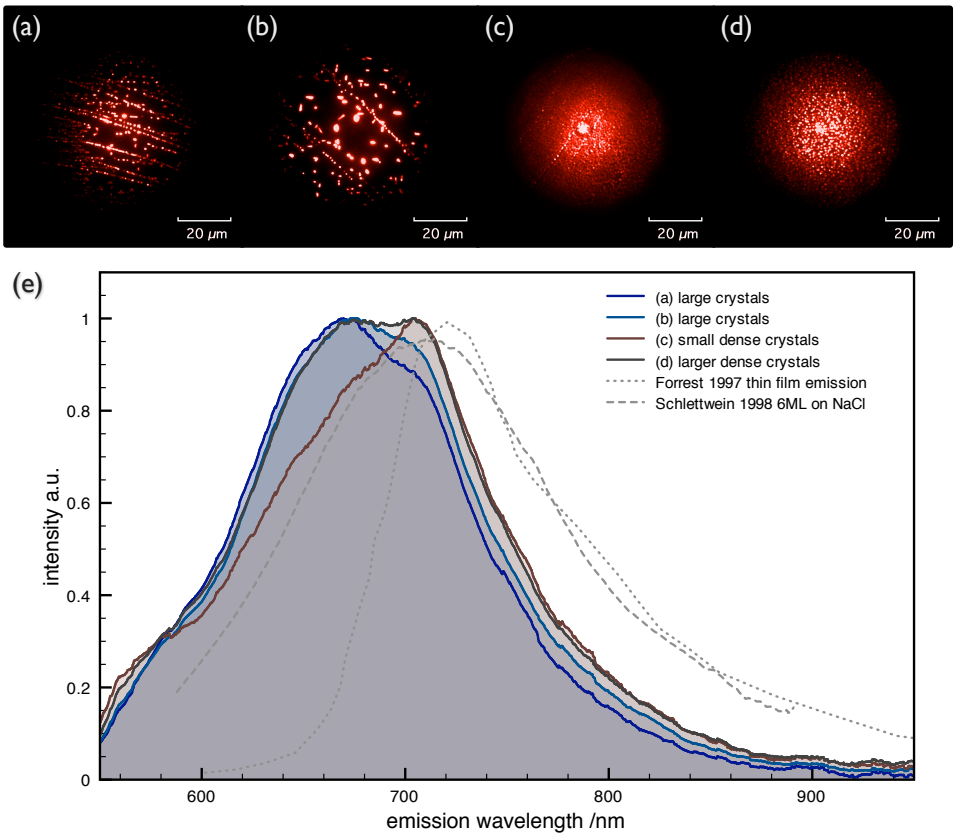

Figure 6.3: Morphological influence on fluorescence spectra of PTCDA. Microscope images of different regions of an annealed 0.75ML PTCDA on NaCl sample (a-d) with corresponding fluorescence spectra (e) from excitation at 488nm. Regions with large, well ordered crystals, corresponding to (a) and (b) exhibit stronger peaks at higher energy (lower wavelength) than regions with smaller clusters at higher density (c) and (d). Fluorescence images taken using Cascade 1K camera mounted on an Olympus IX71 inverted microscope with 60x NA 1.45 objective and filter set (dichroic Semrock FF506di, emission filter Chroma HQ505LP). Spectra were recorded by an Ocean Optics HR2000 (H4 550nm+ grating) spectrometer with dichroic (Chroma Z488RDC). All spectra were processed by subtraction of the background, smoothing, and normalization. Spectra from Forrest [15] and Schlettwein *et al.* [135] are shown for comparison.

optoelectronic properties which are of greatest concern. As such, the integration of techniques such as optical spectroscocpy which can give access to electronic and vibrational states, with scanning probe microscopy techniques which can reveal the details of molecular structures which will be of utmost importance. *Ex situ* local fluorescence microscopy and spectroscopy were performed on annealed sub-monolayer PTCDA islands indicating that (a) there is great variability in the size and density of PTCDA crystallites over the surface, and (b) these different morphologies result in different electronic structure as evidenced by a shift in relative peak heights in the emisssion spectra (see fig. 6.3). While these results are merely preliminary, they demonstrate the importance of careful control and characterization of structure and structure–property relationships.

A

Glossary of organic nomenclature used

acyl functional group consisting of RCO–

carboxylic anhydride functional group consisting of two acyl groups connected by an oxygen

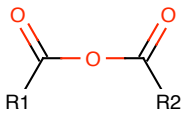

conjugated containing higher order bonds; leads to delocalization of electrons in a molecule, eg. double bonds, aromatic and polyaromatic bonds

imide functional group consisting of two acyl groups connected by a nitrogen (–NH)

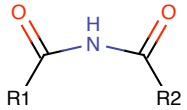

perylene planar aromatic compound consisting of 5 rings

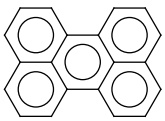

thiol a functional group consisting of –SH

B

Materials: composition, purity, sources and preparation

B.1 Single crystal substrates

Potassium Bromide, KBr
transparent single crystal, {100} faces as cleaved
Korth Kristalle GMBH
Am Jägersberg 3, D24161 Altenholz (Kiel)
http://www.korth.de

Sodium Chloride, NaCl
transparent single crystal, {100} faces as cleaved
Korth Kristalle GMBH
Am Jägersberg 3, D24161 Altenholz (Kiel)
http://www.korth.de

Magnesium Oxide, MgO
transparent single crystal, {100} faces as cut or one side polished
Korth Kristalle GMBH
Am Jägersberg 3, D24161 Altenholz (Kiel)
http://www.korth.de
and
MTI Corporation
2700D Rydin Road, Richmond, CA 94804, USA
http://www.mtixtl.com

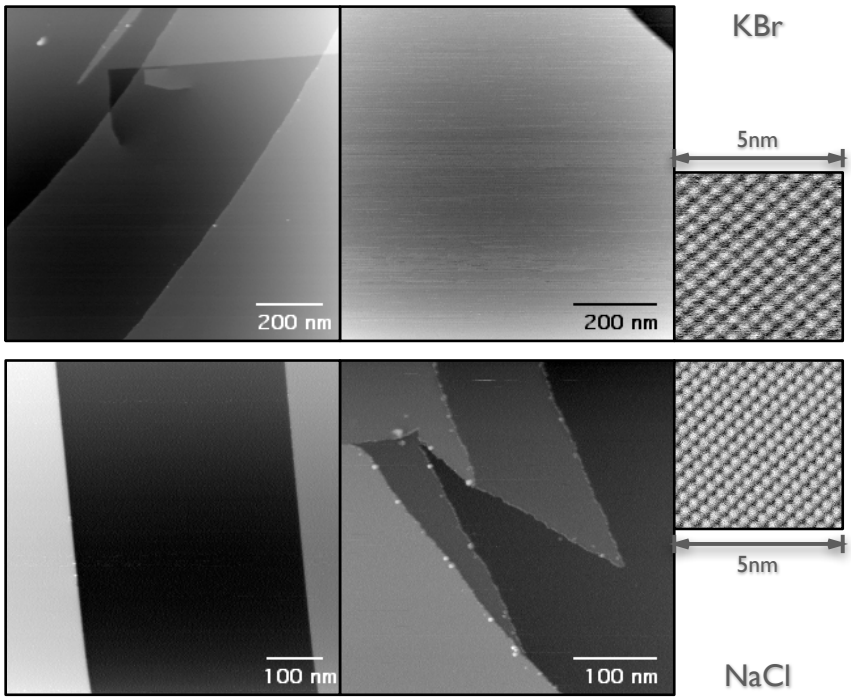

Figure B.1: Images of cleaved KBr (top) and NaCl (bottom) (001) surfaces.

B.1.1 Preparation of single crystal substrates

Single crystal substrates were usually purchased in blocks of size: 40mm $\times$ 20mm $\times$ 10mm, which were then cleaved by means of a razor blade and a hammer to a size of $\sim$10mm $\times$ 6mm $\times$ 2mm, appropriate for the sample holder provided by JEOL for use with the cleaving station. Harder materials, such as MgO, were purchased cut to size. This leaves a piece of the crystal protruding from the face of the sample holder to be cleaved off in UHV. Using a razor blade (or a diamond scribe for harder materials such as MgO) a line is scribed near the face of the sample holder to facilitate cleaving, ensuring that a crack has not developed through the crystal allowing contamination to the sample face to be used. The sample is then placed in the load lock for introduction into the UHV preparation chamber. The load lock pump-down brings the pressure to $\sim 5\times10^{-6}$Pa in 20-30 minutes.

Once moved to the preparation chamber, the cleaving station is advanced towards the sample position in the carousel where it docks securely to prevent

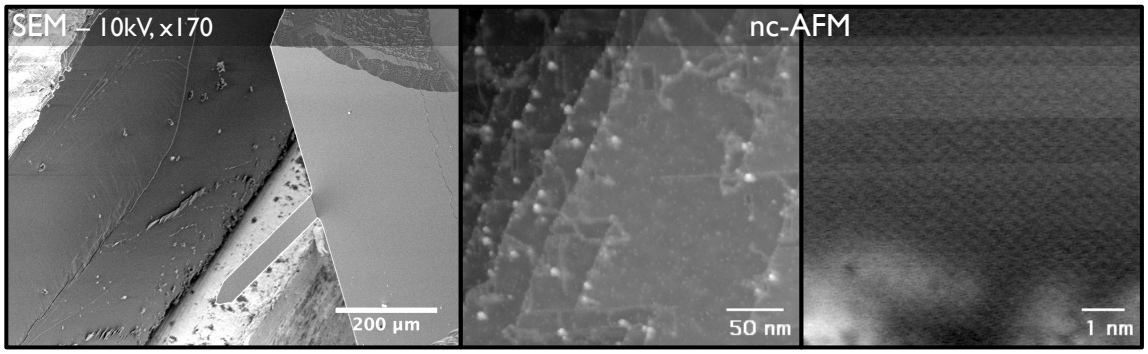

Figure B.2: SEM and nc-AFM images of cleaved MgO(001) surfaces.

misalignment during cleaving. A small steel block is advanced downward to the sample causing the protruding end to break off, usually at the position of the scribe near the sample face. While results of this cleaving method are somewhat variable, with some showing obvious large features on the surface, the majority of samples are usable for AFM study, and often large terraces on the order of several hundred nm to a few microns can be found on alkali halide surfaces. Typically, KBr yields better surfaces under this cleavage method, though equally flat surfaces were also observed on NaCl, but with lower frequency. This is likely a result of the stronger bonding of the NaCl crystal, thus requiring more energy in the cleaving process and leading to a greater chance of introducing defects. After cleavage, alkali halide samples are annealed at $\sim$150°C for 1hr to reduce charging a result of defects.

This method was somewhat less successful for MgO. The resulting surfaces were often charged despite heating to $\sim$800° C which is sufficient to induce defect mobility [174], and when imaging by nc-AFM was possible, a large number of defects were present on the surface. These defects fall into three main categories, similar to that observed previously for cleaved MgO [175]: large clusters at step edges, "strings", and charged point defects. While the first two types are predominantly at or near step edges, the latter type was found over all terraces at spacings of 5-10nm. This not only complicates imaging, but is expected to modify the growth of materials to be deposited by providing defect dominated nucleation sites. While a study of the effect of these defects on nucleation and growth of organic materials

on this catalytically active surface is of interest, without comparison with a defect free surface, concrete statements about the influence of defects on growth would be difficult to develop. As such, preparation of MgO surfaces was not pursued further. Possible avenues for use of MgO surfaces in future are the preparation of MgO thin films on metal substrates (eg. single crystal Fe [176] or Ag [177]), use of polished MgO crystals heated to high temperature to remove contamination, or the use of other *in situ* cleaving methods with possible annealing in a low pressure oxygen atmosphere.

B.2 Molecular materials

Buckminster Fullerene, C_{60}
brown–black powder, 99.5%
Alfa Aesar
26 Parkridge Road, Ward Hill, MA 01835 USA
http://www.alfa.com

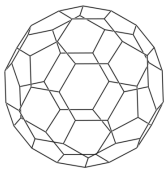

3,4,9,10-perylene tetracarboxyllic dianhydride, PTCDA
red powder, 98%
Acros Organics
Geel West Zone 2, Janssen Pharmaceuticalaan 3a, B-2440 Geel, Belgium
http://www.acros.com

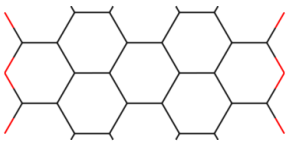

3,4,9,10-perylene tetracarboxyllic diimide, PTCDI
brown powder, 98%
Alfa Aesar

26 Parkridge Road, Ward Hill, MA 01835 USA
http://www.alfa.com

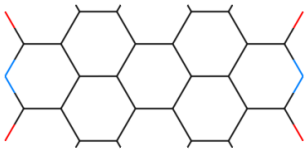

Copper (II) Pthalocyanine, CuPc
blue–purple powder, 95%
Acros Organics
Geel West Zone 2, Janssen Pharmaceuticalaan 3a, B-2440 Geel, Belgium
http://www.acros.com
Note: was further purified by thermal gradient sublimation purification by Simon LeFrancois, details below.

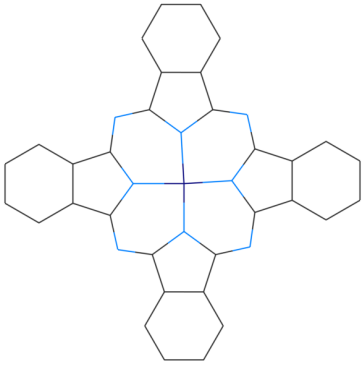

B.2.1 Deposition of molecular materials

Deposition of molecular materials was performed by thermal evaporation using a commercially available evaporator (Kentax, Germany) which allows for the loading of three sources. The sources can be shuttered individually (opening only one source, while blocking the others) or in any combination for co-deposition. Water cooling of the evaporator head ensures that only the desired pocket(s) is heated. Each evaporation pocket contains an independent heating coil and thermocouple for feedback controlled heating.

The powdered organic material is loaded into a small quartz tube closed at one end which is placed inside the heating elements of the evaporator. The evapo-

Material	$T_{outgassing}$	$T_{deposition}$	Density	Approx. rates
C_{60}	$220°C$	330°C	1.70 g/cm^3	0.0015-0.0088 ML/s
PTCDA	$200°C$	$300°C$	1.70g/cm^3	0.007-0.009 ML/s
PTCDI	$200°C$	$300°C$	1.70g/cm^3	$\sim$0.01Å/s
CuPc	$200°C$	$350 - 400°C$	1.62g/cm^3	$\sim$0.02Å/s

Table B.1: Parameters for molecular deposition by thermal evaporation

rator can be separately valved off and pumped for replacement of sources without venting the preparation chamber. In this case, a low temperature ($\sim$50–60°) bake out of the evaporator and vented lines is applied for 2–3 days before opening the evaporator to the UHV preparation chamber. If the full preparation chamber is vented, a standard bake-out ($\sim$150-200° max temperature, $\sim$65° at the molecule evaporator) is applied for 2–3 days or until UHV pressures can be obtained.

Each source is outgassed at the temperature indicated in table B.1 overnight ($\sim$12-14 hours) and raised to the evaporation temperature briefly before cooling down. This reduces the presence of volatile impurities in the source material as well as atmospheric contamination in the pocket. For deposition, the source pocket temperature is raised to the deposition temperature indicated in table B.1, and the rate is measured using a UHV compatible quartz crystal deposition monitor (Inficon, Switzerland). To obtain suitable rates without adjusting the deposition temperature the evaporator can be advanced or retracted, and the shutter position can be adjusted to optimize or reduce deposition.

B.2.2 Thermal gradient sublimation purification procedure

Thermal gradient sublimation is often used to purify organic materials. The procedure involves sublimating the starting material under high vacuum in a clean quartz tube (see schematic of figure B.3a). A thermal gradient along the length of the tube allows materials to redeposit on the walls of the tube in different regions according to the volatility of the material. The result is a separation of components of the starting material with non-volatile impurities left in the region where the starting material was placed, a crust of the purified material at a well defined location according to temperature, and volatile impurities deposited closer to the "cold" end of the tube or removed by the pumping station. For easier removal

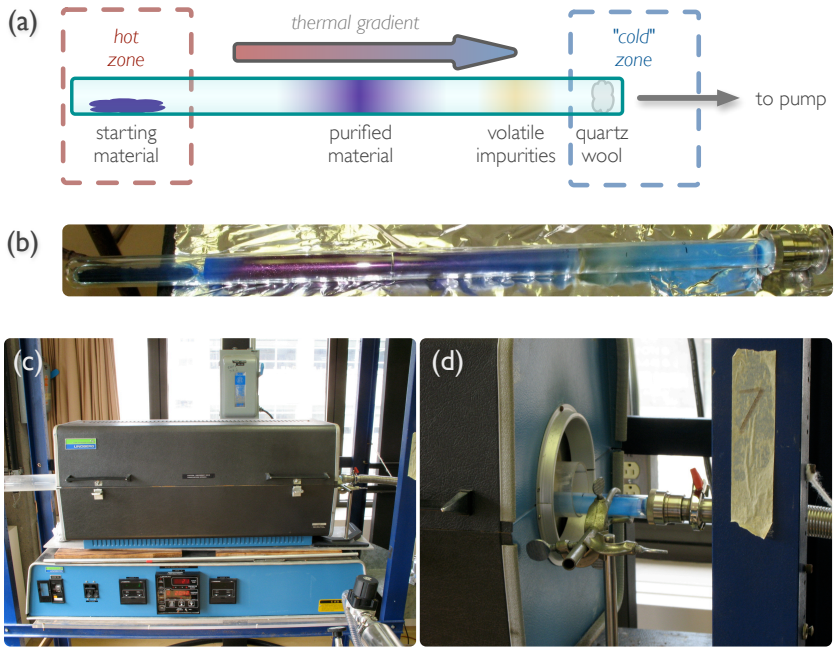

Figure B.3: Thermal gradient submlimation purification apparatus shown schematically (a) with a photo of the quartz rod showing purified CuPc (b) and photographs of the furnace (c) and connection to pumping station (d).

of the purified material, a glass sleeve insert is typically placed at the location where the desired material crystallizes. Also, a wad of quartz wool (not too tightly packed) is often placed in the end of the tube before the connection to the pumping station to further catch volatile material which might deposit in the pumping station otherwise. This method is described by Forrest [15] as well as others.

This method was used to further purify the starting CuPc material which was 95% pure from the commercial source (listed above). The resulting material was dominated by large crystals indicating high purity, and a region of a yellowish deposit appeared indicating the presence of a an impurity which was removed (see fig. B.3b). A quartz glass tube, sealed at one end, was attached to a pumping station by means of a glass-KF connector (see fig. B.3d). To ensure a good seal, a low vapour pressure (Apeizon L) grease was used on the seals connecting to the glass tube. The pumping station consisted of a small turbomolecular pump (Varian Turbo V70-LP) backed by a standard roughing pump, allowing base pressures of $\sim 2 \times 10^{-5}$Pa to be achieved. The CuPc starting material was heated to a measured temperature of $\sim$390° C for 2-4 weeks, starting from room temperature and gradually increasing to the final temperature. As with all other molecular materials used, an outgassing stage in UHV was still performed for further purification.

C

Derivation of Q-control signal (Ideal case)

Consider a damped, driven oscillator:

$$kx(t) + b\dot{x}(t) + m\ddot{x}(t) = F_D \tag{C.1}$$

with a driving signal of the form:

$$F_D = \underbrace{f_D e^{i\omega t}}_{drive} + \underbrace{f_q}_{amp\ Q-control}\underbrace{\left(\frac{\dot{x}(t)}{A\omega}\right)}_{velocity} \tag{C.2}$$

Assume the usual solution:

$$x(t) = Ae^{i(\omega t - \phi)} \tag{C.3}$$

we have:

$$-mA\omega^2 e^{i(\omega t-\phi)} + ibA\omega e^{i(\omega t-\phi)} + kAe^{i(\omega t-\phi)} = f_D e^{i(\omega t)} + if_q e^{i(\omega t-\phi)} \tag{C.4}$$

or making the usual definitions of $\gamma = b/m$, $\omega_0 = \sqrt{k/m}$ and simplifying:

$$-A\omega^2 + i\gamma A\omega + \omega_0^2 A = f_D e^{i\phi} + if_q \tag{C.5}$$

using Eulers relation we separate real:

$$-A\omega^2 + A\omega_0^2 = \frac{f_D}{m}\cos(\phi) \tag{C.6}$$

and imaginary:

$$\gamma A\omega - \frac{f_q}{m} = \frac{f_D}{m}\sin(\phi) \tag{C.7}$$

Solving for amplitude gives:

$$A(\omega) = \frac{\gamma\omega f_q + \sqrt{(\gamma\omega f_q)^2 - [(\gamma^2\omega^2 + (\omega_0^2 - \omega^2)^2)(f_q^2 - f_D^2)]}}{m[\gamma^2\omega^2 + (\omega_0^2 - \omega^2)^2]} \tag{C.8}$$

which reduces to the expression for amplitude of a driven oscillator if $f_q = 0$:

$$A(\omega) = \frac{f_D}{m\sqrt{\gamma^2\omega^2 + (\omega_0^2 - \omega^2)^2}} \tag{C.9}$$

Similarly solving for phase:

$$\tan\phi = \frac{\gamma\omega - f_q/Am}{\omega_0^2 - \omega^2} \tag{C.10}$$

which reduces to the expected expression in the absence of the Q-control signal:

$$\tan\phi = \frac{\gamma\omega}{\omega_0^2 - \omega^2} \tag{C.11}$$

The expression for the phase indicates a useful definition of an effective damping in the presence of a Q-control signal:

$$\gamma_{eff} = \gamma - \frac{f_q}{Am\omega} \tag{C.12}$$

or in terms of Q:

$$Q_{eff} = \frac{\omega_0}{\gamma - f_q/Am\omega} \tag{C.13}$$

allowing one to tune the quality factor, in principle either increasing or decreasing the Q, of the cantilever by adding an additional drive signal proportional to the velocity.

D

Parallel plate capacitor model for tip–surface potential difference

In quantitatively interpreting the results of CPD measurements on a dielectric substrate, the capacitive geometry of the system plays a role in determining the bias between the sample surface and the AFM tip apex. While the geometry of the real system is complex, this issue can be illustrated by a parallel plate model to show the reduction in potential difference across a thin vacuum gap when a thick dielectric is present.

For the case of parallel plates, we may treat the dielectric and the vacuum gap as two simple capacitors in parallel, one with a dielectric constant ϵ_1, and one with vacuum permittivity, ϵ_0:

$$\frac{1}{C_{eq}} = \frac{1}{C_1} + \frac{1}{C_{vac}} = \frac{d}{\epsilon_1 \epsilon_0 A} + \frac{s}{\epsilon_0 A} \tag{D.1}$$

$$C_{eq} = \frac{\epsilon_1 \epsilon_0 A}{d + \epsilon_1 s} \tag{D.2}$$

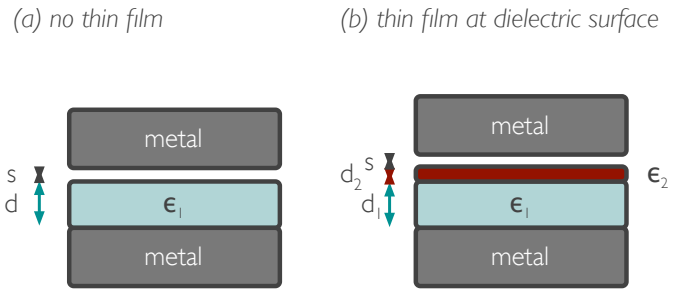

Figure D.1: Schematic of a parallel plate model to demonstrate the geometrical dependence of the relationship between tip–surface bias and applied bias for a dielectric substrate. Two situations are shown, a simple vacuum gap with a dielectric material (a), and a second thin dielectric film in contact with the thick dielectric material.

where d and s are the thicknesses of the dielectric and vacuum gap respectively as defined in fig. D.1. The charge on the capacitor system, which is the same on each component in parallel is:

$$Q = C_{eq}V = \frac{\epsilon_1\epsilon_0 A}{d + \epsilon_1 s}V \tag{D.3}$$

where V is the bias applied across both capacitors. We can then determine the potential difference across the vacuum capacitor only, representing the potential difference between the top surface of our sample and the apex of the tip, in terms of the total applied bias:

$$V_{vac} = \frac{Q}{C_{vac}} = \frac{\epsilon_1 s}{d + \epsilon_1 s}V \tag{D.4}$$

However, since the single crystal dielectric substrates used in these studies are typically of the order of a few mm in dimensions, and the gap between tip and sample usually of the order of a few nm, we can simplify by approximating $s \ll d$, yielding:

$$V_{vac} \simeq \epsilon_1 \frac{s}{d}V \tag{D.5}$$

showing that the actual tip–surface bias is scaled by a geometrical factor from the applied bias.

Following the same treatment with an additional very thin dielectric film as shown in fig. D.1b, for example our molecular islands or monolayers, yields:

$$V_{vac} = \frac{s\epsilon_1\epsilon_2}{\epsilon_2 d_1 + \epsilon_1 d_2 + \epsilon_1\epsilon_2 s}V \tag{D.6}$$

which when making a similar approximation that $s \ll d_1$ and $d_2 \ll d_1$ yeilds the same result as equation D.5.

While this later result may seem odd, it is a consequence of our approximation of parallel plates. In the geometry of the AFM, the tip is a very small point, and the highest density of electric field lines will be in the region near the tip, ie. in the gap and at the upper surface of the dielectric. Thus there will be a greater influence of materials located in this region than is indicated by the parallel plate approximation given here. Nevertheless, the dependence on geometry of the actual potential difference at the surface of a dielectric would need to be taken into

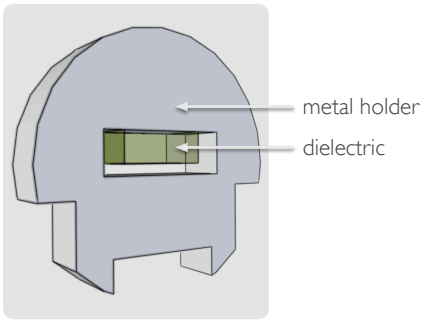

Figure D.2: JEOL cleaving holder and sample geometry. Ideally, only a simple back plane would be held at the sample bias voltage for easier interpretation.

account for quantitative comparison of CPD measurements from different systems on dielectric substrates.

Ideally, in order to most easily take this into account, a dielectric substrate as thin as would be experimentally feasible with a simple metal back plane would be used. The current experimental apparatus utilizes a metal sample holder which surrounds the single crystal insulating samples for the purposes of facilitating cleaving of the sample. This further complicates the characterization of the capacitance of the system as all dimensions of the sample and the position of the tip relative to the edges would also likely be of importance.

E

Determination of overlayer lattice parameters

E.1 Lattice correction: Transformation based on known lattice

For images where an overlayer structure is observed simultaneously with the known structure of the substrate, the known substrate lattice can be used as a calibration to correct for errors in the AFM imaging such as piezo creep, drift, non-linearities and cross-talk between x and y signals. The following gives a derivation of the formulas used for calibration to a square or rectangular lattice substrate, as is the case for alkali halides. The same derivation can be performed for lattices with angles other than 90° , however the resulting formulas are somewhat more complicated. We start by considering the errors in the AFM imaging as shear and stretch transformations:

$$\mathbf{T} = \mathbf{T}_{shear} \times \mathbf{T}_{stretch} = \begin{bmatrix} 1 & \sin(\alpha - \alpha') \\ 0 & \cos(\alpha - \alpha') \end{bmatrix} \times \begin{bmatrix} \frac{a_1'}{a_1} & 0 \\ 0 & \frac{a_2'}{a_2} \end{bmatrix} = \begin{bmatrix} \frac{a_1'}{a_1} & \frac{a_2'}{a_2}\sin(\alpha - \alpha') \\ 0 & \frac{a_2'}{a_2}\cos(\alpha - \alpha') \end{bmatrix} \tag{E.1}$$

which when inverted gives the correction to be applied to the measured overlayer lattice:

$$\mathbf{T}^{-1} = \begin{bmatrix} \frac{a_1}{a_1'} & -\frac{a_1}{a_1'}\tan(\alpha - \alpha') \\ 0 & \frac{a_2}{a_2'}\sec(\alpha - \alpha') \end{bmatrix} \tag{E.2}$$

where a_1, a_2, α are the known lattice parameters of the substrate, and a_1', a_2', α' are the measured lattice constants from the image.

Assuming that the geometrical errors in the image are uniform over the image, we can apply this transformation matrix to the measured overlayer lattice vectors to

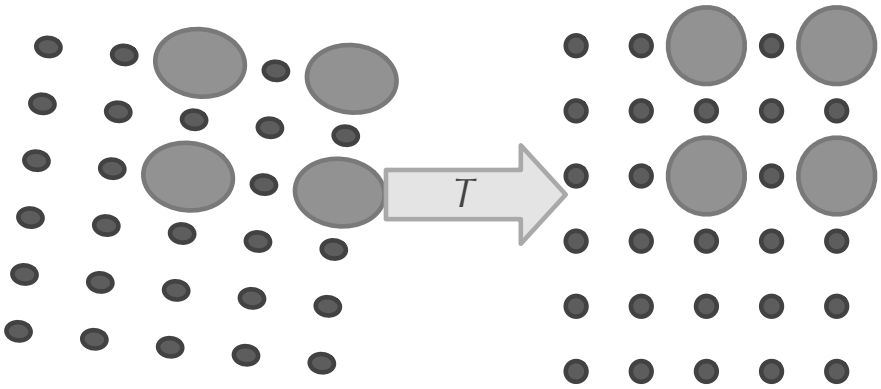

Figure E.1: Example of a rotated and stretched lattice which might be representative of an off-axis scan (sample misaligned) with a constant drift. Using the known substrate lattice a correction can be made to the measured lattice vectors of the overlayer.

arrive at the corrected vector set. We take the measured overlayer lattice vectors, decomposed into x and y components:

$$b_{1x} = |\vec{b_1}|\cos(\theta) \tag{E.3}$$
$$b_{1y} = |\vec{b_1}|\sin(\theta) \tag{E.4}$$
$$b_{2x} = |\vec{b_2}|\cos(\theta+\beta) \tag{E.5}$$
$$b_{2y} = |\vec{b_2}|\sin(\theta+\beta) \tag{E.6}$$

where b_1, b_2 are the magnitudes of the two lattice vectors, β is the angle between them, and θ is the angle between $\vec{a_1}$ and $\vec{b_1}$. These components have the errors:

$$\delta b_{1x} = \sqrt{(\cos(\theta)\delta b_1)^2 + (|b_1|\sin(\theta)\delta\theta)^2} \tag{E.7}$$
$$\delta b_{1y} = \sqrt{(\sin(\theta)\delta b_1)^2 + (|b_1|\cos(\theta)\delta\theta)^2} \tag{E.8}$$
$$\delta(\theta+\beta) = \sqrt{\delta\theta^2 + \delta\beta^2} \tag{E.9}$$
$$\delta b_{2x} = \sqrt{(\cos(\theta+\beta)\delta b_2)^2 + (|b_2|\sin(\theta+\beta)\delta(\theta+\beta))^2} \tag{E.10}$$
$$\delta b_{2y} = \sqrt{(\sin(\theta+\beta)\delta b_2)^2 + (|b_2|\cos(\theta+\beta)\delta(\theta+\beta))^2} \tag{E.11}$$

Applying the transformation matrix, $\mathbf{T} \times \vec{b_i}$, we find each of the corrected lattice vectors:

$$\vec{b_i'} = \begin{bmatrix} \frac{a_1}{a_1'} b_x - \frac{a_1}{a_1'} \tan(\alpha - \alpha') b_y \\ \frac{a_2}{a_2'} \sec(\alpha - \alpha') b_y \end{bmatrix} \tag{E.12}$$

With error:

$$\delta\vec{b_i'} = \begin{bmatrix} \frac{a_1}{a_1'} \sqrt{(\frac{b_x - b_y \tan(\alpha-\alpha')}{a_1'})^2 (\delta a_1')^2 + (\delta b_x)^2 + (b_y \sec^2(\alpha - \alpha'))^2 (\delta\alpha)^2 + \tan^2(\alpha - \alpha')(\delta b_y)^2} \\ \frac{a_2}{a_2'} b_y \sec(\alpha - \alpha') \sqrt{(\frac{\delta a_2'}{a_2'})^2 + (\frac{\delta b_y}{b_y})^2 + \tan^2(\alpha - \alpha')(\delta\alpha)^2} \end{bmatrix} \tag{E.13}$$

or:

$$\delta\vec{b_i'} = \begin{bmatrix} \frac{a_1}{a_1'} \sqrt{(\frac{b_x - b_y \tan(\alpha-\alpha')}{a_1'})^2 (\delta a_1')^2 + (\delta b_x)^2 + (b_y \sec^2(\alpha - \alpha'))^2 (\delta\alpha)^2 + \tan^2(\alpha - \alpha')(\delta b_y)^2} \\ b_y' \sqrt{(\frac{\delta a_2}{a_2'})^2 + (\frac{\delta b_y}{b_y})^2 + \tan^2(\alpha - \alpha')(\delta\alpha)^2} \end{bmatrix} \tag{E.14}$$

From this the magnitudes of each of the lattice vectors and their errors are given by:

$$|\vec{b_i'}| = \sqrt{b_x'^2 + b_y'^2} \tag{E.15}$$

$$\delta|\vec{b_i'}| = \frac{1}{|\vec{b_i'}|} \sqrt{(b_{ix}' \delta b_{ix}')^2 + (b_{iy}' \delta b_{iy}')^2} \tag{E.16}$$

The angles β and θ are given by:

$$\beta = \arccos(\frac{\vec{b_1} \cdot \vec{b_2}}{|\vec{b_1}||\vec{b_2}|}) \tag{E.17}$$

$$\theta = \arctan(\frac{b_{1y}}{b_{1x}}) \tag{E.18}$$

and the error in the angles β and θ are:

$$\delta\beta = \frac{1}{|\vec{b_1}||\vec{b_2}|\sqrt{1-\cos\beta}} \times \sqrt{(b_{2x}\delta b_{1x})^2 + (b_{1x}\delta b_{2x})^2 + (b_{2y}\delta b_{1y})^2 + (b_{1y}\delta b_{2y})^2 + (|\vec{b_2}|\cos(\beta)\delta|\vec{b_1}|)^2 + (|\vec{b_1}|\cos(\beta)\delta|\vec{b_2}|)^2} \tag{E.19}$$

$$\delta\theta = \frac{b_{1y}}{b_{1x}} \frac{1}{1+(b_{1y}/b_{1x})^2} \sqrt{(\frac{\delta b_{1x}}{b_{1x}})^2 + (\frac{\delta b_{1y}}{b_{1y}})^2} \tag{E.20}$$

Thus, the resulting overlayer lattice vectors should be free of the common systematic errors present in SPM measurements by exploiting the known lattice as an image-by-image calibration. This allows much more accurate measurement of overlayer lattice vectors which is crucial in cases where large epitaxial cells appear.

E.2 Overlayer matrix calculation including errors

The positions of overlayer atoms or molecules can be expressed in terms of a matrix notation. While Wood's notation (eg: 2×2 where each overlayer atom is positioned on every second substrate atom) is commonly used when the lattices exhibit the same symmetry, when more complex relations between the overlayer and the substrate arise, this matrix notation must be used. The overlayer matrix is defined

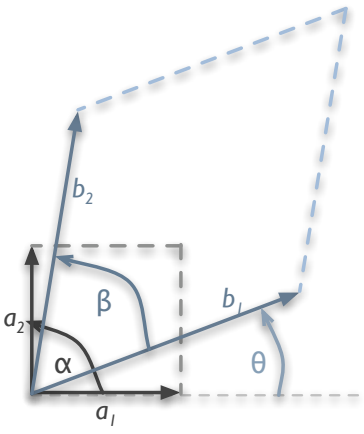

Figure E.2: Definition of notation used for substrate and overlayer lattices, where the $\mathbf{a_i}$ and α correspond to the substrate, and the $\mathbf{b_i}$ and β the overlayer, with θ as the angle between $\mathbf{a_1}$ and $\mathbf{b_1}$

as the transformation of the substrate lattice vectors to the overlayer lattice vectors [31]:

$$\begin{bmatrix} \mathbf{b}_1 \\ \mathbf{b}_2 \end{bmatrix} = [\mathbf{C}] \begin{bmatrix} \mathbf{a}_1 \\ \mathbf{a}_2 \end{bmatrix} = \begin{bmatrix} p & q \\ r & s \end{bmatrix} \begin{bmatrix} \mathbf{a}_1 \\ \mathbf{a}_2 \end{bmatrix} \tag{E.21}$$

where the $\mathbf{a_i}$ correspond to the substrate lattice vectors and the $\mathbf{b_i}$ to the overlayer lattice vectors as shown in figure E.2.

The matrix elements can be expressed in terms of the magnitudes of the lattice vectors and the angles between them [31] as can be found by the methods above:

$$p = \frac{b_1 \sin(\alpha - \theta)}{a_1 \sin(\alpha)} \tag{E.22}$$

$$q = \frac{b_1 \sin(\theta)}{a_2 \sin(\alpha)} \tag{E.23}$$

$$r = \frac{b_2 \sin(\alpha - \theta - \beta)}{a_1 \sin(\alpha)} \tag{E.24}$$

$$s = \frac{b_2 \sin(\theta + \beta)}{a_2 \sin(\alpha)} \tag{E.25}$$

where the angles α, β, and θ are shown in figure E.2.

Given that the substrate lattice is known to much greater accuracy than the overlayer (ie. error in the substrate lattice is assumed to be negligible), the errors on each of the matrix elements are given by:

$$\delta p = p\sqrt{\cot^2(\alpha - \theta)(\delta\theta)^2 + (\frac{\delta b_1}{b_1})^2} \tag{E.26}$$

$$\delta q = q\sqrt{\cot^2(\theta)(\delta\theta)^2 + (\frac{\delta b_1}{b_1})^2} \tag{E.27}$$

$$\delta r = r\sqrt{\cot^2(\alpha - \theta - \beta)(\delta\theta)^2 + \cot^2(\alpha - \theta - \beta)(\delta\beta)^2 + (\frac{\delta b_2}{b_2})^2} \tag{E.28}$$

$$\delta s = s\sqrt{\cot^2(\theta + \beta)(\delta\theta)^2 + \cot^2(\theta + \beta)(\delta\beta)^2 + (\frac{\delta b_2}{b_2})^2} \tag{E.29}$$

Given the known error on each of the calculated matrix elements, an integer, fractional or irrational number can potentially be ascribed to each, although unique assignment is often not possible for large coincident unit cells. Using the matrix **C**, the type of structural relationship can be easily classified according to the "gram-

mar of epitaxy" put forth by Hooks et al. [31] as follows:

Commensurism (also referred to as point-on-point coincidence): All matrix elements of C are integers, indicating that each overlayer lattice point lies on a substrate lattice point. For inorganic systems, this is the most common case where an "epitaxial" relationship is described. Energetically, a commensurate lattice leads to a minimization of the substrate–overlayer interaction. Since this situation usually arises when the substrate–overlayer interaction dominates, the positions of the deposit lattice points will be determined by the surface potential.

Coincidence-I (also referred to as point-on-line coincidence, or "quasi-epitaxy" [178]): At least two of the matrix elements of C are integers confined to a single column of the matrix. This defines the situation where every overlayer lattice point lies on at least one primitive lattice line of the substrate, hence the alternate terminology of "point-on-line (POL)" coincidence. Coincidence-I can be subdivided into two catagories:

Coincidence-IA : All matrix elements are rational numbers. In this case a supercell can be constructed, defining a phase coherent registry with the lattice, even though some overlayer lattice points do not lie on lattice points of the substrate. In inorganic systems this is typically referred to simply as "coincidence". In terms of the substrate–overlayer interaction, the situation of coincidence-IA is energetically less favorable than commensurism as some of the overlayer lattice points will be out of phase with the substrate lattice, even though a longer range phase coherence still exists. Of course, when the full set of interactions is considered, this may still be an energetic minimum for the system.

Coincidence-IB : At least one of the matrix elements of C is an irrational number. Although every overlayer lattice point lies on one primitive lattice line of the substrate, the irrational matrix element produces an incommensurate relationship in one direction. Due to this incommensurate relation in one direction, a finite supercell *cannot* be constructed. (Note: If the supercell size exceeds the area investigated experimentally, coincidence-IA will be indistinguishable from coincidence-IB.)

Coincidence-II (also called "geometrical coincidence"): All matrix elements are rational, but no column consists of integers. In this case a supercell can still be constructed, but not all of the lattice points of the overlayer lie on at least one substrate lattice line. Although this case violates the reciprocal space criterion ($\mathbf{b}_1^* = m\mathbf{a}_1^*$, where m is an integer), it is still considered coincidence due to the presence of a lattice registry (supercell can be constructed). Again, coincidence-II is less energetically favorable in terms of the overlayer–substrate interaction than the aforementioned cases.

Incommensurism : The matrix **C** has at least one irrational element and neither column consists of integers. In this case there is no finite size supercell which can be constructed, and hence no distinct lattice registry between the overlayer and the substrate. Incommensurism is the least favorable in terms of the interface energy and will occur in the absence of an available phase-coherent structure.

F

DFT calculations of PTCDA adsorption on NaCl

THE FOLLOWING SECTION IS BASED ON TEXT FROM:

S.A. Burke, W. Ji, J.M. Mativetsky, J.M. Topple, S. Fostner, H.-J. Gao, H. Guo and P. Grütter. Strain Induced Dewetting of a Molecular System: Bimodal Growth of PTCDA on NaCl. *Phys. Rev. Lett.* **100**:186104, 2008.

(Supporting Information, Part 2: calculations by Wei Ji.)

Computational methods: All first-principles calculations were based on Density Functional Theory (DFT), a Perdew-Burke-Ernzerhof (PBE) [179] Generalized Gradient Approximation (GGA) for the exchange-correlation energy, Projector Augmented Waves (PAW) [180, 181] and a plane-wave basis set with its kinetic energy cutoff up to 400 eV, as implemented in the Vienna abi-initio Simulation Package (VASP) [182, 183]. The semi-core 2p electron of Na was treated as valance electron. Only the Gamma point is adopted to sample the surface Brillouin Zone, since the wave-function overlap between Na+ and Cl-, and PTCDA molecules is rather small. All aspects of the calculation were carefully tested to ensure the total energy convergence of 1 meV per atom. Five NaCl layers, separated by a vacuum layer of seven NaCl layers, were employed to model the surface, while two button layers were kept fixed during the structure relaxation. All other atoms were fully relaxed until the net force on every relaxed atom is less than 0.01 eV/Å. A p3x3 supercell was adopted to model the monolayer structure of PTCDA/NaCl(001) interface.
Calculated total energy and fully relaxed structures: Four possible adsorption sites were considered in the calculation. Using the central benzene ring of PTCDA as a reference, these four possible adsorption sites are, as shown in Fig. F.1, Na-Top

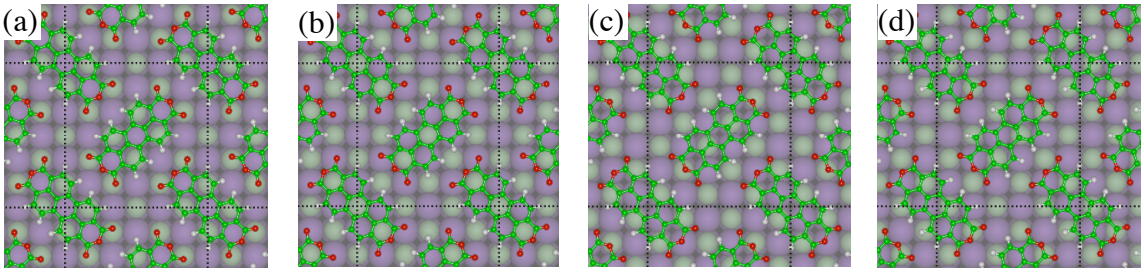

Figure F.1: Four possible adsorption sites.

(a), Cl-Top (b), Bridge (c), and Na-Cl-Bridge (d). The calculated total energy shows that the Cl-Top site is the most stable one, which is over 0.2 eV more stable than other sites. In the fully relaxed structure of the Cl-Top site, the optimized PTCDA molecule shows a flat geometry, in contrast to how it behaves as a bent molecular backbone on noble metal surfaces [184]. The distance measured between carboxylic O and the Na atom underneath is 3.53 Å, is consistent with experimentally measured value of 3.4 Å.

Interaction mechanism and the validity of using molecular mechanism calculation: The differential charge density (DCD) is defined as $\rho_{DCD} = \rho_{Total} - \rho_{PTCDA} - \rho_{NaCl}$, which directly reveals the information of adsorption-induced chemical bond formation. Figure F.2 shows the calculated DCD of PTCDA on NaCl. It directly shows that there is almost no charge transfer, only charge redistribution occurs at the PTCDA-NaCl interface. This observation thus strongly suggests that the interaction between PTCDA and NaCl substrate is mainly through the electrostatic interaction, e.g. Coulomb interaction. It turns out that there is no strong chemical interaction between PTCDA and NaCl(001). This statement is also supported by projected density of states analysis. So that the Molecular Mechanism (MM) calculation could describe the monolayer structures equally well as DFT. As proof, the suggested most stable configuration by MM is the same one as DFT suggests,as is also consistent with the experimental observation. Including van der Waals interactions, the performance of MM in calculating molecular multi-layers should be much better than DFT.

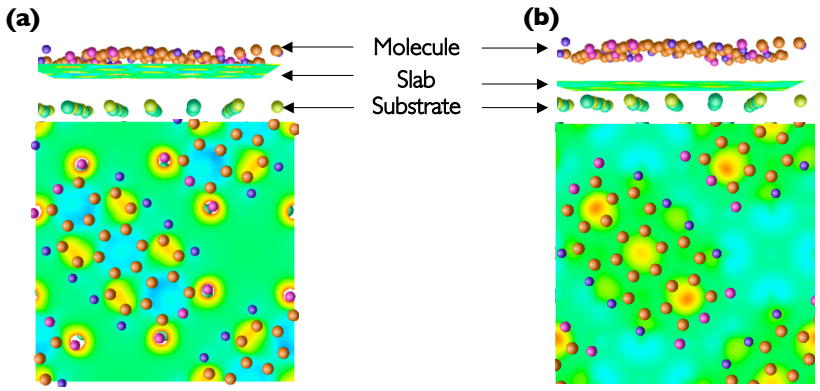

Figure F.2: Side view (upper) and top view (lower) of calculated differential charge densities between PTCDA and NaCl surface, being closer to the molecule (a) and to the substrate (b).

Bibliography

[1] Bharat Bhushan. *Springer Handbook of Nanotechnology*, chapter 1: Introduction to Nanotechnology. Springer, Berlin, 2007.

[2] Numerical figures taken from Intel document "60 years of the transistor: 1947–2007", available at http://www.intel.com/technology/timeline.pdf.

[3] A. Correia, M. Perez, J. J. Saenz, and P. A. Serena. Nanoscience and nanotechnology - driving research and applications. *Physica Status Solidi-Rapid Research Letters*, 1(4):A68–A72, 2007.

[4] The US National Nanotechnology Initiative website gives a host of examples of nanotechnologies: http://www.nano.gov/.

[5] Directed from NNI: Smalltimes article "Nanotennis anyone? Tiny, sporty materials have their day on court": http://www.smalltimes.com/Articles/Article_Display.cfm?ARTICLE_ID=269245&p=109.

[6] Directed from NNI: Cornell University news release "CU biodegradable wipe would quickly detect biohazards, from avian flu to E. coli": http://www.news.cornell.edu/stories/Sept06/napkin.biohazard.ssl.html.

[7] Paolo Fortina, Larry J. Kricka, David J. Graves, Jason Park, Terry Hyslop, Felicia Tam, Naomi Halas, Saul Surrey, and Scott A. Waldman. Applications of nanoparticles to diagnositcs and therapeutics in colorectal cancer. *Trends in Biotechnology*, 25(4):145–152, 2007.

[8] Arich Aviram and Mark A. Ratner. Molecular rectifiers. *Chem. Phys. Lett.*, 29(2):277–283, 1974.

[9] G. Binnig and H. Rohrer. Scanning tunneling microscope. *Helvetica Physica Acta*, 55:726–735, 1982.

[10] G. Binnig, H. Rohrer, Ch. Gerber, and E. Weibel. 7×7 reconstruction on Si(111) resolved in real space. *Phys. Rev. Lett.*, 50(2):120–123, 1983.

[11] G. Binnig and C.F. Quate. Atomic force microscope. *Phys. Rev. Lett.*, 56(9):930–933, 1986.

[12] G. Binnig, Ch. Gerber, E. Stoll, T.R. Albrecht, and C.F. Quate. Atomic resolution with atomic force microscope. *Europhysics Letters*, 3(12):1281–1286, 1987.

[13] S.M. Lindsay and M.A. Ratner. Molecular transport junctions: Clearing mists. *Advanced Materials*, 19:23–31, 2007.

[14] M. Galperin, M. A. Ratner, A. Nitzan, and A. Troisi. Nuclear coupling and polarization in molecular transport junctions: Beyond tunneling to function. *Science*, 319(5866):1056–1060, 2008.

[15] S.R. Forrest. Ultrathin organic films grown by organic molecular beam deposition and related techniques. *Chem. Rev.*, 97:1793–1896, 1997.

[16] G. Horowitz. Organic field-effect transistors. *Adv. Mater.*, 10(5):365–377, 1998.

[17] C.D. Dimitrakopoulos and P.R.L. Malenfant. Organic thin film transistors for large area electronics. *Adv. Mater.*, 14:99, 2002.

[18] J.R. Sheats. Manufacturing and commercialization issues in organic electronics. *J. Mater. Res.*, 19:1974–1989, 2004.

[19] N. Karl. Charge carrier transport in organic semiconductors. *Synthetic Metals*, 133–134:649–657, 2003.

[20] G. V. Nazin, X. H. Qiu, and W. Ho. Visualization and spectroscopy of a metal-molecule-metal bridge. *Science*, 302(5642):77–81, 2003.

[21] J. Repp, G. Meyer, S. Paavilainen, F. E. Olsson, and M. Persson. Imaging bond formation between a gold atom and pentacene on an insulating surface. *Science*, 312(5777):1196–1199, 2006.

[22] L. Venkataraman, J. E. Klare, C. Nuckolls, M. S. Hybertsen, and M. L. Steigerwald. Dependence of single-molecule junction conductance on molecular conformation. *Nature*, 442(7105):904–907, 2006.

[23] L. Venkataraman, J. E. Klare, I. W. Tam, C. Nuckolls, M. S. Hybertsen, and M. L. Steigerwald. Single-molecule circuits with well-defined molecular conductance. *Nano Letters*, 6(3):458–462, 2006.

[24] J. L. Xia, I. Diez-Perez, and N. J. Tao. Electron transport in single molecules measured by a distance-modulation assisted break junction method. *Nano Letters*, 8(7):1960–1964, 2008.

[25] J. Hihath and N. Tao. Rapid measurement of single-molecule conductance. *Nanotechnology*, 19(26):265204, 2008.

[26] S. R. Forrest. The path to ubiquitous and low-cost organic electronic appliances on plastic. *Nature*, 428(6986):911–918, 2004.

[27] M. Szymonski, J. Kolodziej, B. Such, P. Piatkowski, P. Struski, P. Czuba, and F. Krok. Nano-scale modification of ionic surfaces induced by electronic transitions. *Progress in Surface Science*, 67:123–138, 2001.

[28] Maria Veronica Tiba. *Organo-metallic structures for spintronic applications*. PhD thesis, Technische Universiteit Eindhoven, 2005.

[29] A. Ueda, R. Mu, Y. S. Tung, M. H. Wu, A. Zavalin, P. W. Wang, and D. O. Henderson. Optically measured diffusion constants of oxygen vacancies in mgo. *Journal of Physics-Condensed Matter*, 13(23):5535–5544, 2001.

[30] Andrew Zangwill. *Physics at Surfaces*. Cambridge University Press, Cambridge, 1988.

[31] D. E. Hooks, T. Fritz, and M. D. Ward. Epitaxy and molecular organization on solid substrates. *Advanced Materials*, 13(4):227–241, 2001.

[32] F. Rosei, M. Schunack, Y. Naitoh, P. Jiang, A. Gourdon, E. Laegsgaard, I. Stensgaard, C. Joachim, and F. Besenbacher. Properties of large organic molecules on metal surfaces. *Progress in Surface Science*, 71:95–146, 2003.

[33] Laurent Nony, Enrico Gnecco, and Ernst Meyer. *Applied Scanning Probe Methods III: Characterization*, chapter 16: Investigation of Organic Supramolecules by Scanning Probe Microscopy in Ultra-high Vacuum. Springer, Berlin, 2006.

[34] J. Repp and G. Meyer. Scanning tunneling microscopy of adsorbates on insulating films. from the imaging of individual molecular orbitals to the manipulation of the charge state. *Applied Physics a – Materials Science & Processing*, 85(4):399–406, 2006.

[35] P. Liljeroth, J. Repp, and G. Meyer. Current-induced hydrogen tautomerization and conductance switching of naphthalocyanine molecules. *Science*, 317(5842):1203–1206, 2007.

[36] N. Ogawa, G. Mikaelian, and W. Ho. Spatial variations in submolecular vibronic spectroscopy on a thin insulating film. *Physical Review Letters*, 98(16):166103, 2007.

[37] M. Sterrer, T. Risse, M. Heyde, H. P. Rust, and H. J. Freund. Crossover from three-dimensional to two-dimensional geometries of au nanostructures on thin MgO(001) films: A confirmation of theoretical predictions. *Physical Review Letters*, 98(20):206103, 2007.

[38] M. Kulawik, N. Nilius, and H. J. Freund. Influence of the metal substrate on the adsorption properties of thin oxide layers: Au atoms on a thin alumina film on NiAl(110). *Physical Review Letters*, 96(3):036103, 2006.

[39] Shin–ichi Kitamura and Masashi Iwatsuki. Observation of 7×7 reconstructed structure on the Silicon (111) surface using ultrahigh vacuum noncontact atomic force microscopy. *Jpn. J. Appl. Phys.*, 34:L145–L148, 1995.

[40] F. J. Giessibl. Atomic resolution of the Silicon(111) 7×7 surface by Atomic Force Microscopy. *Science*, 267:68–71, 1995.

[41] M. Bammerlin, R. Lüthi, and et. al. True atomic resolution on the surface of an insulator via ultra-high vacuum dynamic force microscopy. *Probe Microscopy*, 1:3–9, 1997.

[42] R. Bennewitz, O. Pfeiffer, S. Schär, V. Barwich, E. Meyer, and L.N. Kantorovich. Atomic corrugation in nc-AFM of alkali halides. *Appl. Surf. Sci.*, 188, 2002.

[43] C. Barth and C. R. Henry. Atomic resolution imaging of the (001) surface of uhv cleaved mgo by dynamic scanning force microscopy. *Physical Review Letters*, 91(19):196102, 2003.

[44] R. Hoffmann, L.N. Kantorovich, A. Baratoff, H.J. Hug, and H.-J. Güntherodt. Sublattice identification in scanning force microscopy on alkali halide surfaces. *Phys. Rev. Lett.*, 92(14):146103, 2004.

[45] M.A. Lantz, R. Hoffmann, A.S. Foster, A. Baratoff, H.J. Hug, H. R. Hidber, and H.-J. Güntherodt. Site-specific force-distance characteristics on NaCl(001): Measurements versus atomistic simulations. *Phys. Rev. B*, 74:245426, 2006.

[46] C. Barth and C. R. Henry. Surface double layer on (001) surfaces of alkali halide crystals: A scanning force microscopy study. *Physical Review Letters*, 98(13):136804, 2007.

[47] S. Maier, O. Pfeiffer, T. Glatzel, E. Meyer, T. Filleter, and R. Bennewitz. Asymmetry in the reciprocal epitaxy of nacl and kbr. *Physical Review B*, 75(19):195408, 2007.

[48] F. Ostendorf, S. Torbrugge, and M. Reichling. Atomic scale evidence for faceting stabilization of a polar oxide surface. *Physical Review B*, 77(4):041405(R), 2008.

[49] T. Fukuma, K. Kobayashi, K. Noda, K. Ishida, T. Hoiruchi, H. Yamada, and K. Matsushige. Molecular-scale non-contact AFM studies of ferroelectric organic thin films epitaxially grown on alkali halides. *Surface Science*, 516:103–108, 2002.

[50] L. Nony, E. Gnecco, A. Baratoff, A. Alkauskas, R. Bennewitz, O. Pfeiffer, S. Maier, A. Wetzel, E. Meyer, and Ch. Gerber. Observation of individual molecules trapped on a nanostructured insulator. *NanoLetters*, 4:2185, 2004.

[51] S. A. Burke, J. M. Mativetsky, R. Hoffmann, and P. Grütter. Nucleation and submonolayer growth of C_{60} on KBr. *Phys. Rev. Lett.*, 94:096102, 2005.

[52] O. Pfeiffer, E. Gnecco, L. Zimmerli, S. Maier, E. Meyer, L. Nony, R. Bennewitz, F. Deiderich, H. Fang, and D. Bonifazi. Force microscopy on insulators: Imaging of organic molecules. *Journal of Physics: Conference Series*, 19:166–174, 2005.

[53] T. Kunstmann, A. Schlarb, M. Fendrich, Th. Wagner, R. Möller, and R. Hoffmann. Dynamic force microscopy of 3,4,9,10-perylenetetracarboxylic dianhydride on KBr(001). *Phys. Rev. B*, 71:121403(R), 2005.

[54] J. M. Mativetsky, S. A. Burke, S. Fostner, and P. Grutter. Templated growth of 3,4,9,10-perylenetetracarboxylic dianhydride molecules on a nanostructured insulator. *Nanotechnology*, 18(10):105303, 2007.

[55] S. A. Burke, J. M. Mativetsky, S. Fostner, and P. Grutter. C_{60} on alkali halides: Epitaxy and morphology studied by noncontact AFM. *Phys. Rev. B*, 76(3):035419, 2007.

[56] S. A. Burke, W. Ji, J. M. Mativetsky, J.M. Topple, S. Fostner, H.-J. Gao, H. Guo, and P. Grutter. Strain induced dewetting of a molecular system: Bimodal growth of PTCDA on NaCl. *Physical Review Letters*, 100:186104, 2008.

[57] T. Dienel, C. Loppacher, S. C. B. Mannsfeld, R. Forker, and T. Fritz. Growth-mode-induced narrowing of optical spectra of an organic adlayer. *Advanced Materials*, 20(5):959, 2008.

[58] R. Stomp, Y. Miyahara, S. Schaer, Q. Sun, H. Guo, P. Grutter, S. Studenikin, P. Poole, and A. Sachrajda. Detection of single-electron charging in an individual inas quantum dot by noncontact atomic-force microscopy. *Physical Review Letters*, 94(5):056802, 2005.

[59] U. Zerweck, Ch. Loppacher, and L.M. Eng. Ordered growth and local work-function measurements of tris(8-hydroxyquinoline) aluminium on ultrathin KBr films. *Nanotechnology*, 17:S107–S111, 2006.

[60] C. Loppacher, U. Zerweck, L. M. Eng, S. Gemming, G. Seifert, C. Olbrich, K. Morawetz, and M. Schreiber. Adsorption of PTCDA on a partially KBr covered Ag(111) substrate. *Nanotechnology*, 17(6):1568–1573, 2006.

[61] John A. Venables. *Introduction to Surface and Thin Film Processes*. Cambridge University Press, Cambridge, 2000.

[62] G. Witte, K. Hänel, S. Söhnchen, and Ch. Wöll. Growth and morphology of thin films of aromatic molecules on metals: the case of perylene. *Appl. Phys. A*, 82:477–455, 2006.

[63] F. Silly and M. R. Castell. Bimodal growth of Au on $SrTiO_3$(001). *Phys. Rev. Lett.*, 96(8):086104, 2006.

[64] D. Kafer, L. Ruppel, and G. Witte. Growth of pentacene on clean and modified gold surfaces. *Phys. Rev. B*, 75(8):085309, 2007.

[65] S. Rath and H. Port. Dewetting of thin UHV-deposited organic films. *Chem. Phys. Lett.*, 421:152–156, 2006.

[66] S. Kowarik, A. Gerlach, and F. Schreiber. Organic molecular beam deposition: fundamentals, growth dynamics, and *in situ* studies. *Journal of Physics: Condensed Matter*, 20:184005, 2008.

[67] J.H. DeBoer. Atomic forces and adsorption. *Advances in Colloid Science*, 3:1–66, 1950.

[68] F. Schreiber. Organic molecular beam deposition: Growth studies beyond the first monolayer. *Physica Status Solidi a-Applied Research*, 201(6):1037–1054, 2004.

[69] D. Y. Zhong, M. Hirtz, W. C. Wang, R. F. Dou, L. F. Chi, and H. Fuchs. Kinetics of island formation in organic film growth. *Physical Review B*, 77(11):113404, 2008.

[70] A. Moll, A. Hildebrandt, H.P. Lenhof, and O. Kohlbacher. Ballview: an object-oriented molecular visualization and modeling framework. *J Comput Aided Mol Des.*, 19(11):791–800, 2005.

[71] K. Momma and F. Izumi. Vesta: a three-dimensional visualization system for electronic and structural analysis. *J. Appl. Crystallogr.*, 41:653–658, 2008.

[72] Bharat Bhushan and Othmar Marti. *Springer Handbook of Nanotechnology*, chapter 22: Scanning Probe Microscopy – Principle of Operation, Instrumentation, and Probes. Springer, Berlin, 2007.

[73] Image taken from Canadian National Institute for the Blind website: http://cnib.ca.

[74] Roland Bennewitz. Friction force microscopy. *materials today*, pages 42–48, 2005.

[75] E. Gnecco, R. Bennewitz, and E. Meyer. Abrasive wear on the atomic scale. *Phys. Rev. Lett.*, 88(21):215501, May 2002.

[76] N. Oyabu, P. Pou, Y. Sugimoto, P. Jelinek, M. Abe, S. Morita, R. Perez, and O. Custance. Single atomic contact adhesion and dissipation in dynamic force microscopy. *Physical Review Letters*, 96(10):106101, 2006.

[77] John E. Sader, Ian Larson, Paul Mulvaney, and Lee R. White. Method for the calibration of atomic force microscope cantilevers. *Review of Scientific Instruments*, 66(7):3789–3798, 1995.

[78] John E. Sader, James W. M. Chon, and Paul Mulvaney. Calibration of rectangular atomic force microscope cantilevers. *Review of Scientific Instruments*, 70(10):3967–3969, 1999.

[79] S. Morita, R. Weisendanger, and E. Meyer. *Non-contact atomic force microscopy*. Springer, Berlin, 2002.

[80] U. Zerweck, C. Loppacher, T. Otto, S. Grafstrom, and L. M. Eng. Accuracy and resolution limits of kelvin probe force microscopy. *Physical Review B*, 71(12):125424, 2005.

[81] R. Stomp, Y. Miyahara, Domenique Weiner, and Peter Grütter. Measuring absolute tip–sample capacitance with an Atomic Force Microscope. manuscript in preparation.

[82] Jacob Israelachvili. *Intermolecular & Surface Forces, second edition*. Academic Press, London, 1991.

[83] R. Garcia and A. San Paulo. Dynamics of a vibrating tip near or in intermittent contact with a surface. *Physical Review B*, 61(20):13381–13384, 2000.

[84] F. J. Giessibl. Forces and frequency shifts in atomic-resolution dynamic-force microscopy. *Physical Review B*, 56(24):16010–16015, 1997.

[85] Keith J. Laidler and John H. Meiser. *Physical Chemistry, third edition*. Houghton Mifflin Company, Boston, 1999.

[86] A. S. Foster, A. L. Shluger, and R. M. Nieminen. Quantitative modelling in scanning force microscopy on insulators. *Applied Surface Science*, 188(3-4):306–318, 2002.

[87] A. S. Foster, A. Y. Gal, J. M. Airaksinen, O. H. Pakarinen, Y. J. Lee, J. D. Gale, A. L. Shluger, and R. M. Nieminen. Towards chemical identification in atomic-resolution noncontact afm imaging with silicon tips. *Phys. Rev. B*, 68(19):195420, Nov 2003.

[88] Y. Sugimoto, P. Pou, M. Abe, P. Jelinek, R. Perez, S. Morita, and O. Custance. Chemical identification of individual surface atoms by atomic force microscopy. *Nature*, 446(7131):64–67, 2007.

[89] R. Erlandsson, L. Olsson, and P. Martensson. Inequivalent atoms and imaging mechanisms in ac-mode atomic-force microscopy of si(111)7x7. *Physical Review B*, 54(12):R8309–R8312, 1996.

[90] M. H. Lee and W. H. Jhe. General theory of amplitude-modulation atomic force microscopy. *Physical Review Letters*, 97(3):036104, 2006.

[91] T. R. Albrecht, P. Grutter, D. Horne, and D. Rugar. Frequency-modulation detection using high-q cantilevers for enhanced force microscope sensitivity. *Journal of Applied Physics*, 69(2):668–673, 1991.

[92] R. Garcia, R. Magerle, and R. Perez. Nanoscale compositional mapping with gentle forces. *Nature Materials*, 6(6):405–411, 2007.

[93] U. Durig, H. R. Steinauer, and N. Blanc. Dynamic force microscopy by means of the phase-controlled oscillator method. *Journal of Applied Physics*, 82(8):3641–3651, 1997.

[94] U. Durig. Extracting interaction forces and complementary observables in dynamic probe microscopy. *Applied Physics Letters*, 76(9):1203–1205, 2000.

[95] F. J. Giessibl. A direct method to calculate tip-sample forces from frequency shifts in frequency-modulation atomic force microscopy. *Applied Physics Letters*, 78(1):123–125, 2001.

[96] J. E. Sader and S. P. Jarvis. Accurate formulas for interaction force and energy in frequency modulation force spectroscopy. *Applied Physics Letters*, 84(10):1801–1803, 2004.

[97] J. E. Sader, T. Uchihashi, M. J. Higgins, A. Farrell, Y. Nakayama, and S. P. Jarvis. Quantitative force measurements using frequency modulation atomic force microscopy - theoretical foundations. *Nanotechnology*, 16(3):S94–S101, 2005.

[98] M A Venegas de la Cerda, A Madgavkar J Abad, D Martrou, and S Gauthier. Step-induced tip polarity reversal investigated by dynamic force microscopy on KBr(001). *Nanotechnology*, 19(4):045503 (7pp), 2008.

[99] Tino Roll, Tobias Kunstmann, Markus Fendrich, Rolf Möller, and Marika Schleberger. Temperature dependence of the energy dissipation in dynamic force microscopy. *Nanotechnology*, 19(4):045703 (5pp), 2008.

[100] J. M. R. Weaver and D. W. Abraham. High-resolution atomic force microscopy potentiometry. *J. Vacuum Science & Technology B*, 9(3):1559–1561, 1991.

[101] S. Sadewasser and M. C. Lux-Steiner. Correct height measurement in noncontact atomic force microscopy. *Phys. Rev. Lett.*, 91(26):266101, 2003.

[102] T. Ogawa and *et al.* 3,4 : 9,10-perylenetetracarboxylic dianhydride (PTCDA) by electron crystallography. *Acta Crystall. B*, 55:123–130, 1999.

[103] Heating parent holder designed by Dr. Regina Hoffmann based on the standard parent holder supplied by JEOL. Parts machined at Basel University, Switzerland.

[104] Jeffrey M. Mativetsky. *Understanding and Controlling the Growth of Metals and Molecules on an Insulating Surface*. PhD thesis, McGill University, 2006.

[105] J. M. Mativetsky, Y. Miyahara, S. Fostner, S. A. Burke, and P. Grutter. Use of an electron-beam evaporator for the creation of nanostructured pits in an insulating surface. *Applied Physics Letters*, 88(23):233121, 2006.

[106] Sarah A. Burke. Buckminsterfullerene on KBr studied by high resolution NC-AFM: Molecular nucleation and growth on an insulator. Master's thesis, McGill University, 2004.

[107] Dominik Brandlin, Robert Sum, and Vicki Connolly. *easyPLL FM Sensor Controller*. NanoSurf, Switzerland.

[108] J.V. Barth, G. Costantini, and K. Kern. Engineering atomic and molecular structures at surfaces. *Nature*, 437:671–679, 2005.

[109] R. Bennewitz. Structured surfaces of wide band gap insulators as templates for overgrowth of adsorbates. *J. Phys: Condens. Matter*, 18:R417–R435, 2006.

[110] Gregor Witte and Christof Wöll. Growth of aromatic molecules on solid substrates for applications in organic electronics. *J. Mater. Res.*, 19(7):1889–1916, 2004.

[111] M. Bammerlin, R. Lüthi, E. Meyer, A. Baratoff, J. Lü, M. Guggisberg, C. Loppacher, C. Gerber, and H.-J. Güntherodt. Dynamic SFM with true atomic resolution on alkali halide surfaces. *App. Phys. A*, 66:S293–S294, 1998.

[112] Ch. Loppacher, U. Zerweck, L.M. Eng, S. Gemming, G. Seifert, C. Olbrich, K. Morawetz, and M. Schreiber. Adsorption of PTCDA on a partially KBr covered Ag(111) substrate. *Nanotechnology*, 17:1568–1573, 2006.

[113] L. A. Girifalco. Molecular properties of C_{60} in the gas and solid phases. *J. Phys. Chem.*, 96:858–861, 1992.

[114] Y. Kim, L. Jiang, T. Iyoda, K. Hashimoto, and A. Fujishima. AFM study of surface phenomena based on C_{60} film growth. *App. Surf. Sci.*, 130–132:602–609, 1998.

[115] K. Yase, N. Ara-Kato, T. Hanada, H. Takiguchi, Y. Yoshida, G. Back, K. Abe, and N. Tanigaki. Aggregation mechanism in fullerene thin films on several substrates. *Thin Solid Films*, 331:131–140, 1998.

[116] K. Tanigaki, S. Kuroshima, and T.W. Ebbesen. Crystal growth and structure of fullerene thin films. *Thin Solid Films*, 257:154–165, 1995.

[117] R. Lüthi, H. Haefke, E. Meyer, L. Howald, H.-P. Lang, G. Gerth, and H.-J. Güntherodt. Frictional and atomic-scale study of C_{60} thin-films by scanning force microscopy. *Zeitschrift Fur Physik B-Condensed Matter*, 95(1):1–3, 1994.

[118] J. Vogt and H. Weiss. The structure of NaCl(100) and KCl(100) single crystal surfaces: a tensor low energy electron diffraction analysis. *Surface Science*, 491:155–168, 2001.

[119] J. Vogt and H. Weiss. The structure of KBr(100) and LiF(100) single crystal surfaces: a tensor low energy electron diffraction analysis. *Surface Science*, 501:203–213, 2002.

[120] J. M. Gómez-Rodríguez, A. M. Baró, L. Vázquez, R. C. Salvarezza, J. M. Vara, and A. J. Arvia. Fractal surfaces of gold and platinum electrodeposits. dimensionality determination by scanning tunneling microscopy. *J. Phys. Chem.*, 96:347–350, 1992.

[121] J.M. Williams and T.P. Beebe, Jr. Analysis of fractal surfaces using scanning probe microscopy and multiple-image variography. 2. Results on fractal and nonfractal surfaces, observation of fractal crossovers, and comparison with other fractal analysis techniques. *J. Phys. Chem.*, 97:6255–6260, 1993.

[122] S. C. B. Mannsfeld, K. Leo, and T. Fritz. Line-on-line coincidence: A new type of epitaxy found in organic-organic heterolayers. *Phys. Rev. Lett.*, 94:056104, 2005.

[123] G. Schull and R. Berndt. Orientationally ordered (7×7) superstructure of C_{60} on Au(111). *Phys. Rev. Lett.*, 99:226105, 2007.

[124] Wei Ji, Sarah Burke, Hong-Jun Gao, Peter Grutter, and Hong Guo. Electronic hybridization of molecules on insulating surface. manuscript submitted for publication.

[125] Z. Zhang and M.G. Lagally. Atomistic processes in the early stages of thin-film growth. *Science*, 276:377–383, 1997.

[126] K. Binder. Theory for the dynamics of "clusters." ii. critical diffusion in binary systems and the kinetics of phase separations. *Phys. Rev. B*, 15(9):4425–4447, 1977.

[127] W.W. Mullins and J. Viñals. Self-similarity and growth kinetics driven by surface free energy reduction. *Acta metall.*, 37(4):991–997, 1989.

[128] B. Krause, A.C. Dürr, F. Schreiber, and H. Dosch. Thermal stability and partial dewetting of crystalline organic thin films: 3,4,9,10-perylenetetracarboxylic dianhydride on Ag(111). *J. Chem. Phys.*, 119(6):3429–3435, 2003.

[129] Y. Tang, Y. Wang, G. Wang, H. Wang, L. Wang, and D. Yan. Vacuum-deposited submonolayer thin films of a three-ring bent-core compound. *J. Phys. Chem. B*, 108:12921–12926, 2004.

[130] P. Tarazona and R. Evans. Wetting transitions at models of a solid-gas interface. *Molec. Phys.*, 48(4):799–831, 1983.

[131] P.G. deGennes. Wetting: statics and dynamics. *Rev. Mod. Phys.*, 57(3):827–863, 1985.

[132] R. Temirov, S. Soubatch, A. Luican, and F. S. Tautz. Free-electron-like dispersion in an organic monolayer film on a metal substrate. *Nature*, 444(7117):350–353, 2006.

[133] M. Mobus, N. Karl, and T. Kobayashi. Structure of perylene-tetracarboxylic-dianhydride thin-films on alkali-halide crystal substrates. *J. Crystal Growth*, 116(3-4):495–504, 1992.

[134] K. Glöckler, C. Seidel, A. Soukopp, M. Sokolowski, E. Umbach, M. Böhringer, R. Berndt, and W. D. Schneider. Highly ordered structures and submolecular scanning tunnelling microscopy contrast of PTCDA and DM-PBDCI monolayers on Ag(111) and Ag(110). *Surface Science*, 405(1):1–20, 1998.

[135] D. Schlettwein and *et al.* Ultrathin films of perylenedianhydride and perylenebis(dicarboximide) dyes on (001) alkali halide surfaces. *Chem. Mater.*, 10(2):601–612, 1998.

[136] J. M. Mativetsky, S. A. Burke, S. Fostner, and P. Grutter. Nanoscale pits as templates for building a molecular device. *Small*, 3(5):818–821, 2007.

[137] S. Mannsfeld and *et al.* Combined LEED and STM study of PTCDA growth on reconstructed Au(111) and Au(100) single crystals. *Org. Electron.*, 2:121, 2001.

[138] J. C. Swarbrick and *et al.* Square, hexagonal, and row phases of PTCDA and PTCDI on Ag–Si(111)-$\sqrt{3} \times \sqrt{3}$r30°. *J. Phys. Chem.*, 109:12167, 2005.

[139] J.B. Gustafsson, H.M. Zhang, and L.S.O. Johansson. STM studies of thin PTCDA films on Ag/Si(111)-$\sqrt{3} \times \sqrt{3}$. *Phys. Rev. B*, 75:155414, 2007.

[140] D. Shi and *et al.* Role of lateral alkyl chains in modulation of molecular structures on metal surfaces. *Phys. Rev. Lett.*, 96(22):226101, 2006.

[141] S. Sadewasser, T. Glatzel, S. Schuler, S. Nishiwaki, R. Kaigawa, and M. C. Lux-Steiner. Kelvin probe force microscopy for the nano scale characterization of chalcopyrite solar cell materials and devices. *Thin Solid Films*, 431:257–261, 2003.

[142] C. Loppacher, U. Zerweck, S. Teich, E. Beyreuther, T. Otto, S. Grafstrom, and L. M. Eng. Fm demodulated kelvin probe force microscopy for surface photovoltage tracking. *Nanotechnology*, 16(3):S1–S6, 2005.

[143] H. Hoppe, T. Glatzel, M. Niggemann, A. Hinsch, M. C. Lux-Steiner, and N. S. Sariciftci. Kelvin probe force microscopy study on conjugated polymer/fullerene bulk heterojunction organic solar cells. *Nano Letters*, 5(2):269–274, 2005.

[144] V. Palermo, M. Palma, and P. Samori. Electronic characterization of organic thin films by kelvin probe force microscopy. *Advanced Materials*, 18(2):145–164, 2006.

[145] J. Cao, J. Z. Sun, J. Hong, X. G. Yang, H. Z. Chen, and M. Wang. Direct observation of microscopic photoinduced charge redistribution on TiO_2 film sensitized by chloroaluminum phthalocyanine and perylenediimide. *Applied Physics Letters*, 83(9):1896–1898, 2003.

[146] L. Nony, R. Bennewitz, O. Pfeiffer, E. Gnecco, A. Baratoff, E. Meyer, T. Eguchi, A. Gourdon, and C. Joachim. Cu-TBPP and PTCDA molecules on insulating surfaces studied by ultra-high-vacuum non-contact AFM. *Nanotechnology*, 15(2):S91–S96, 2004.

[147] F. Bocquet, L. Nony, C. Loppacher, and T. Glatzel. Analytical approach to the local contact potential difference on (001) ionic surfaces: Implications for kelvin probe force microscopy. *Physical Review B*, 78(3):035410, 2008.

[148] Private communication with L. Nony (11th international nc-AFM conference, Madrid 2008).

[149] S. Sadewasser, T. Glatzel, R. Shikler, Y. Rosenwaks, and M. C. Lux-Steiner. Resolution of Kelvin probe force microscopy in ultrahigh vacuum: compar-

ison of experiment and simulation. *Applied Surface Science*, 210(1-2):32–36, 2003.

[150] E. Strassburg, A. Boag, and Y. Rosenwaks. Reconstruction of electrostatic force microscopy images. *Review of Scientific Instruments*, 76(8):083705, 2005.

[151] U. Zerweck, C. Loppacher, T. Otto, S. Grafstrom, and L. M. Eng. Kelvin probe force microscopy of C_{60} on metal substrates: towards molecular resolution. *Nanotechnology*, 18(8):084006, 2007.

[152] J. Kroger, H. Jensen, R. Berndt, R. Rurali, and N. Lorente. Molecular orbital shift of perylenetetracarboxylic-dianhydride on gold. *Chemical Physics Letters*, 438(4-6):249–253, 2007.

[153] N. Lorente and M. Persson. Theory of single molecule vibrational spectroscopy and microscopy. *Physical Review Letters*, 85(14):2997–3000, 2000.

[154] T. Frederiksen, M. Brandbyge, N. Lorente, and A. P. Jauho. Inelastic scattering and local heating in atomic gold wires. *Physical Review Letters*, 93(25):256601, 2004.

[155] C. T. C. Chang, J. P. Sethna, A. N. Pasupathy, J. Park, D. C. Ralph, and P. L. McEuen. Phonons and conduction in molecular quantum dots: Density functional calculations of Franck-Condon emission rates for bifullerenes in external fields. *Physical Review B*, 76(4):045435, 2007.

[156] N. Sergueev, D. Roubtsov, and H. Guo. Ab initio analysis of electron-phonon coupling in molecular devices. *Physical Review Letters*, 95(14):146803, 2005.

[157] B. A. Gregg and M. C. Hanna. Comparing organic to inorganic photovoltaic cells: Theory, experiment, and simulation. *Journal of Applied Physics*, 93(6):3605–3614, 2003.

[158] O. Guillermet, M. Mossoyan-Deneux, M. Giorgi, A. Glachant, and J. C. Mossoyan. Structural study of vapour phase deposited 3,4,9,10-perylene tetracarboxylicacid diimide: Comparison between single crystal and ultra thin films grown on pt(100). *Thin Solid Films*, 514(1-2):25–32, 2006.

[159] K. Tojo and J. Mizugushi. Refinement of the crystal structure of 3,4:9,10-perylene-bis(dicarboximide), c24h10n2o4, at 263 k. *Zeitschrift f´ur Kristallographie*, 217(1):45, 2002. Data deposited at the Cambridge Crystallographic Data center (CCDC) File: LENPEZ01, No. CCDC 187633.

[160] C. Ludwig, B. Gompf, J. Petersen, R. Strohmaier, and W. Eisenmenger. STM investigations of PTCDA and PTCDI on graphite and MoS_2 - a systematic study of epitaxy and STM image-contrast. *Zeitschrift Fur Physik B-Condensed Matter*, 93(3):365–373, 1994.

[161] B. Uder, C. Ludwig, J. Petersen, B. Gompf, and W. Eisenmenger. STM characterization of organic-molecules on H-terminated Si(111). *Zeitschrift Fur Physik B-Condensed Matter*, 97(3):389–390, 1995.

[162] M. Fendrich and T. Kunstmann. Organic molecular nanowires: N,N-'-dimethylperylene-3,4,9,10-bis(dicarboximide) on KBr(001). *Applied Physics Letters*, 91(2):023101, 2007.

[163] J. Topple, S. Burke, S. Fostner, and P. Gr´utter. PTCDI on NaCl: Dynamics of dewetting. manuscript submitted for publication.

[164] T. Fukuma, K. Kobayashi, H. Yamada, and K. Matsushige. Noncontact atomic force microscopy study of copper-phthalocyanines: Submolecular-scale contrasts in topography and energy dissipation. *Journal of Applied Physics*, 95(9):4742–4746, 2004.

[165] R. Hiesgen, M. Rabisch, H. Bottcher, and D. Meissner. Stm investigation of the growth structure of cu-phthalocyanine films with submolecular resolution. *Solar Energy Materials and Solar Cells*, 61(1):73–85, 2000.

[166] F. Van zeggeren and G. C. Benson. Calculation of the surface energies of alkali halide crystals. *Journal of Chemical Physics*, 26(5):1077–1082, 1957.

[167] J. E. Northrup, M. L. Tiago, and S. G. Louie. Surface energetics and growth of pentacene. *Physical Review B*, 66(12):121404(R), 2002.

[168] D. Nabok, P. Puschnig, and C. Ambrosch-Draxl. Cohesive and surface energies of pi-conjugated organic molecular crystals: A first-principles study. *Physical Review B*, 77(24):245316, 2008.

[169] W. R. Tyson and W. A. Miller. Surface free-energies of solid metals - estimation from liquid surface-tension measurements. *Surface Science*, 62(1):267–276, 1977.

[170] J. L. F. Da Silva, C. Stampfl, and M. Scheffler. Converged properties of clean metal surfaces by all-electron first-principles calculations. *Surface Science*, 600(3):703–715, 2006.

[171] Sung Chul Jung and Myung Ho Kang. First-principles study of a single C_{60} cluster adsorbed on KBr(100). *Surface Science*, 602:1916–1920, 2008.

[172] J. Frenkel and T. Kontorova. Plastic deformation of crystals. *Journal of Physics USSR*, 1:137–149, 1939.

[173] S. W. Koch, W. E. Rudge, and F. F. Abraham. The commensurate incommensurate transition of krypton on graphite - a study via computer-simulation. *Surface Science*, 145(2-3):329–344, 1984.

[174] Y. Chen, R. T. Williams, and W. A. Sibley. Defect cluster centers in MgO. *Physical Review*, 182(3):960, 1969.

[175] C. Barth and C. R. Henry. Atomic resolution imaging of the (001) surface of UHV cleaved MgO by dynamic scanning force microscopy. *Physical Review Letters*, 91(19):196102, 2003.

[176] C. Tusche, H. L. Meyerheim, N. Jedrecy, G. Renaud, A. Ernst, J. Henk, P. Bruno, and J. Kirschner. Oxygen-induced symmetrization and structural coherency in Fe/MgO/Fe(001) magnetic tunnel junctions. *Physical Review Letters*, 95(17):176101, 2005.

[177] S. Altieri, L. H. Tjeng, and G. A. Sawatzky. Electronic structure and chemical reactivity of oxide-metal interfaces: MgO(100)/Ag(100). *Physical Review B*, 61(24):16948–16955, 2000.

[178] S. R. Forrest and Y. Zhang. Ultrahigh-vacuum quasiepitaxial growth of model van der waals thin films. I. Theory. *Physical Review B*, 49(16):11 297–11 308, 1994.

[179] J. P. Perdew, J. A. Chevary, S. H. Vosko, K. A. Jackson, M. R. Pederson, D. J. Singh, and C. Fiolhais. Atoms, molecules, solids, and surfaces - applications of the generalized gradient approximation for exchange and correlation. *Physical Review B*, 46(11):6671–6687, 1992.

[180] P. E. Blochl. Projector augmented-wave method. *Physical Review B*, 50(24):17953–17979, 1994.

[181] G. Kresse and D. Joubert. From ultrasoft pseudopotentials to the projector augmented-wave method. *Physical Review B*, 59(3):1758–1775, 1999.

[182] G. Kresse and J. Hafner. Abinitio molecular-dynamics for liquid-metals. *Physical Review B*, 47(1):558–561, 1993.

[183] G. Kresse and J. Furthmuller. Efficient iterative schemes for ab initio total-energy calculations using a plane-wave basis set. *Physical Review B*, 54(16):11169–11186, 1996.

[184] W. Ji, Z. Y. Lu, and H. Gao. Electron core-hole interaction and its induced ionic structural relaxation in molecular systems under x-ray irradiation. *Physical Review Letters*, 97(24):246101, 2006.